FINITE ELEMENT SIMULATIONS OF IMPACT TEST FOR LIGHT ALLOY WHEELS

A Thesis Submitted to
the Graduate School of Engineering and Sciences of
İzmir Institute of Technology
in Partial Fulfillment of the Requirements for the Degree of

DOCTOR OF PHYLOSOPHY

in Mechanical Engineering

by
Uğur PEHLİVANOĞLU

November 2016
İZMİR

We approve the thesis of **Uğur PEHLİVANOĞLU**

Examining Committee Members:

Prof. Dr. Bülent YARDIMOĞLU
Department of Mechanical Engineering, İzmir Institute of Technology

Assoc. Prof. Dr. H. Seçil ARTEM
Department of Mechanical Engineering, İzmir Institute of Technology

Prof. Dr. Ramazan KARAKUZU
Department of Mechanical Engineering, Dokuz Eylül University

Assist. Prof. Dr. Gökhan KİPER
Department of Mechanical Engineering, İzmir Institute of Technology

Assist. Prof. Dr. Levent AYDIN
Department of Mechanical Engineering, İzmir Katip Çelebi University

02 November 2016

Prof. Dr. Bülent YARDIMOĞLU
Supervisor, Department of Mechanical Engineering,
İzmir Institute of Technology

Prof. Dr. Figen KOREL
Deputy Head of the Department of
Mechanical Engineering

Prof. Dr. Bilge KARAÇALI
Dean of the Graduate School
of Engineering and Sciences

ACKNOWLEDGEMENTS

First and foremost, I would like to express gratitude to my advisor, Prof. Dr. Bülent YARDIMOĞLU, for his support through every step of my PhD, a significant effort of more than 5 years. Without his great theoretical and academic knowledge, it would have been impossible to improve my research background. His instructions in Advanced Mechanics of Materials, Analytical Methods in Vibrations, Finite Element Analysis in Solid Mechanics and Theory of Plasticity combined with my practical software knowledge generated a new perspective toward solving mechanical engineering problems. He convinced me to study as a full time researcher to finalize the PhD, while this period enabled me to experience academic environment and enlarge my point of view.

Furthermore, I want to praise the advice of my thesis supervising committee members Prof. Dr. Ramazan KARAKUZU and Assoc. Prof. Dr. H. Seçil ARTEM, while Dr. Cihangir ÖZCANLI is appreciated for his lectures.

I would also like to acknowledge financial support by The Scientific and Technological Research Council of Turkey, (Project Number: 3120356), which supported experimental sections and some of the computer simulations performed in this thesis.

Finally, my family deserves great thanks for their emotional and mental support; especially my wife who allowed me to spend my time for concluding the studies.

Last but not least, I would like to thank my mother and father for their encouragements to complete my PhD study.

ABSTRACT

FINITE ELEMENT SIMULATIONS OF IMPACT TEST FOR LIGHT ALLOY WHEELS

Static and dynamic finite element models for the simulation of the wheel impact test defined in ISO7141 were developed for the AlSi7Mg and AlSi11Mg alloy wheels. The dynamic model consists of the striker, the wheel with radial pneumatic tire, and the hub adapter structure. Two types of tire models, composite and simplified, are formed in this study. The finite element model in the dynamic model, referred to as composite tire, involves bead, bead core, casing and crown plies, tread, and side walls. A simplified tire model that does not include bead cores, casing and crown plies is also generated. Although these items are not used in the second model directly, they are considered using their equivalent effects. It is shown that a simplified tire model can be used instead of the composite tire model.

The dynamic model is validated by experimental studies. Such studies are related to the plastic deformations at the impact point of the wheel. It is shown that simulation of the failure of the wheel during impact tests can be determined using von Mises and effective plastic strain occurs in the wheel.

In total, forty-one experiments are done to see the wheel behaviors and whether it performes according to the standard. The experimental results and the corresponding simulations focusing on von Mises stresses along with effective strains are shown in box plots. Thus, critical values for design are found.

The static model consists of the wheel with simplified tire and the lumped model of the hub adapter structure. The stiffness characteristic of the impact point of the wheel is determined by using the static model. It is shown that the maximum von Mises stress that occurs in the wheel due to impact load is found using energy conversions. Significant time can be saved by this manner.

ÖZET

HAFİF ALAŞIMLI JANTLAR İÇİN DARBE TESTİNİN SONLU ELEMAN BENZETİMLERİ

Bu tezde, AlSi11Mg ve AlSi7Mg alaşımlı jantlar için ISO 7141 de tanımlanan darbe testi benzetiminin statik ve dinamik sonlu elemanlar modeli elde edilmiştir. Dinamik sonlu elemanlar modeli; vurucu, radyal lastikli jant ve darbe tezgâhından oluşmuştur. Tezde, kompozit ve basitleştirilmiş lastik olarak iki tip lastik oluşturulmuştur. Kompozit lastik olarak isimlendirilen dinamik modeldeki lastiğin sonlu elemanlar modeli topuk, topuk çemberi, sentetik ve çelik kuşak, sırt ve yan duvarlardan oluşur. Ayrıca, topuk çemberi, sentetik ve çelik kuşağı kullanmayan basitleştirilmiş lastik modeli oluşturulmuştur. Ancak, ikinci modelde doğrudan kullanılmadığı belirtilen unsurların eşdeğer etkileri göz önüne alınmıştır. Basitleştirilmiş lastik modelinin kompozit lastik yerine kullanılabilirliği gösterilmiştir.

Dinamik model deneysel çalışmalarla doğrulanmıştır. Deneysel çalışmalar jantın darbe noktasında meydana gelen kalıcı şekil değişimleri ile ilgilidir. Jantın darbe testinden geçişinin benzetiminde, jantta meydana gelen von Mises ve efektif plastik birim şekil değiştirmelerin kullanılabileceği gösterilmiştir.

Bunlardan başka, standarda göre jantların testi geçip geçemeyeceğini görmek için toplam kırk bir deney yapılmıştır. Elde edilen deneysel sonuçlar ve bu sonuçların her birine karşılık yapılan maksimum von Mises gerilimleri ve birim şekil yer değiştirmelere odaklanmış benzetimlerin değerleri kutu grafikleri ile gösterilmiştir. Böylece tasarım için kritik değerler bulunmuştur.

Statik sonlu elemanlar modeli, basitleştirilmiş lastik modeli, jant ve topaklanmış test tezgâhından ibarettir. Jantın darbe noktasının yay karakteristiği statik modelle elde edilmiştir. Darbe yükünden dolayı jantta meydana gelen von Mises gerilimlerinin enerji dönüşümü ile bulunacağı gösterilmiştir. Böylece önemli bir zaman tasarrufu sağlanabilir.

TABLE OF CONTENTS

APPENDICES

LIST OF FIGURES

LIST OF TABLES

LIST OF SYMBOLS

A_f	Cross-sectional area of fiber
A_r	Cross-sectional area of rubber
A_{rf}	Cross-sectional area of object having rubber and fiber
A_0	Cross-sectional area of specimen under the axial load
B_i	Boundary function
c	Viscous damping coefficient
c_{eq}	Equivalent viscous damping
$C[\ ]$	Differential operators for damping
$[C]$	Damping matrix
C_{ij}	Components of the right Cauchy-Green deformation tensor
C_{10}, C_{01}	Mooney-Rivlin parameters
$\{d\}$	Element displacement vector
$\{D\}$	Displacement vector of entire body
D_1	Mooney-Rivlin parameter
e	Coefficient of restitution
E	Modulus of elasticity of isotropic material
E_{ij}	Components of the Lagrangian strain tensor
ΔE	Energy loss per cycle
E_r	Modulus of elasticity of rubber
E_{rf}	Equivalent modulus of elasticity of composite material with rubber and fibres
E_f	Modulus of elasticity of fibre
$\vec{F}$	Force vector,
F	Scalar value of force $\vec{F}$
F^a	Applied load
F^{nr}	Restoring force at iteration i
$F(x,y,t)$	External loading function
F_{ij}	Deformation gradients
F_x, F_y, F_z	Force components in x, y, z directions, respectively
$\{F(t)\}$	Force vector

g	Gravity
h	Hysteretic damping constant, height
H^n	Hourglass resistance
I_1, I_2, I_3	Invariants of C_{ij}
$\vec{I}_{1\to 2}$	Impulse
k	Stiffness
k^*	Complex stiffness factor of material
K	Initial bulk modulus.
$[K]$	Stiffness matrix
$[K_i^T]$	Tangent stiffness matrix at iteration i
l	Original length of the specimen under the axial load
l_0	Initial length of the specimen under the axial load
L	Length
$L[\ ]$	Differential operators for stiffness
m	Mass of particle, mass of the striker
M	Mass of collar
$M[\ ]$	Differential operators for mass, and
$[M]$	Mass matrixes
$[N(x,y)]$	Shape function matrix
$N_r(t)$	Modal force
P	Forces acting on particle during deformation or axial force.
P^n	External and body forces.
$\{q(t)\}$	Displacement vector
R	Forces acting on particle after deformation
S^n	Stress divergence vector
S_{ij}	Components of the second Piola-Kirchhoff stress tensor
Q_1, Q_2,Q_3	Values in box plot
t	Time
Δt	Time step
u	Particles velocity during and after deformation
u_i	Displacement at iteration i
$\vec{v}$	Velocity vector
v	Scalar value of velocity $\vec{v}$ before impact

v'	Scalar value of velocity $\vec{v}$ after impact
$w(x,y,t)$	Displacement function
W	Weight, maximum static wheel load, strain energy density function
$W_r(x,y)$	Characteristic function
$\{x(t)\}$	State space vector
x, y	x, y coordinate of a particle/discrete element
X	Magnitude of the steady-state response
α, β	Proportional damping coefficients
γ	Loss factor of material
δ,	Elongation
δ_{ij}	Kronecker delta
$\delta_{\max}$	Maximum elongation
δ_{st}	Elongation under static load
ε	Strain
ε^e	Elastic strain
ε^p	Plastic strain
$\acute{\varepsilon}$	Strain rate
$\eta_r(t)$	Time dependent generalized coordinates
$\lambda_1, \lambda_2, \lambda_3$	Principal stretch ratios
μ	Friction Coefficient, initial shear modulus.
ξ	Damping ratio
ξ_r	r^{th} modal damping ratio
σ	Stress
$\sigma_{\max}$	Maximum stress
σ_{ij}	Cauchy stress
σ_n	Nominal stress
σ_{st}	Stress under static load
τ_{ij}	Kirchhoff stress
ω	Forcing frequency
ω_d	Damped natural frequency
ω_n	Natural frequency
ω_r	r^{th} modal natural frequency

CHAPTER 1

INTRODUCTION

An automobile wheel is a very crucial component in automobiles due to the functionality. Moreover, when safety is considered, the wheel is also one of the most important parts of a vehicle. Due to these reasons, the design validation process of wheels has strict qualifications. The wheel design has to not only meet these qualifications, but also be aesthetic and economic. There are several destructive mechanic tests performed to validate wheel design after sample production. These are (i) rotating bending tests, (ii) radial fatigue test and (iii) impact test. All these destructive mechanic tests are performed after the mold and sample production based on the initial or modified design. If the wheel does not pass the tests, the design validation process restarts to modify the wheel geometry, which requires the mold modifications. The simulations of these tests have an important role to avoid restarting the design verification process and decrease time and cost. Although simulations of rotating bending tests and radial fatigue tests have been performed widely by wheel designers for the last decades, impact test simulations force wheel producers to effectively complete the design requirements. It should be emphasized that impact test simulation models are very complex and related with the nonlinear dynamic problem as material and large deformation.

The wheel is one of the oldest and most important inventions for humans. Although it is simple form of a circular disc rotating about an axle, humans obtained mechanical mobility which had a great effect on history. It is not known exactly how or where the wheel was invented, but research indicates that the first use of wheels was about 3000 BC. The first cart wheels were developed by the inhabitants of the Middle East. The first spoke wheels appeared around 2000 BC in Egypt found in the catacombs of the Pharaohs illustrated in Figure 1.1.

At the time of the Iron Age, around 1200 BC, an important advance was achieved. The rims of wooden wheel were covered with iron hoops by skilled Hittite blacksmiths. This type of wheel was widespread throughout the Assyrian Empire and people of other races.

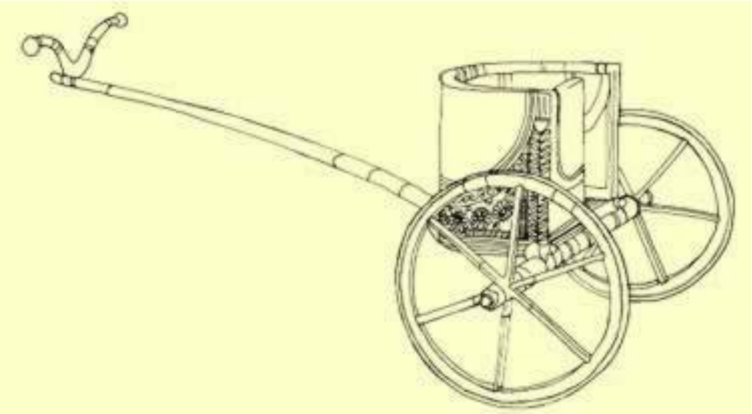

Figure 1.1 A typical Egyptian chariot with six-spoke wheels.
(Source: http://www.touregypt.net/featurestories/chariots.htm)

During the middle ages, spoke and solid wooden wheels were used widely on rough country roads. As the towns flourish, the wheels with their iron hoops caused severe damage to the stone-paved streets and they were banned out of cities. The use of wheels of different sizes on the rear and front axles also improved the mobility of carts and wagons during this period.

Until Scottish inventor, Robert William Thomson invented the first pneumatic tire shown in Figure 1.2 in 1845, wheels with wooden, steel and wire spokes were used without any type of shock absorption. Though this was a great invention, Thomson's tire was never commercially successful due to the cost of rubber at that time. Forty years later, in 1888, John Boyd Dunlop developed a practical pneumatic tire. The motor car had been invented a few years earlier by Carl Benz (Kermelk 1999).

Figure 1.2. First pneumatic tire invented by Robert William Thomson
(Source: http://blog.hemmings.com/index.php/2013/12/10/this-day-in-history-1845-robert-william-thomson-patents-the-pneumatic-tire/)

A number of developments have been obtained for different purposes and applied to a wide range of applications over the years. One of the most important one was a tire with a flexible bead that allowed it to be directly fitted over the rim flange.

The weight of the wheels has always been a consideration. So, a variety of lightweight center sections were specially designed or arranged in order to enable vertical as well as axial and tangential forces to be transmitted from the tire to the axle. The development of rims led to the use of steel profiles with variations in thickness to be obtained during rim production to have homogenous stress distribution and a lighter wheel.

Meanwhile, entirely different production methods for casting and forging have been gradually adapted with alternative materials such as aluminum and magnesium or combinations of them. The most diverse types of materials and technological options are now available, enabling the optimum level of functional efficiency, weight and cost.

The function of the wheel shown in Figure 1.3 provides connection from the axle to the tire and to transmit forces from one to the other.

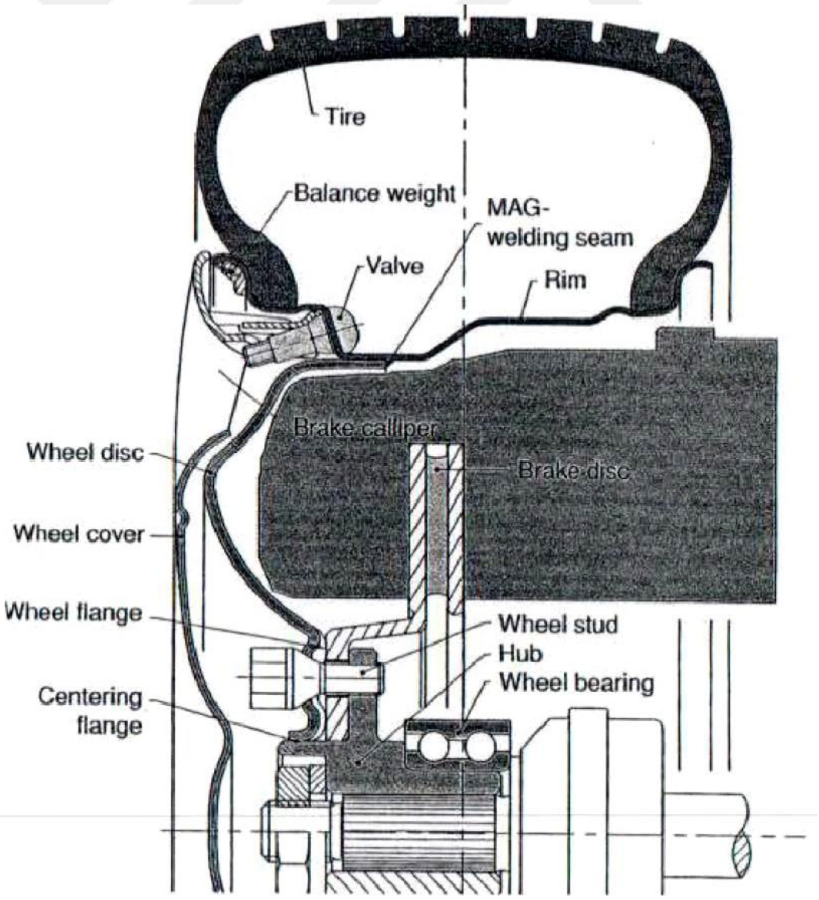

Figure 1.3. Typical car wheel mounting arrangement
(Source: Kermelk, 1999)

The rim and either the disc or wheel bodies are the principal components of the wheels. The wheel can be one piece or multiple parts as a disc-type or spoke wheel, depending on the type of material and technology used. It is properly shaped to house the tire (to form an airtight seal) and to permit mounting to the hub. At the same time, wheels are progressively becoming a styling feature for vehicles and are also required to provide efficient ventilation for the brakes.

The wheel is one of several crucial safety parts of an automotive, including the wheel stud and steering system. If the functions of these systems malfunction, the car is totally lost. Due to this reason, the design and design verification phase of the wheel is crucial. The design of the wheel must match all the requirements defined by international standards, regulations and direct instructions of the vehicle manufacturer.

Wheel types change according to production methods, material and the intended purpose. Steel disc wheels, cast light alloy and forged wheels are the main types according to material and production methods. The wheel’s rim profile and disc shape may vary depending on type of vehicle such as passenger cars, commercial vehicles, agricultural tractors, cycles and motorcycles.

Steel disc wheels consist of two parts - the disc and the rim. They are made from bot-rolled sheet steel manufactured by rolling and deep drawing processes. The disc and the rim are spot or arc welded together. This type of wheel has the optimum design in terms of economy, serviceability and safety.

Cast light alloy and forged wheels are categorized by low weight and very good uniformity. These types of wheels can have stylish designs. Aluminum or, more rarely, magnesium is usually cast in one piece by the low-pressure or gravity die casting method. A sample of light alloy wheel is shown in Figure 1.4.

Figure 1.4. A sample of light alloy wheel

Forged wheels are shaped in a number of forging and flow forming processes. In both cases, finishing takes place with the turning of functional faces or contours, such as the rim profile, wheel flange and center hole, and the drilling or milling of stud boles and valve. Depending on the degree of strength required, these operations may be preceded by heat treatment.

Wheel impact test is standardized with ISO7141 and SAE J175 standards. However, these standards refer to the vehicle manufacturer requirements in some steps. Therefore, impact test machines must be produced according to these standards. Also, the calibration procedure of the impact test machine is defined in the standards.

It is possible to find a few studies on impact test simulations generally based on the finite element method. On the other hand, since the tire is a critical part of the impact test, a suitable finite element model of the tire is necessary to obtain more accurate results. Unlike the wheel impact test, there are many different studies on the finite element modeling of tires. Selected studies about finite element modeling of the impact test and the tire are summarized chronologically below.

Riesner et al (1986) applied finite element analysis and used total plastic work approach to predict the result of SAE J175 wheel impact test. Their study is based on three separate analyses; static, dynamic and fracture mechanics. The spring constant for the impact point of the wheel is obtained from the static finite element model of the 72^0 portion of the wheel instead of the entire wheel. They modeled the impact test as a dynamic model which consists of lumped masses, springs, and dampers to simulate the dynamic response. The maximum displacement of the impact point of the wheel is obtained from dynamic analysis. The peak force occurred during impact was calculated by multiplying spring constant and the maximum displacement of the impact point of the wheel. The peak force was applied to the static model of the wheel to calculate the stress and strain energy density distribution, and total plastic work approach was used to predict the wheel failure.

The impact test system used for their study shown in Figure 1.5 is different from the the system used today. Their test system had a main weight of 2000 lb with an auxiliary weight of 220 lb, and combined three springs. The spring system was preloaded before impact and the distance between the two weights was 2.5 in before contact. However, the present impact test system modeled in this study does not have such a spring assembly and an auxiliary weight due to the current standard. Moreover, the wheel is mounted to a different fixture known as wheel hub adapter structure.

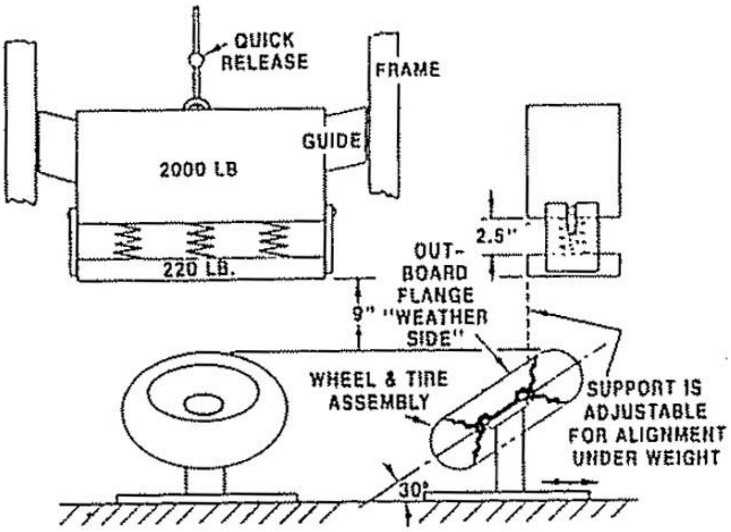

Figure 1.5. Wheel impact test system of Riesner
(Source: Riesner et al., 1986)

Lee et al (2000) studied the effect of strain rate on the stress–strain curve for aluminum alloys. Their studies indicated that if the strain rate is low ($\dot{\varepsilon}<10^{2}–10^{3}\ s^{-1}$), the effect of strain rate on the mechanical properties is insignificant.

Orengo et al (2003) investigated several tire finite element models for simulation of vehicle impact to roadside hardware and showed that a tire model composed of isotropic shells with uniform thickness for rubber leads to very unrealistic deformations. They used anisotropic modeling technique and developed a radial tire model consisting of bead coils, radial fibers, rubber sidewall, steel belt and tread by using LS-DYNA. They modeled the bead coils using two rings of shell elements with elastic properties and a relatively high Young's modulus. Radial fibers were considered as beam elements with properties of the equivalent to a distributed layer of radial fibers. The model is shown in Figure 1.6.

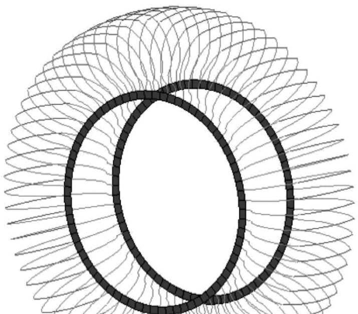

Figure 1.6. FEM of the radial reinforcement fibers and of the bead coils
(Source: Orengo et al., 2003)

Hall et al (2004) developed a tire model using shell and solid elements for a P195/65 R15 tire to simulate the behavior of the tire under different vertical loading and contact patch geometry. They used hyper-elastic rubber material model for the main body of the tire, an orthotropic elastic material for the plies/bands and mild steel for bead. They found a good correlation between the load-deflection characteristics of the tire.

Shang et al. (2005) developed a numerical model of the impact test for an A356 aluminum alloy wheel by using LS-DYNA. Their model consists of a wheel, tire and striker as shown Figure 1.7. They considered material inhomogeneities using tensile test results obtained from a different part of the wheel: hub, spoke, and rim. Also, they used a nonlinear elasto-plastic material model for the whole wheel.

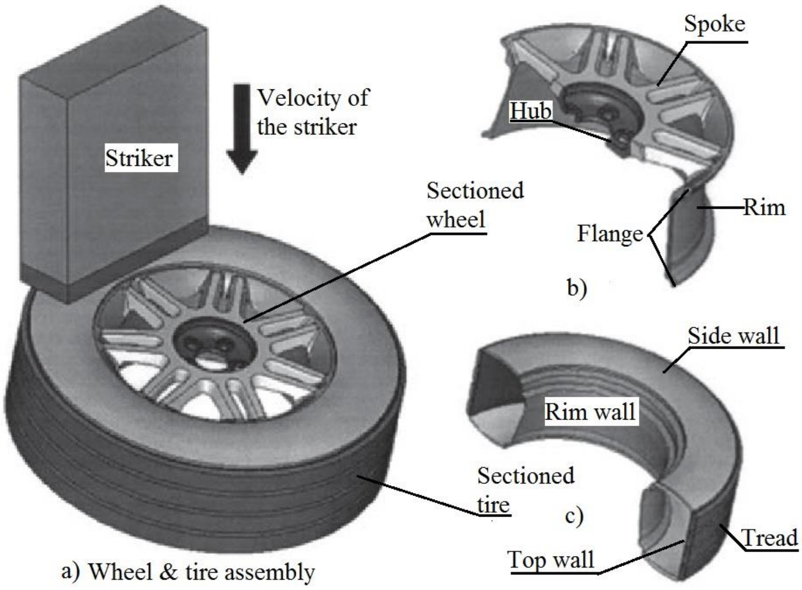

Figure 1.7 Model of the wheel impact test
(Source: Shang et al., 2005)

They modeled the tire P215/60R16 by shell and solid elements. However, they used homogenous properties for the tire regions such as side wall, top wall, and tread. They used “Airbag simple pressure volume” keyword command in LS-DYNA for the air pressure within the tire. They asserted that the tire is capable of transmitting impact loads but modeling a tire is complex and needs additional computing time. Therefore, to remove the tire from the finite element model, while considering the von-Mises stresses and plastic strain, they found that the energy absorption ratio of the tire is 20 %. They verified their numerical model by comparing the length of “A” shown in Figure 1.8 with experimental results.

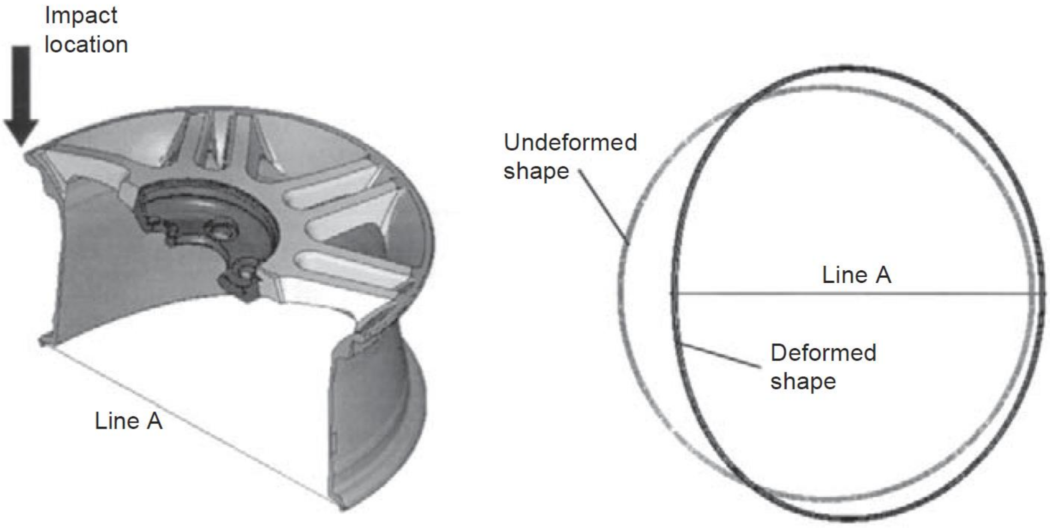

Figure 1.8 Definition of Line A
(Source: Shang et al., 2005)

Reida et al (2007) developed a detailed tire model for a LT245/75R16 tire considering the main parts shown in Figure 1.9. Their model can be summarized as follows:

1. Tread: solid elements, hyper-elastic rubber material model
2. Sidewall: shell elements, elastic material model
3. Steel beads, steel belts, and body plies: beam elements, elastic material model

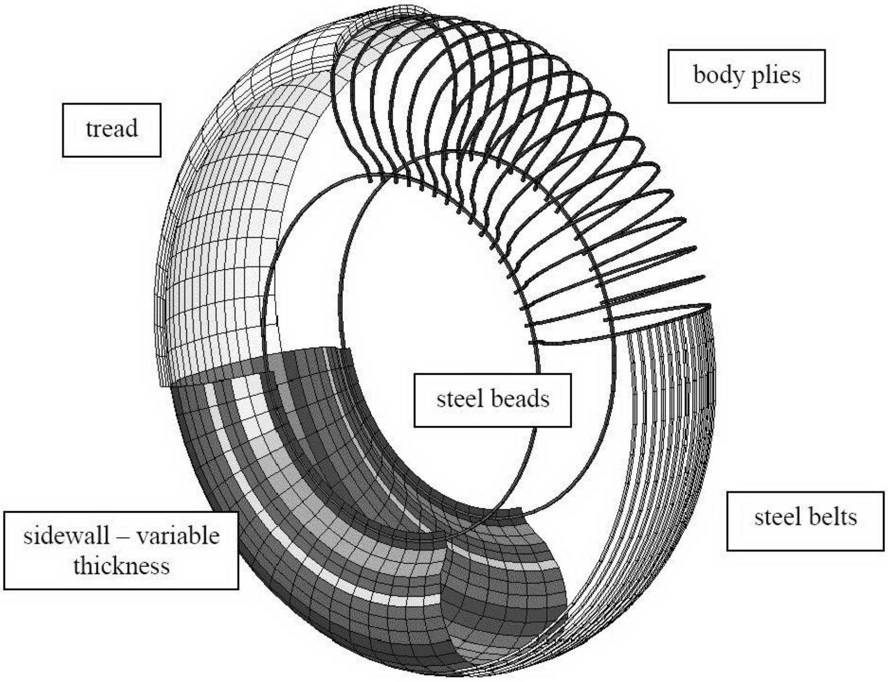

Figure 1.9. The complete model of the tire
(Source: Reida et al., 2007)

Chang and Yang (2009) performed nonlinear dynamic finite element analysis to simulate the behavior of a forged aluminum wheel 6061-T6 for impact test. The analysis model is shown in Figure 1.10 with the components.

They used the strain energy density as a damage parameter to predict the wheel failure. The fracture criterion was based on the total plastic work obtained from the tensile test with test specimens cut from the wheel. They also showed that the effect of strain rate on the mechanical properties of the wheel can be neglected. The material properties and material models are available in their publications. ABAQUS/Explicit commercial finite element software was used to carry out the nonlinear dynamic analysis of the wheel impact test. The finite element types used in the model are given as follows:

- Striker : Hexahedron element
- Wheel : Hexahedron and tetrahedron elements
- Tire : Shell element
- Cushion : Hexahedron element
- Support : Hexahedron element

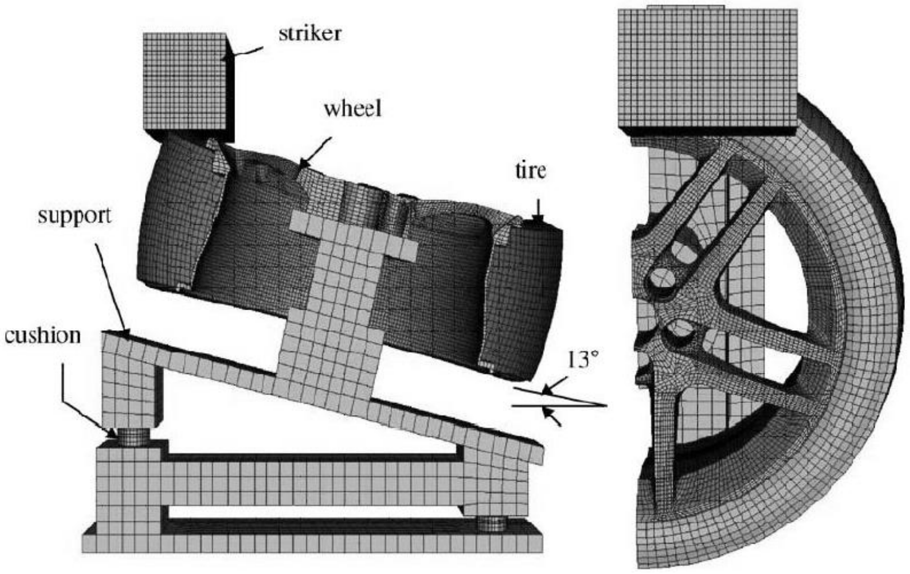

Figure 1.10. Finite element model for wheel impact test
(Source: Chang and Yang, 2009)

They also showed that optimum mesh size for the wheel is 5 mm. Mesh convergence study is carried out according to the displacement at the contact point between the striker and the wheel. Mesh convergence plot at contact points is shown in Figure 1.11.

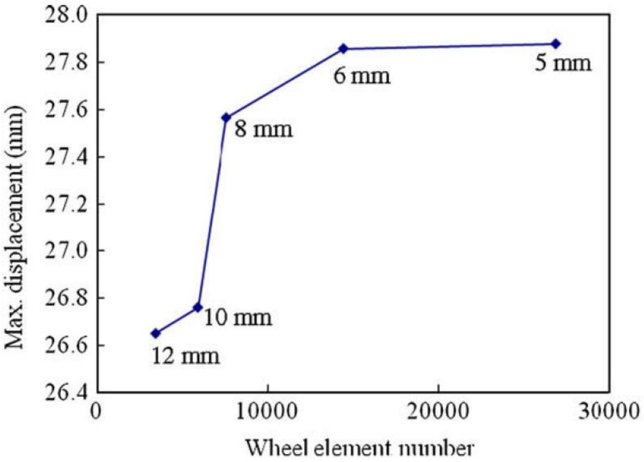

Figure 1.11. Mesh convergence study at contact points
(Source: Chang and Yang, 2009)

They modeled the air pressure of tire as static pressure. The model involved clamping load induced by the tightening torque on the bolt. The clamping force was simulated by applying both a concentrated force on the support plate and a surface load on the conical surface of bolt hole as shown in Figure 1.12

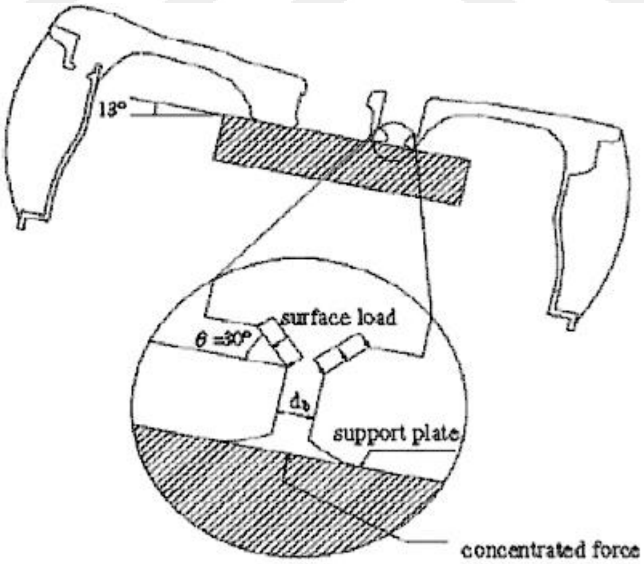

Figure 1.12. Clamping force region
(Source: Chang and Yang, 2009)

Cheng et al (2011) developed the 3D finite element model of a 195/60R14 radial tire shown in Figure 1.13 and studied the load performance of the radial tire numerically by using finite element software MARC. They used the rebar model shown in Figure 1.16 for rubber matrix which is composed of two belt layers in rubber. The individual cords and rubbers were assumed as isotropic. Eight-node brick elements were used for the 3D finite element model. The material models of the rubber matrix and the cords were Mooney–Rivlin and linear elastic, respectively.

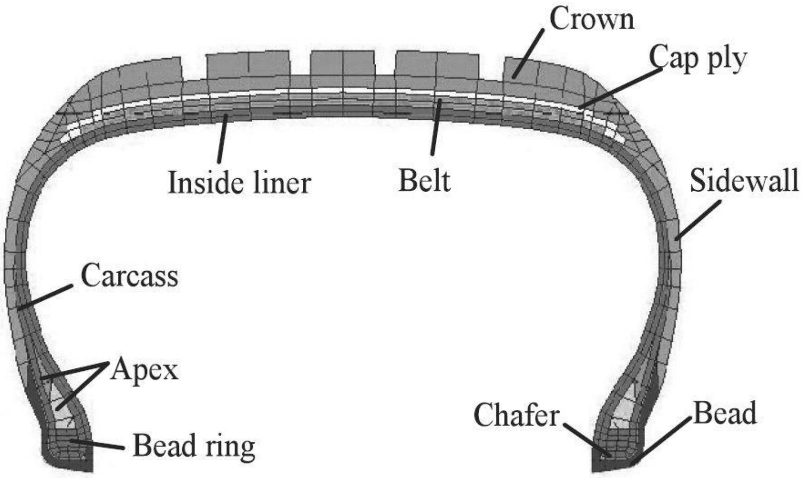

Figure 1.13. The Finite element model of the tire.
(Source: Cheng et al., 2011)

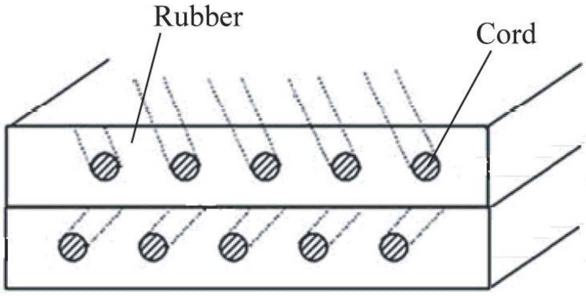

Figure 1.14. Rebar model
(Source: Cheng et al., 2011)

Jigang and Guozh (2012) performed the finite element model of impact test of wheel, shown in Figure 1.15 by using ANSYS/LS-DYNA. In their study, the maximum equivalent stress obtained from simulation was used as a damage parameter to predict the wheel failure. They considered the material of the wheel as a brittle material and measured the yield stress as impact strength of the wheel. They performed two numeric analyses and experimental impact tests using two different wheel models. The impact load was 540 kg and the tire was P225/60R16. The maximum equivalent stress occurred on the wheels was 241 MPa and 210 MPa for the first and second model of the wheel, respectively. The second wheel passed but the first one failed in the test. The first wheel broke down where the maximum stress occurred in the numerical analyze.

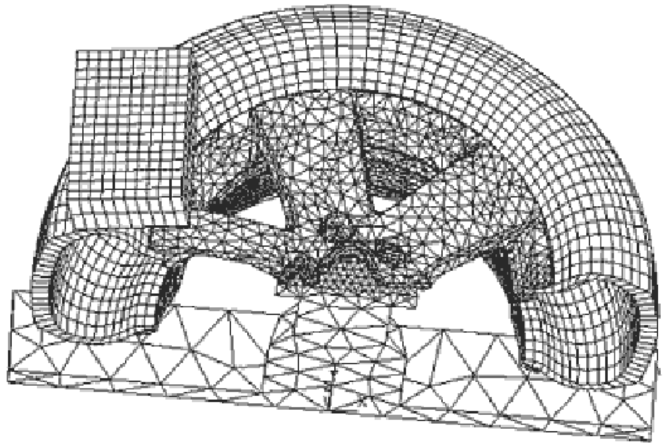

Figure 1.15. The finite element mesh model of the impact test
(Source: Jigang and Guozh, 2012)

Yuan et al. (2012) obtained the finite element model of whole system shown in Figures 1.16. The first principal strain from simulation was used as a damage parameter to predict the wheel failure. The Mooney-Rivlin model, which has two parameters, was used to describe hyper elastic behavior of rubber under large deflection. Air pressure of tire was modeled as static pressure. The material of wheel was A356 (AlSi7Mg) and its uniaxial tensile test data was provided in their study. According to the experimental data, nonlinear plastic materials were used to simulate the wheel.

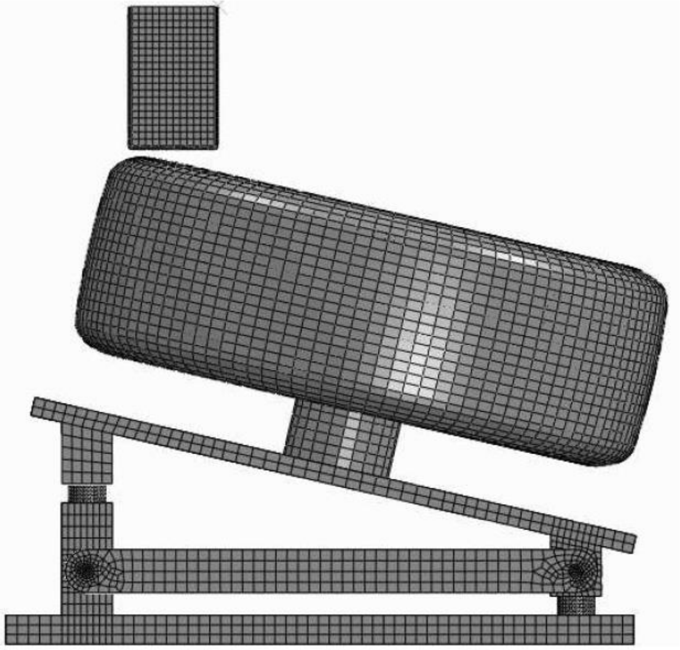

Figure 1.16 The finite element model of whole system for impact test
(Source: Yuan et al., 2012)

Tsai and Huang (2013) studied the wheel impact test without modeling the tire, but they considered the pre-stress that occurred in outer rim flanges due to the tire pressure by applying tire the force T_f, shown in Figure 1.17, to the wheel model. In the figure, P_0 is tire pressure, a is the distance from the center of the wheel to the inside wall of the wheel, r_f is the radius of the wheel rim. Bilinear isotropic hardening material model was used for the wheel. The equivalent plastic strain was selected as failure criteria.

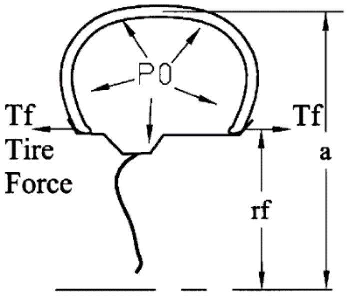

Figure 1.17. Side pressure distribution of the wheel rim.
(Source: Tsai and Huang, 2013)

Ishikawa et al (2014) conducted the finite element and experimental analysis of the 13° and 90° impact tests of the aluminum wheel by using the ABAQUS. The models involved both wheels and tires. The hub adapter structure of 13° for the impact test was also considered in the model. The structure of the tire model is shown in Figure 1.18.

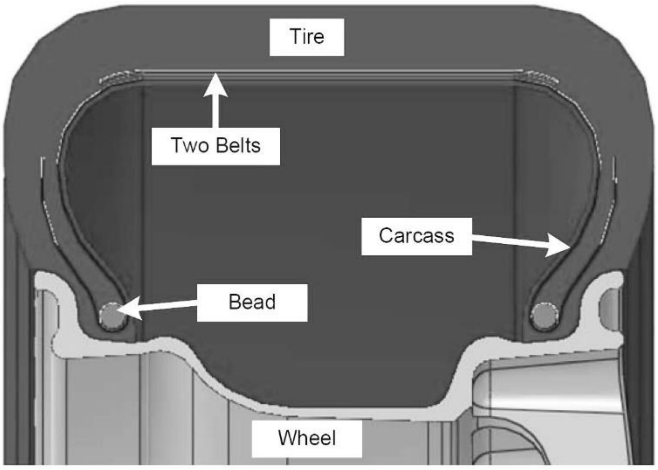

Figure 1.18. The structure of tire model.
(Source: Ishikawa et al., 2014)

They used static pressure for air inside of the tire. Neo-hookean hyperelastic material model was used for the tire; rebar model is used for the belts and carcass. The bead was modeled by three dimensional solid elements. Ten nodes modified tetrahedron solid elements were used for the model of the wheel. The entire model of the 13° impact test is shown in Figure 1.19. The hub adapter structure was supported by dashed connector elements which figured the rubber inelastic behavior. The 90° impact test is illustrated in Figure 1.20.

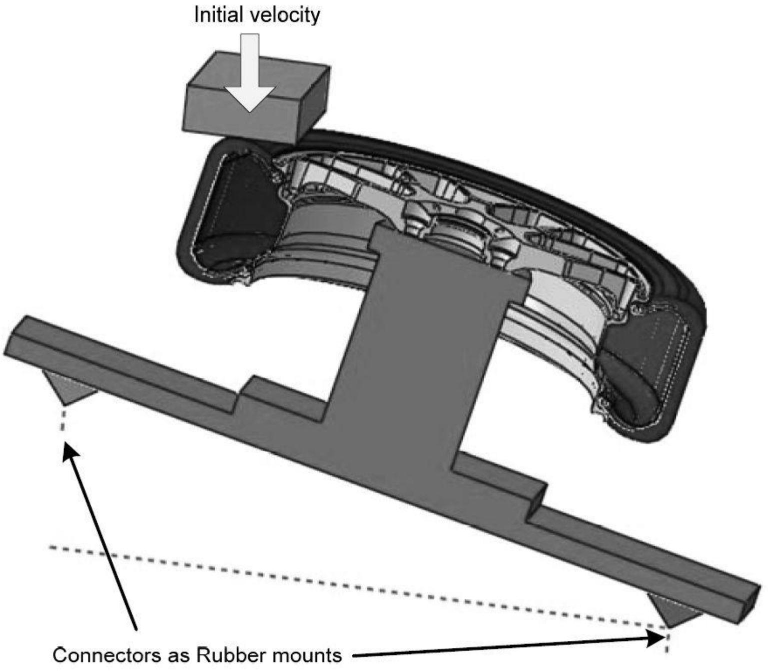

Figure 1.19. The entire model of the 13° impact test
(Source: Ishikawa et al., 2014)

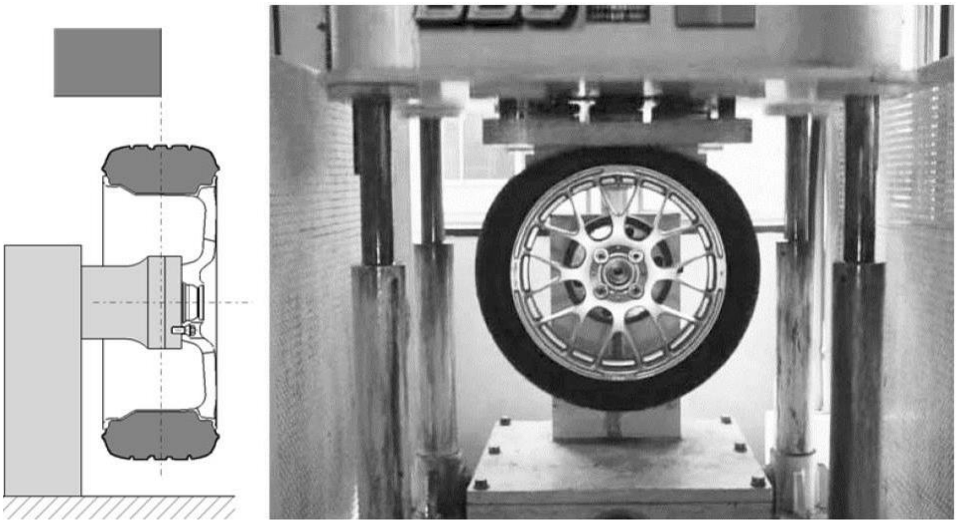

Figure 1.20. The 90° impact test
(Source: Ishikawa et al., 2014)

Moreover, they performed two different types of numerical analyses of the 13 impact tests. First type was with the tire model, and second was without. The deformed section outlines of the wheel that were obtained numerically and experimentally are shown in Figure 1.21. The outlines obtained from the model with tire and experiments are very similar. However, the outline of the wheel obtained from the model without the tire is significantly different from the experimental result. Therefore, the finite element model of the 13° impact test has to involve a tire model.

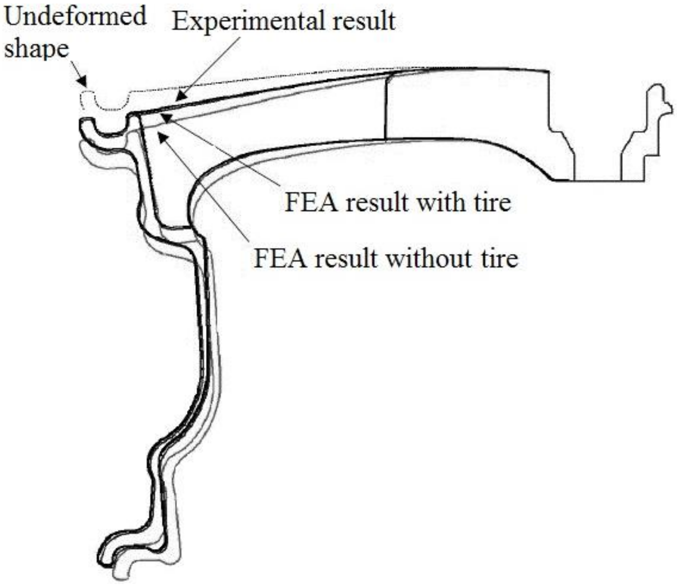

Figure 1.21. Comparison of deformed outlines of the wheel.
(Source: Ishikawa et al., 2014)

In Table 1.1, a general review of the finite element models of 13° wheel impact test available in literature is summarized according to the modeled portions of the test, wheel material, and the failure criteria.

Depending on the literature presented in Table 1.1, it can be concluded that the finite element modeling of the wheel, hub adapter structure having natural rubbers, and the tire have important roles for the finite element analysis. All authors used elasto-plastic material model and tetrahedron elements for the wheel models. Most of the authors modeled the hub adapter structure with natural rubbers. Elastic and Mooney-Rivlin with two parameters material models were used for the natural rubbers. But, a few authors modeled the impact test in which the tire consists of major components such as the tread, sidewall, steel beads, steel belts and body plies. Former studies also show that the shell and membrane elements can cause unrealistic deformations of the tire in the area of contact.

Moreover, it is concluded that 3D solid elements should be used for rubber parts of the tire. Rebar elements in the ABAQUS or beam elements in the LS-DYNA are used for the reinforcement elements of the tire; steel belts and body plies. Dynamic modeling of the pressure in the tire is a more realistic method than static modeling. Thus, the simple pressure airbag keyword of the LS-DYNA is used for dynamic modeling of the pressured air in the tire. A few authors considered the clamping load induced by the tightening torque on the bolt.

Table 1.1. General review of the finite element models of the 13° wheel impact test

Component		Authors					
		Riesner et al (1986)	Shang et al (2005)	Chang and Yang (2009)	Jigang and Guozh (2012)	Yuan et al (2012)	Ishikawa et al. (2014)
The parts of tire	Tread	No	Yes/3D elements	Yes/Shell elements	Not mentioned	Yes/No detail is given	Yes/3D elements
	Sidewall		Yes/Shell elements				
	Steel beads		No	No			
	Steel belts		No	No			Yes/Rebar elements
	Body plies		No	No			
	Pressure load		Dynamic	Static		Static	Static
Others	Hub adapter structure	No	No	Yes	Yes/ No detail is given	Yes	Yes
	Wheel material	6061-T6	A356	6061-T6	Aluminum Alloy	A356	A356
	Damage parameter (Failure criteria)*	TPW	EPS	TPW	VM	FPS	EPS

* TPW: Total plastic work, EPS: Effective plastic strain, VM: von Mises, FPS: First principal strain

The computational time of the wheel impact test simulations declared by some authors are listed in Table 1.2.

Table 1.2. The computational time of the 13° wheel impact test simulations

Definition	Authors	
	Shang et al (2005)	Ishikawa et al. (2014)
Central process unit, CPU, type of the computer	AMD Athlon 1.7 GHz	Intel Xeon E5645 2.40 GHz
Memory of the computer	1 GB	Not mentioned
Number of cores of the computer	1	8
Number of nodes of the FE model	140895 (with tire)	225892
Number of elements of the FE model	257840 (with tire)	137528
End or termination time of the simulation [sec]	~ 0.85 (with tire) 0.60 (without tire)	0.1
Computational time of the FE model (Hour)	72 (with tire) 28 (without tire)	~50 Hours

It is useful to mention that Ishikawa et al. (2014) and Shang et al (2005) verified their numerical simulations regarding plastic deformations by experimental studies.

In the current study, static and dynamic finite element models for the simulation of the wheel impact test defined in ISO7141 were developed for the AlSi7Mg and AlSi11Mg alloy wheels by considering all modeling methods of the impact test discussed above.

The dynamic model consisted of the wheel, complete hub adapter structure, and the tire having major components: the tread, sidewall, steel beads, steel belts and body plies. Natural rubber mounts of the hub structure were modeled as spring and damper elements. The dynamic model was used for the pressured air inside of the tire. Moreover, the clamping load induced by the tightening torque on the bolts was considered. The dynamic model was verified by using plastic deformation values of the wheel spoke that were obtained experimentally.

Some parts of the model were also simplified to reduce the computational time. 1D/2D finite element models of the complete hub adapter structures were formed and verified. In addition to these, a simplified tire model was developed and tested numerically.

Forty-one experimental impact tests were carried out for fourteen different AlSi11Mg and AlSi7Mg alloy wheels. The maximum von Mises stresses on the wheel during the impact were obtained from numerical simulations of these models. Box-plot statistical method was used to show the maximum von Mises stress predictions for both AlSi11Mg and AlSi7Mg alloy wheels.

The static model consists of the wheel with simplified tire and the lumped model of the hub adapter structure. Force-displacement curve and von Mises stresses distribution of the wheel according to the displacement of the impact point of the wheel are obtained by means of the static model. Force-displacement and strain energy -displacement functions are found. It is shown that the maximum von Mises stress on the wheel due to any impact load can be calculated by using energy approach instead of running the dynamic simulation.

CHAPTER 2

THEORETICAL BACKGROUND

2.1. Introduction

During the impact test of the light alloy wheel, an impact mass is released from a specified height onto a wheel with the pneumatic radial tire fixed on a standard test stand as detailed in this Chapter. To evaluate the deformation of the wheel during this period, the test components and their physical behaviors are introduced.

First, the characteristics of the standard test stand, wheel and pneumatic tire are presented. The composite structures of the tire are illustrated and their special terms are given. Then, to understand the physical behavior of the objects under the time dependent load, namely impact load, the equation of motion for lumped systems is summarized. Moreover, the most common damping types such as linear-viscous damping, Coulomb/dry friction damping, hysteretic/solid/structural damping and proportional/Rayleigh damping are explained.

Based on these results, time responses of linear and nonlinear lumped systems are written for single-degree-of-freedom and multi-degree-of-freedom systems.

Direct central impact and the coefficient of restitution along with impulse and momentum concepts are described by considering the two different particles having velocities in the same directions. It is known that coefficient of restitution is related with the energy transform mechanism of the impact and is based on the material characteristics of the particles.

Finally, the main subject of the impact test assessing the deformations of objects due to impact are examined both elastically and plastically by considering a vertical bar with a collar. This is a classical example to show the potential energy transform from falling collar to strain energy of the vertical bar. This concept is used in this thesis to simplify the analysis.

2.2. Impact Loading Test Machine

The road vehicles-light alloy wheels-impact test is specified by ISO7141. It is used to examine the lateral kerb impact collision properties of a wheel produced by light alloys completely or partially. In this test, impact loading test machine shown in Figure 2.1.

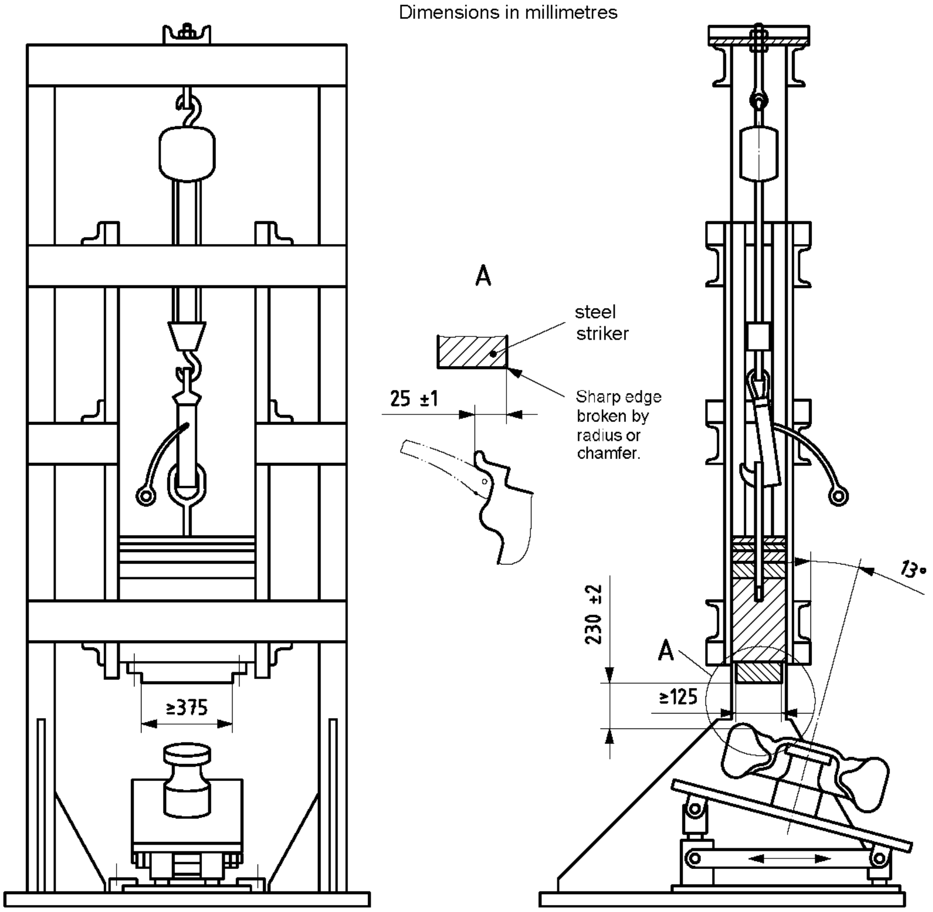

Figure 2.1 Impact loading test machine
(Source: ISO7141, 2005)

The test machine has a steel striker falling from 230±2 mm freely and having at least 125 mm wide and 375 mm long impact face as shown in Figure 2.1. The mass of the striker mass m is given as

$$m = 0.6W + 180 \tag{2.1}$$

where m is in kg within a tolerance of ± 2% and W is specified by vehicle manufacturer as the maximum static wheel load in kg.

Wheel hub adapter structure shown in Figure 2.1 is given in Figure 2.2 with dimensions. The geometry of the tire used in this test is specified by the vehicle manufacturer. If the tire is not specified, the smallest nominal section width tubeless radial-ply tire is used. Similarly, If the vehicle manufacturer does not specify the inflation pressure, it is taken as 200 kPa.

Calibration of the wheel hub adapter structure shown in Figure 2.2 is accomplished by using a calibration adapter. Vertical deflection under the calibration load is given in Figure 2.2 for calibration testing.

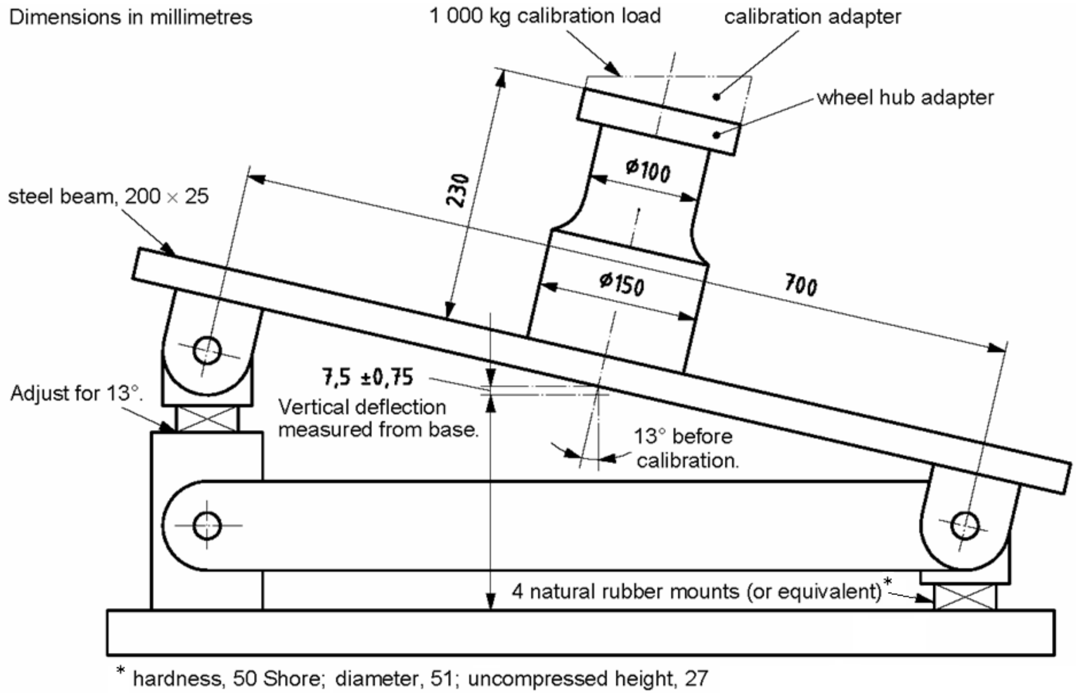

Figure 2.2 Wheel hub adapter structure
(Source: ISO7141, 2005)

According to ISO7141, the wheel is considered to have failed the test if any of the following apply:

a. Visible fracture(s) penetrate through a section of the center member of the wheel assembly;
b. The center member separates from the rim,
c. The tire loses all air pressure within 1 minute.

The wheel is not considered to have failed the test by deformation of the wheel assembly or by fractures in the area of the rim section by the face plate of the striker.

2.3. Wheel Characteristics

Passenger car wheels are generally manufactured in two types:

1. Sheet metal disc-type wheel shown in Figure 2.3.
2. Cast alloy wheel shown in Figure 2.4.

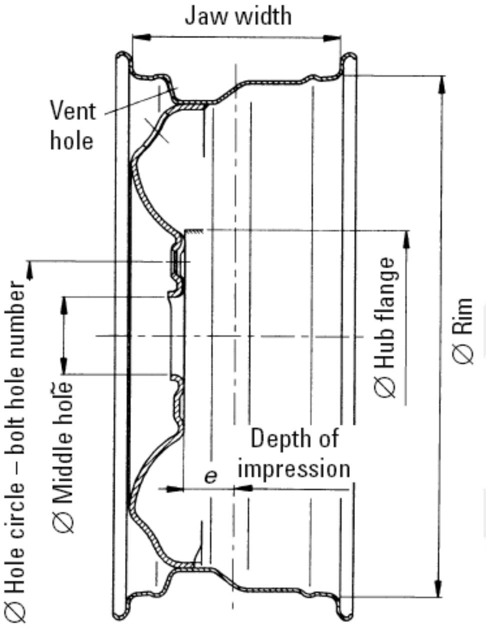

Figure 2.3. The sheet metal disc-type wheel
(Source: Reimpell et al., 2001)

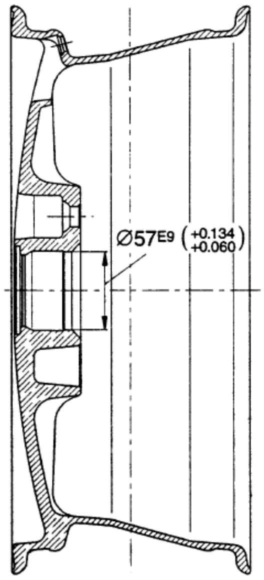

Figure 2.4. Cast alloy wheel
(Source: Reimpell et al., 2001)

Sheet metal disc wheels are commonly used due to their low cost and high stress limits. Its general geometrical features are shown in Figure 2.3. Depending on the design load of the wheel, cold-formable or band steel with a high elongation can be used. Sheet metal thicknesses range from 1.8 to 4.0 mm and 3.0 to 6.5 mm for the rim and the attachment faces, respectively.

Conversely, cast alloy wheels have the following advantages (Reimpell et al, 2001):

- lower mass;
- extensive styling options and better appearance;
- precise centering and limitation of the radial and lateral run out
- good heat transfer for brake-cooling

However, cast alloy wheels cost four times as much as sheet metal disc wheels.

It should be noted that both types of wheel must satisfy the same design rules, namely, impact tests, dynamic cornering test, etc.

2.4. Pneumatic Tire Characteristics

There are two types of pneumatic tires as follows (Bonnick and Newbold, 2005):

1. cross-ply or bias tire shown in Figure 2.5.
2. radial-ply tire shown in Figure 2.6.

It is clear that tires are made of composite materials having different laminated structures. Therefore, the term ply is used to classify them.

It can be seen from Figure 2.5 that the plies are placed one upon the other in the angles that are not in the radial directions. The angle between the cords is about 100°. Also, the angle between each cord and the tire bead and wheel rim is about 40°.

It is clear form Figure 2.6 that the cord plies of radial-ply tire have 90° to the direction of travel. This type of tire has a more flexible side wall, thus it has a greater contact area with the road when it is in cornering.

Figure 2.7 shows the difference between the first and second type of tire when they are under cornering conditions. It is remarkable that radial-ply tire has better road contact than bias tire.

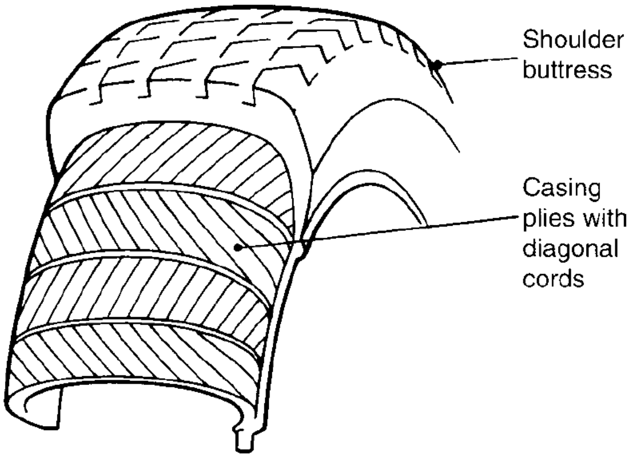

Figure 2.5. Cross-ply tire construction
(Source: Bonnick and Newbold, 2005)

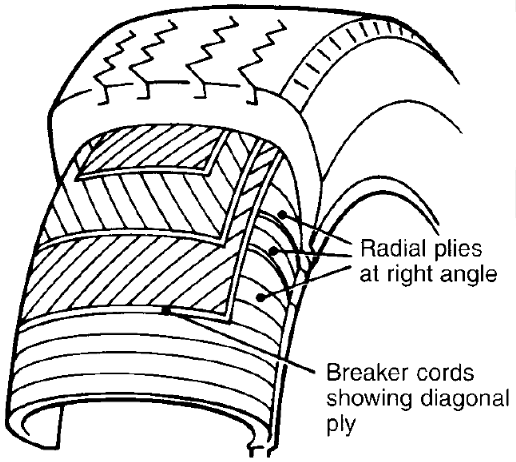

Figure 2.6. Radial-ply tire construction
(Source: Bonnick and Newbold, 2005)

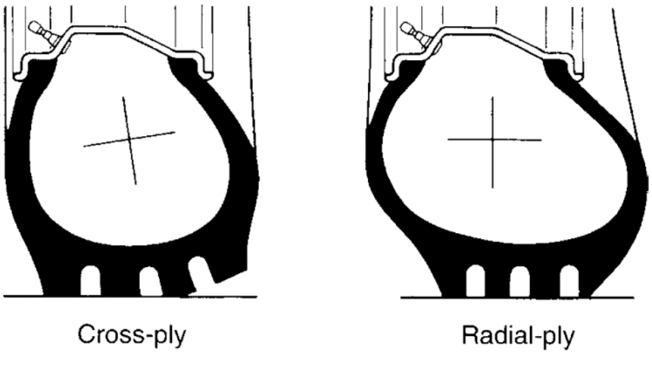

Figure 2.7. Cross-ply and radial-ply tires under cornering conditions
(Source: Bonnick and Newbold, 2005)

Details of the construction of a radial ply tire are shown in Figure 2.8. The beads consist of steel wires wrapped with fabric to form bundle in the shape of a ring. Also, they are wrapped by the ends of the plies. Radial plies are generally rayon for car tires due to the bonding ability, good fatigue resistance, and low cost. Other materials for plies are rayon, nylon or polyester. Beneath the tread, bracing plies have 2-3 bias layers of steel or 4-6 of rayon. Bracing plies have many critical functions such as preventing the tire from distortion due to centrifugal force and increasing the resistance to punctures.

The tread is made of a special rubber for wear resistance. It is important that different types of rubber are used for the treads, side walls, beads and fillers.

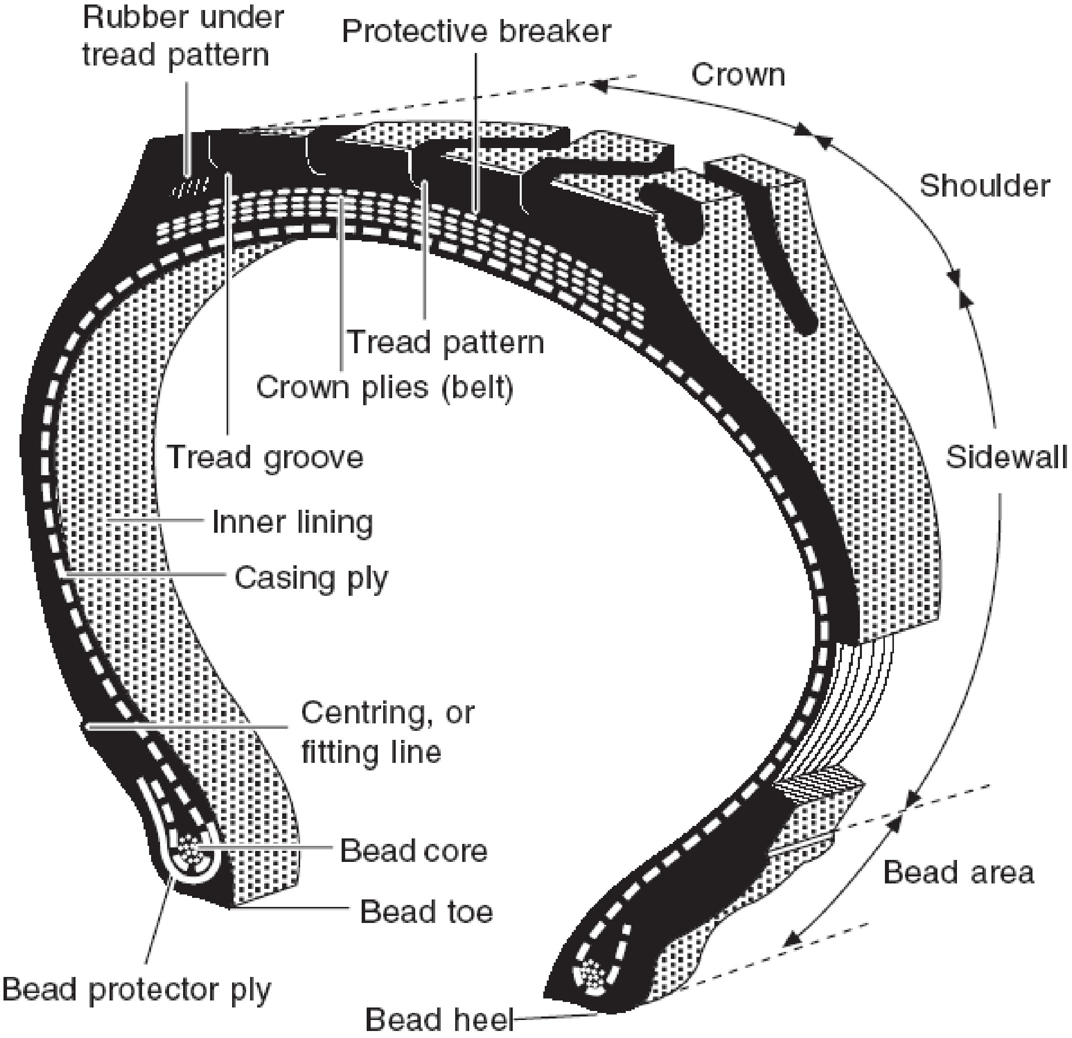

Figure 2.8. Construction of radial ply tire
(Source: Garretts et al., 2001)

2.5. Equation of Motion of Lumped Systems

When the system parameters are discrete sets of finite numbers, these systems are also named as discrete, lumped-parameter, or finite-dimensional systems. In these systems, point masses are separated by springs and dampers. The simplest one is a single degree of freedom system of which parameters can be described by scalar numbers. If the degree of freedom of the system is greater than one, it is called multi-degree-of freedom system. For this type of system, mass, damping and stiffness properties are given by matrices and displacements, velocities, and accelerations are represented by vectors. Thus, equation of motion is expressed by Yardımoğlu (2012) as,

$$[M]\{\ddot{q}(t)\} + [C]\{\dot{q}(t)\} + [K]\{q(t)\} = \{F(t)\} \tag{2.2}$$

where $\{q(t)\}$ is the displacement vector that is counterpart of $w(x, y, t)$, $\{F(t)\}$ is the force vector. Moreover, $[M]$, $[C]$, and $[K]$ are mass, damping, and stiffness matrices, respectively..

2.6. Damping

Several forms of damping models are available for modeling of energy dissipating mechanical systems. The most common models are as follows:

1. Linear-viscous damping
2. Coulomb or dry friction damping
3. Hysteretic damping or solid damping or structural damping
4. Proportional or Rayleigh damping

Another useful model of damping is related with the object vibrating in air or fluid. This model is called as air damping, quadratic damping, or velocity-squared damping. Moreover, displacement-squared damping occurs due to material damping.

Linear-viscous damping occurs when the parts have relative motions with respect to each other with lubricated contact. For this type of damping, damping force is directly proportional to the relative velocity between the parts. This is illustrated in Figure 2.9.

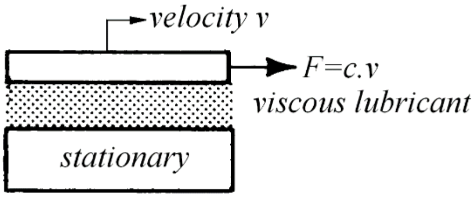

Figure 2.9. Simple model for viscous damping

When a body slides on a dry surface as shown in Figure 2.10, the damping due to friction is known as Coulomb or dry friction. Damping force is related with the dry friction coefficient, denoted by μ, of the contact surfaces.

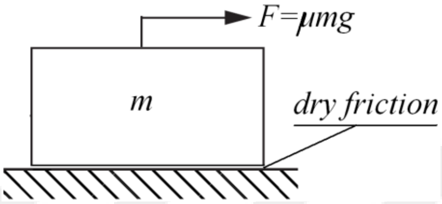

Figure 2.10. Simple model for Coulomb damping

Hysteretic damping is based on the energy lost due to the internal friction of the material per cycle under a harmonic load. Figure 2.11 shows an experimental stress–strain plot for one cycle of harmonically loaded material.

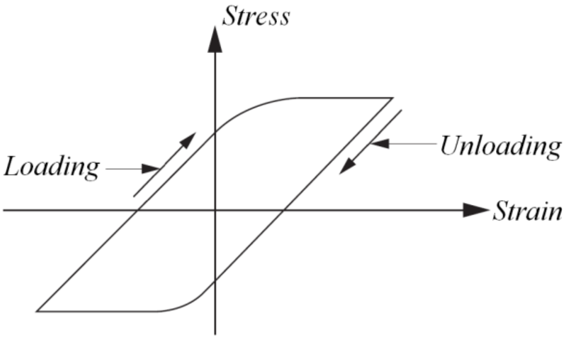

Figure 2.11. Hysteresis loop due to internal damping
(Source: Inman, 2014)

Energy loss per cycle is given by Inman (2014) as:

$$\Delta E = \pi \omega c_{eq} X^2 \tag{2.3}$$

where ω is forcing frequency, c_{eq} is equivalent viscous damping coefficient, and X is magnitude of the steady-state response. Equivalent viscous damping coefficient is given as

$$c_{eq} = \frac{h}{\omega} \tag{2.4}$$

where h is known as hysteretic damping constant which is given as:

$$h = k\gamma \tag{2.5}$$

where k and γ are stiffness coefficient and loss factor of the material, respectively. If equivalent viscous damping and stiffness forces are combined, complex stiffness coefficient k^* is found as follows:

$$k^* = k(1 + i\gamma) \tag{2.6}$$

For proportional damping, damping matrix $[C]$ in Equation (2.2) is a linear combination of stiffness matrix $[K]$ and mass matrix $[M]$ as (Inman, 2014):

$$[C] = \alpha\,[M] + \beta[K] \tag{2.7}$$

where α and β are coefficients. Damping matrix $[C]$ is also expressed as

$$[C_k] = \beta\,[K], \qquad [C_m] = \alpha\,[M] \tag{2.8.a,b}$$

Equations (2.8.a) and (2.8.b) are known as stiffness and mass proportional damping matrices, respectively. Figure 2.12 illustrates the Equations (2.7), (2.8.a), and (2.8.b) as r^{th} damping ratio versus r^{th} natural frequency.

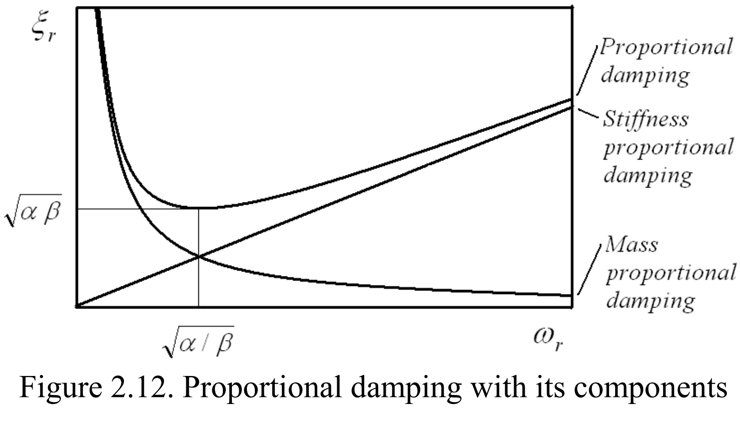

Figure 2.12. Proportional damping with its components

2.7. Time Response of Linear Lumped Systems

2.7.1. Single-Degree-of-Freedom Systems

For a single-degree-of-freedom system shown in Figure 2.13, Equation (2.2) is reduced to the following scalar form:

$$m\,\ddot{x}(t) + c\,\dot{x}(t) + k\,x(t) = F(t) \tag{2.9}$$

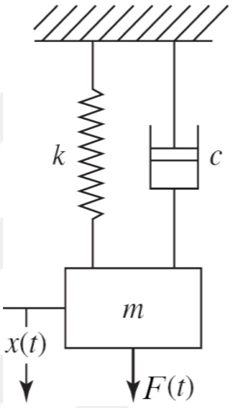

Figure 2.13. A single-degree-of-freedom system

Time response *x*(*t*) of an under damped system to arbitrary input *F*(*t*) is given by Inman (2014) as

$$\begin{aligned} x(t) &= \frac{1}{m\omega_d}\exp(-\xi\omega_n t)\int_0^t [F(\tau)\exp(\xi\omega_n\tau)\sin\omega_d(t-\tau)\,d\tau \\ &= \frac{1}{m\omega_d}\int_0^t F(t-\tau)\exp(-\xi\omega_n\tau)\sin\omega_d\tau\,d\tau \end{aligned} \tag{2.10}$$

where ω_n is the natural frequency, ξ is the damping ratio and ω_d is damped natural frequency. All these are given as follows:

$$\omega_n = \sqrt{k/m} \tag{2.11}$$

$$\xi = \frac{c}{c_{cr}} = \frac{c}{2m\omega_n} = \frac{c}{2\sqrt{km}} \tag{2.12}$$

$$\omega_d = \omega_n\sqrt{1-\xi^2} \tag{2.13}$$

2.7.2. Multi-Degree-of-Freedom Systems

As an example, three-degree-of-freedom system is shown in Figure 2.14.

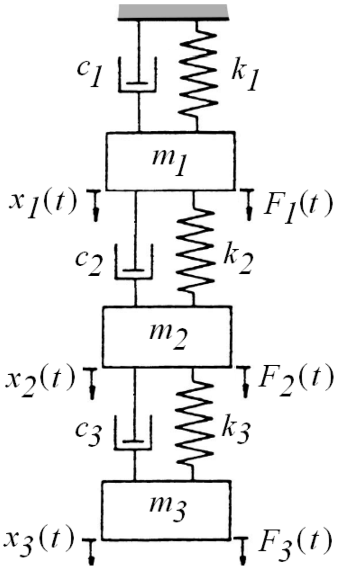

Figure 2.14. A three-degrees-of-freedom system

If the *n*-degree-of-freedom system given in Equation (2.2) has proportional damping, Equation (2.2) can be written in the form of independent modal equations (Meirovitch, 2000)

$$\ddot{\eta}_r(t) + 2\xi_r\omega_r\dot{\eta}_r(t) + \omega_r^2\eta_r(t) = N_r(t), \quad r = 1,2,...n \tag{2.14}$$

where r^{th} modal force $N_r(t)$ is given as

$$N_r(t) = \{u_r\}^T\{F(t)\}, \quad r = 1,2,...n \tag{2.15}$$

in which $\{u_r\}$ is the r^{th} modal vector.

Solution of Equation (2.14) to arbitrary input $\{F(t)\}$ is simply

$$\eta_r(t) = \frac{1}{\omega_{dr}} \int_0^t N_r(t-\tau)\exp(-\xi_r \omega_r \tau)\sin\omega_{dr}\tau \, d\tau, \quad r = 1,2,...n \tag{2.16}$$

where ω_r, ξ_r, ω_{dr} are r^{th} natural frequency, damping ratio and damped natural frequency, respectively.

2.8. Time Response of Non-Linear Lumped Systems

2.8.1. Single-Degree-of-Freedom Systems

Since nonlinear systems are much more difficult to solve, numerical simulation is introduced in this section. The differences between linear and nonlinear systems are summarized as follows (Inman, 2014):

1. A nonlinear system has more than one equilibrium point and each may be either stable or unstable.
2. Steady-state response of a nonlinear system does not always exist, and the solution is strongly dependent on the initial conditions.
3. The oscillation period of a nonlinear system depends on the initial conditions, the amplitude of excitation, and the physical parameters.
4. Resonance in nonlinear systems may occur at excitation frequencies that are not equal to the linear system’s natural frequency.
5. Superposition principle cannot be used in a nonlinear system.
6. In a nonlinear system, a harmonic excitation may cause a non-periodic or chaotic response.

The general equation of motion for a single-degree-of-freedom nonlinear system may be written as

$$\ddot{x}(t) + f(x(t), \dot{x}(t)) = F(t) \tag{2.17}$$

where $f(x(t), \dot{x}(t))$ may be linear or nonlinear, and forcing function $F(t)$ may be in any form. It should be noted that acceleration coefficient is unity. Equation (2.17) can be expressed in state space form as

$$\begin{aligned} \dot{x}_1(t) &= x_2(t) \\ \dot{x}_2(t) &= -f(x(t), \dot{x}(t)) + F(t) \end{aligned} \tag{2.18}$$

State space vector $\{x(t)\}$ is given as

$$\{x(t)\} = \begin{bmatrix} x_1(t) \\ x_2(t) \end{bmatrix} \tag{2.19}$$

Equation (2.18) can be written by using Equation (2.19) as

$$\{\dot{x}(t)\} = \{F(x(t)\} + \{f(t)\} \tag{2.20}$$

where

$$\{F(\{x(t)\})\} = \begin{bmatrix} x_2(t) \\ -f(x_1(t), x_2(t)) \end{bmatrix} \tag{2.21}$$

$$\{f(t)\} = \begin{bmatrix} 0 \\ F(t) \end{bmatrix} \tag{2.22}$$

The Euler integration method can be used for the solution of Equation (2.20),

$$\{x(t_{i+1})\} = \{x(t_i)\} + \{F(\{x(t_i)\})\}\Delta t + \{f(t_i)\}\Delta t \tag{2.23}$$

where the time step is $\Delta t = t_{i+1} - t_i$.

2.8.2. Multi-Degree-of-Freedom Systems

The classical eigenvalue methods are not suitable for nonlinear dynamic analysis of the system shown in Figure 2.15. (Ginsburg and Gellert, 1980). Therefore, efficient algorithms for the direct numerical integration of the equations of motion are needed.

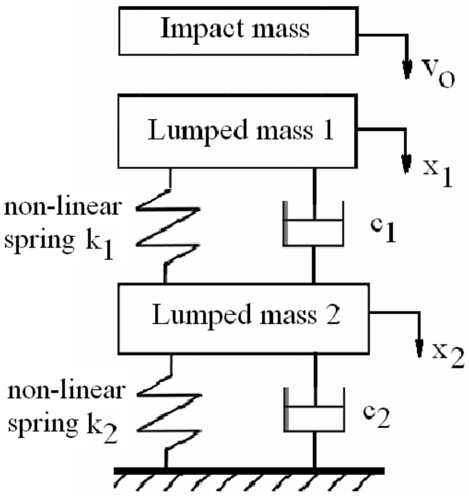

Figure 2.15. A two-degrees-of-freedom system

2.9. Impulse and Momentum-Central Impact

Let us consider a force $\vec{F}$ acting on a particle of mass *m*. Newton's second law can be written in the form

$$\vec{F} = \frac{d}{dt}(m\vec{v}) \tag{2.24}$$

where $m\vec{v}$ is linear momentum of the particle. Multiplying both side of Equation (2.24) by *dt* and integrating from t_1 to t_2, it yields,

$$m\vec{v}_1 + \int_{t_1}^{t_2} \vec{F} dt = m\vec{v}_2 \tag{2.25}$$

The integral in Equation (2.25) is known as linear impulse $\vec{I}_{1\rightarrow 2}$. Also, if the interval of time $\Delta t = t_2 - t_1$ is a very short, the force is called as impulsive force. If $\vec{I}_{1\rightarrow 2} = 0$ in Equation (2.25) then it reduces to

$$m\vec{v}_1 = m\vec{v}_2 \tag{2.26}$$

Equation (2.26) is known as conservation of linear momentum.

Collision of two particles is an example for impulse-momentum application. There are two types of central impacts of two particles depending on their initial velocity directions as shown in Figure 2.16. The line of impact is determined by using the contact point of the particles. Thus, line of impact passes through from center of the particles.

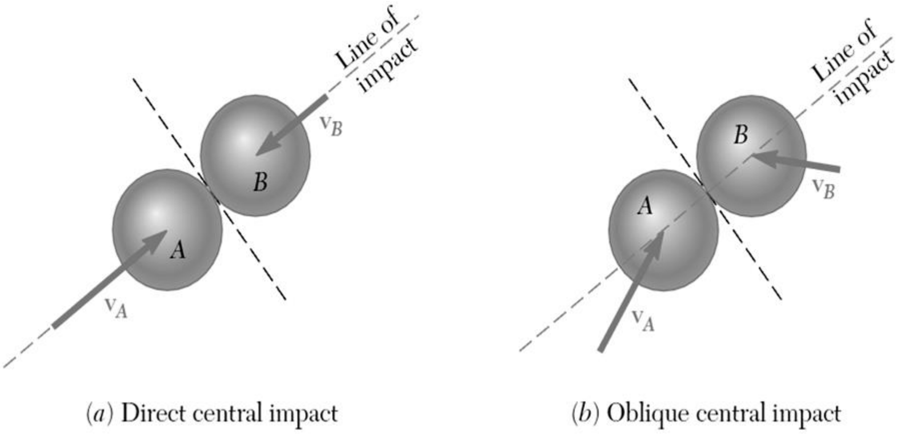

Figure 2.16. Central Impact types
(Source: Beer et al, 2010)

Now, direct central impact is detailed. Assuming $v_A > v_B$, collisions of two particles A and B shown in Figure 2.17 is considered. In first step, particle A strikes particle B. In second step, particles A and B deform and have a common velocity u. Then, the two particles can return to their original shape or can have permanent deformation depending on the magnitude of the impact forces occurred in second step. This time is called the restitution period.

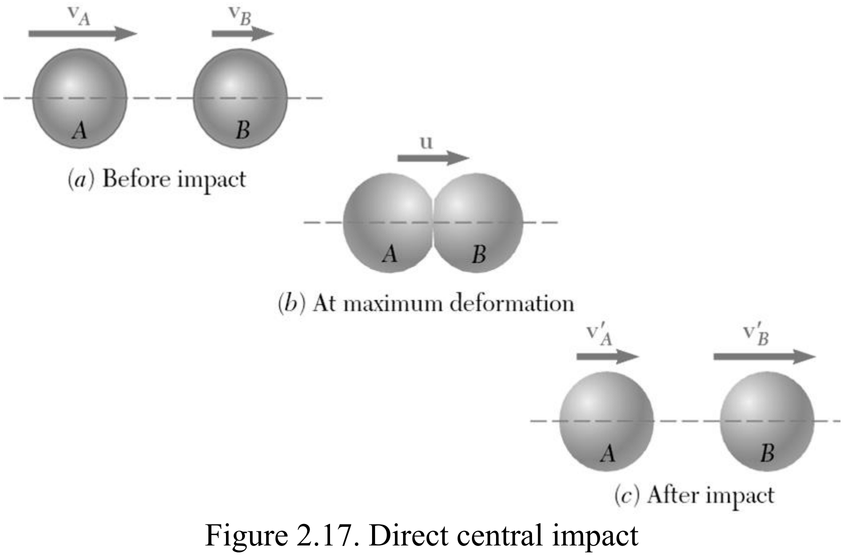

Figure 2.17. Direct central impact
(Source: Beer et al, 2010)

If the total momentum of the two particles having central impact is conserved, the scalar form, which is based on a rule that right is positive and left is negative, can be used as

$$m_A v_A + m_B v_B = m_A v'_A + m_B v'_B \tag{2.27}$$

In this subject, deformation and restitution times shown in Figure 2.18 are the most critical. During the deformation, the following equation can be written for particle A

$$m_A v_A - \int P dt = m_A u \tag{2.28}$$

Notation can be seen from Figure 2.18. Also, during the period of restitution for particle A

$$m_A u - \int R dt = m_A v'_A \tag{2.29}$$

In general,

$$\int P dt > \int R dt \tag{2.30}$$

The coefficient of restitution *e* is defined as

$$e = \frac{\int R dt}{\int P dt} \tag{2.31}$$

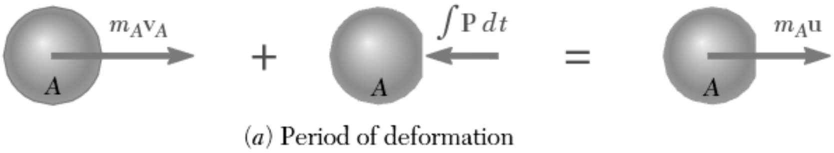

(*a*) Period of deformation

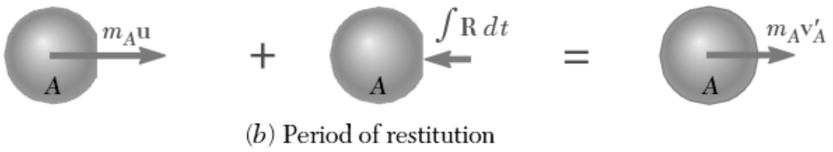

(*b*) Period of restitution

Figure 2.18. Periods of deformation and restitution
(Source: Beer et al, 2010)

Due to Equation (2.30), e is always between 0 and 1 and depends on the particles geometry, materials and velocities. Solving Equations (2.28) and (2.29) for the two impulses and substituting into Equation (2.31), the coefficient of restitution e becomes

$$e = \frac{u - v'_A}{v_A - u} \tag{2.32}$$

Similarly, for particle B,

$$e = \frac{v'_B - u}{u - v_B} \tag{2.33}$$

Since the Equations (2.32) and (2.33) are equal to each other, they are also equal to the quotient obtained by adding, respectively, their numerators and their denominators as

$$e = \frac{(u - v'_A) + (v'_B - u)}{(v_A - u) + (u - v_B)} = \frac{v'_B - v'_A}{v_A - v_B} \tag{2.34}$$

There are three cases depending on the value of the coefficient of restitution e:

1. Perfectly elastic impact, if $e = 1$,
2. Elasto-plastic impact, if $0 < e < 1$,
3. Perfectly plastic impact, if $e = 0$.

2.10. Elastic Deformation of Structures Under Impact Load

Structures may have several geometrical components such as bar, beam, plate, shell etc. Elastic deformation analysis of aforementioned members has several methods depending on the problem. The general approach is based on energy method.

In order to obtain an analogical procedure for this topic, the system having a vertical bar *AB* fixed at the upper end and a collar with mass *M* shown in Figure 2.19 can be considered. The collar is initially at rest and falls from height *h* measured from the bottom end of the bar *AB*. It can be seen from Figure 2.19 that the vertical bar *AB* has a flange at the bottom end *B* to stop the collar.

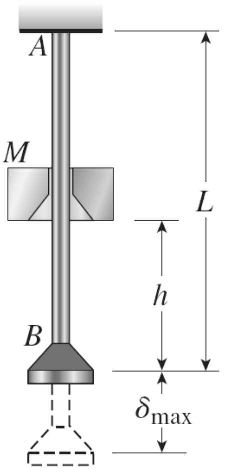

Figure 2.19. Impact load on a bar due to a falling object of mass *M*
(Source: Gere, 2004)

When the collar hits the flange, the bar starts to elongate. After a very short time, both the flange and the collar reach maximum deformation position. Thereafter, the bar shortens and lengthens, repeatedly. Due to the material damping effect, the motion of the bar ends, namely, the bar comes to rest with the mass M on the flange.

The following assumptions are made to simplify the analysis:

1. Bar *AB* deforms elastically,
2. Kinetic energy of the collar transforms into strain energy in the bar *AB*.
3. Changes in potential energy of the bar due to the elongation are neglected.
4. Damping is neglected.

Now, the maximum elongation of the bar $\delta_{\max}$ shown in Figure 2.19 is found by equating the potential energy of the collar to the maximum strain energy of the bar as

$$Mg(h+\delta_{\max}) = \frac{EA\delta_{\max}^2}{2L} \tag{2.35}$$

where *E* is Young's modulus, *g* is gravitational acceleration, *A* and *L* are cross section area and length of the bar, respectively. Equation (2.35) is solved for the positive root to find the maximum deflection

$$\delta_{\max} = \frac{MgL}{EA} + \left[\left(\frac{MgL}{EA}\right)^2 + 2h\left(\frac{MgL}{EA}\right)\right]^{1/2} \tag{2.36}$$

It should be noted that the elongation δ_{st} under static load $W=Mg$ is given by

$$\delta_{st}=\frac{WL}{EA}=\frac{MgL}{EA} \tag{2.37}$$

Equation (2.36) can be written in terms of δ_{st} by using Equation (2.37)

$$\delta_{\max}=\delta_{st}+[\delta_{st}^2+2h\delta_{st}]^{1/2} \tag{2.38}$$

If $h>>\delta_{st}$ then

$$\delta_{\max}=[2h\delta_{st}]^{1/2} \tag{2.39}$$

On the other hand, the energy conversation of the collar can be written as

$$0.5Mv^2=Mgh \tag{2.40}$$

Therefore, h in Equation (2.39) can be expressed in terms of velocity of collar v

$$h=v^2/2g \tag{2.41}$$

Substituting Equations (2.37) and (2.41) into Equation (2.39) yields

$$\delta_{\max}=\sqrt{\frac{M\,v^2L}{EA}} \tag{2.42}$$

The ratio of the dynamic maximum displacement of a structure to the static displacement for the same load is called an impact factor and can written as follows

$$\text{Impact Factor}=\frac{\delta_{\max}}{\delta_{st}} \tag{2.43}$$

Equation (2.38) can be expressed in terms of Impact Factor to see the dynamic load effect.

If the collar released from *h*=0, this type of loading is called as suddenly applied load. For this type of loading, maximum displacement is found by substituting *h*=0 into the Equation (2.38)

$$\delta_{\max} = 2\,\delta_{st} \tag{2.44}$$

Due to the assumption for material behavior, deformation of the bar *AB* remains in the elastic region. Maximum elastic strain due to the dynamic load applied by collar is

$$\varepsilon_{\max} = \frac{\delta_{\max}}{L} \tag{2.45}$$

Maximum stress in the bar can be calculated by using Hook's law as

$$\sigma_{\max} = E\varepsilon_{\max} = E\frac{\delta_{\max}}{L} \tag{2.46}$$

By following the same procedure used for displacements,

$$\sigma_{st} = \frac{E\delta_{st}}{L} \tag{2.47}$$

$$\sigma_{\max} = \sigma_{st} + [\sigma_{st}^2 + \frac{2hE}{L}\sigma_{st}]^{1/2} \tag{2.48}$$

If $h >> \delta_{st}$

$$\sigma_{\max} = \sqrt{\frac{2hE\sigma_{st}}{L}} = \sqrt{\frac{M\,v^2 E}{AL}} \tag{2.49}$$

Note that as the kinetic energy increases the stress also increases. The stress in the bar $\sigma = W\,/\,A$ is independent of the length of the bar L and Young's modulus E for static load, but for impact load, an increase in L of the bar reduces the stress and an increase in E of the bar decreases the stress.

2.11. Plasticity

2.11.1. Stress-Strain Curve

A test specimen shown in Figure 2.20 is produced and inserted into the tensile machine which applies the axial load gradually. Test machine provides the data on the stress-strain behavior of the material of specimen. A typical stress-strain curve is shown in Figure 2.21.

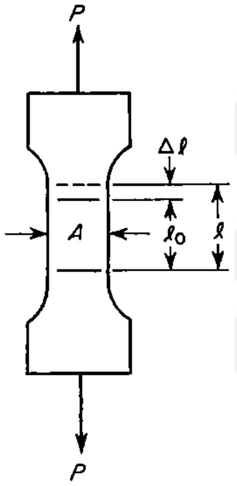

Figure 2.20. Tensile test specimen under the axial load
(Source: Mendelson, 1968)

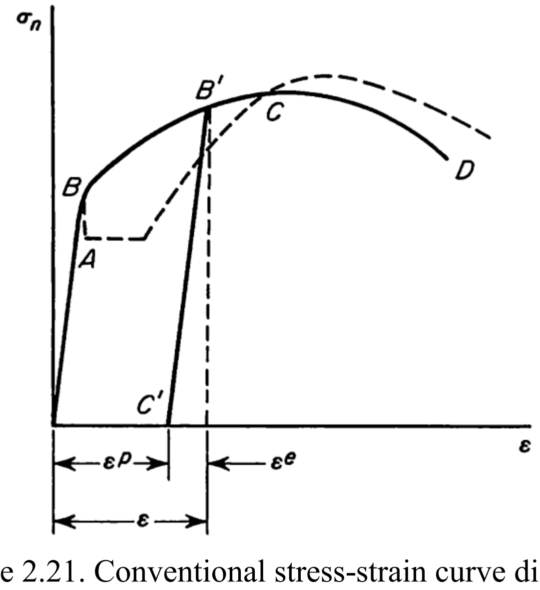

Figure 2.21. Conventional stress-strain curve diagram
(Source: Mendelson, 1968)

The vertical axis of the plot shown in Figure 2.21 is known as nominal stress, and gives as

$$\sigma_n = \frac{P}{A_0} \tag{2.50}$$

where A_0 is the original cross sectional area. Also, the horizontal axis of the same plot is called as the conventional or engineering strain and written as

$$\varepsilon = \frac{l - l_0}{l_0} \tag{2.51}$$

where l and l_0 are shown in Figure 2.21. It is clear that l is the original length.

It can be seen from Figure 2.21 that the relation between stress and strain is linear in the first region between origin and the point A that is proportional limit. Thus, in this region, the linear theory of elasticity based on Hook's law is valid. Also, until point B that is called elastic limit or yield point the material still remains in elastic region. This means that if the load is removed, the specimen returns to its original length. However, in most material the proportional limit A and elastic limit B are very close.

After point B, the deformation of the specimen is permanent, so it is called as plastic deformation. It can also be seen from the same figure that the slope of the curve reduces when the strain increases. The behavior of the material in the region from B to C is known as work hardening or strain hardening. The stress necessary in this region is called flow stress. When the curve reaches to point C, the load P is at the maximum. After this point of instability, the specimen "necks down" rapidly and fractures at D. The stress distribution between C and D is the state of triaxial.

Eventually, point C is a limit for the useful part of the tensile test as far as plasticity theory. The stress at the maximum load point C is called the tensile strength, or ultimate stress. If the load is removed at any point between B and C, for example B', then point B' moves to C' during the unloading as shown in Figure 2.21. Thus, although the strain at point B' is ε, the strain at point C' is ε^p which is plastic strain. Therefore,

$$\varepsilon = \varepsilon^e + \varepsilon^p \tag{2.52}$$

where ε is total strain and ε^e is elastic strain.

If the specimen is reloaded from point C', the unloading line B'C' is not followed exactly, the reloading path has very minor deviations. This is known as hysteresis loop. Plastic flow does not start again until the point B' is reached. With further loading, the stress-strain curve is continued along B'C as if no unloading had occurred. Point B' can thus be considered as a new yield point for the strain-hardened material.

2.11.2. Main Concepts of Plasticity

Plasticity theory has three main parts:

1. Yield criterion is based on a yield function *F* as function of material characteristics, plastic work per unit volume associated with hardening rule. If the yield function is equal to zero, yield occurs. Several yield surfaces based on different approaches are shown in Figure 2.22.
2. Flow rule is related with plastic potential Q which represents a surface and a plastic strain rate vector $\acute{\varepsilon}_p$ perpendicular to mentioned surface.
3. Hardening rule has two types: kinematic and isotropic hardening. In the first, the yield surface size and shape do not change, but the center axis of the yield surface translates as illustrated in Figure 2.23.a. In the second one, the yield surface size changes, but the center axis and the general shape of the yield surface do not change as shown in Figure 2.23.b.

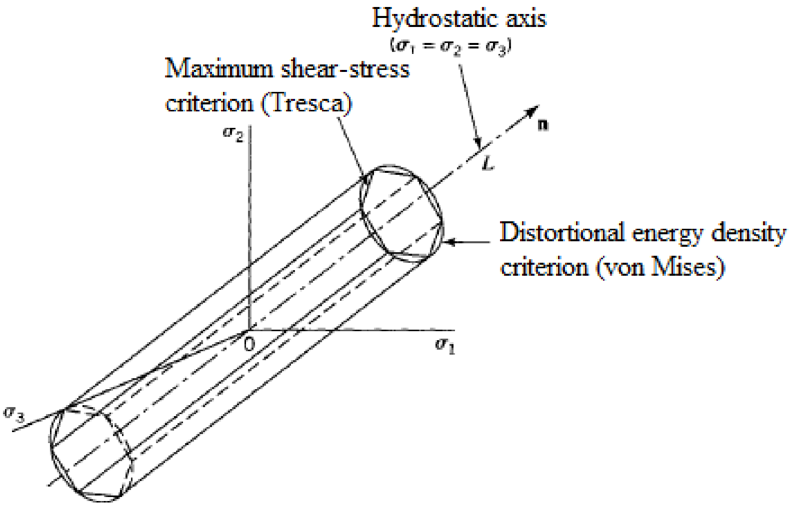

Figure 2.22. Yield surface in principal stress space
(Source: Boresi and Schmidt, 2003)

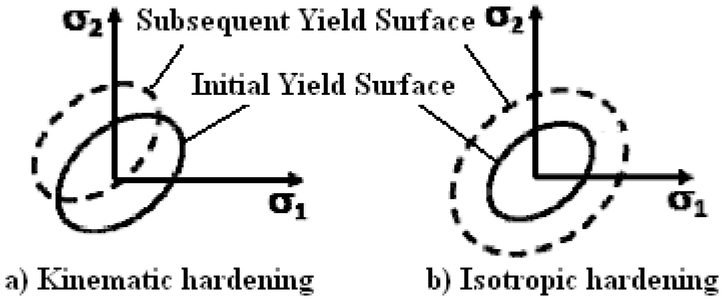

Figure 2.23. Kinematic and Isotropic hardening
(Source: ANSYS, 2009)

2.11.3. Idealization of the stress-strain curve

Figure 2.24 shows idealized curves as well as corresponding dynamic models which can be used to describe the material behavior.

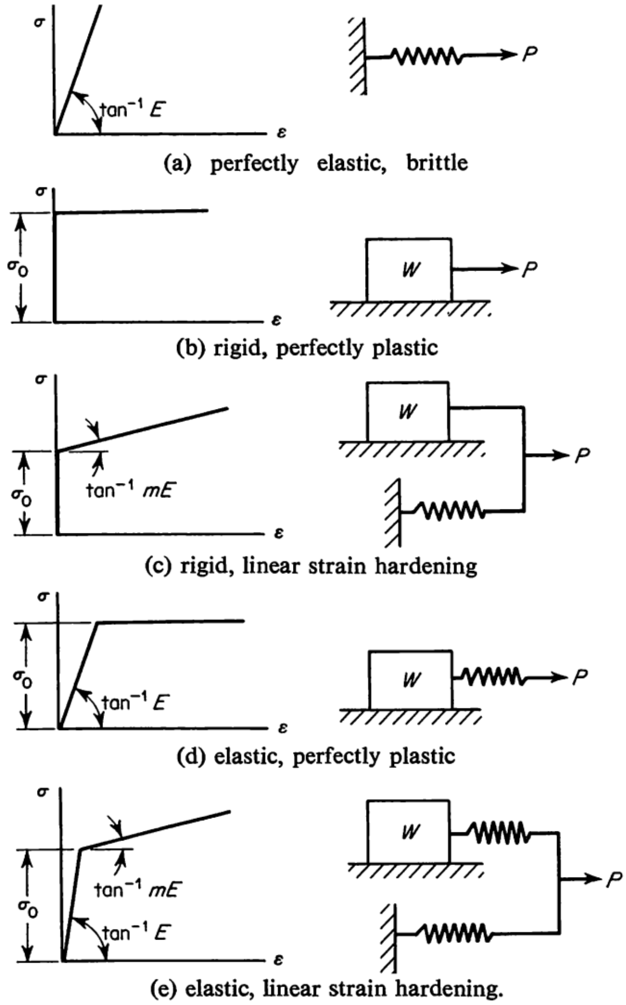

Figure 2.24. Idealized stress-strain curves
(Source: Mendelson, 1968)

2.11.4. Effect of strain rate

The effect of increasing the strain rate is generally to increase the tensile yield, as shown in Figure 2.25. For materials with a lower yield, such as mild steel, the stress-strain curve may approach that of a perfectly plastic material.

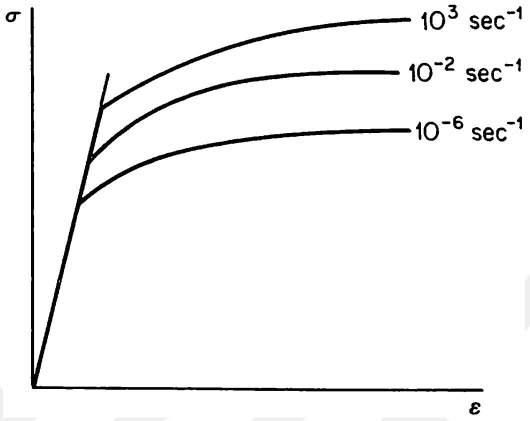

Figure 2.25. Effect of strain rate
(Source: Mendelson, 1968)

2.12. Plastic Deformation of Structures under Impact Load

This section is an extension of the former section for plastic deformation. Therefore, the tension test diagram for a specimen under axial load *P* and with elongation δ shown in Figure 2.26 is considered.

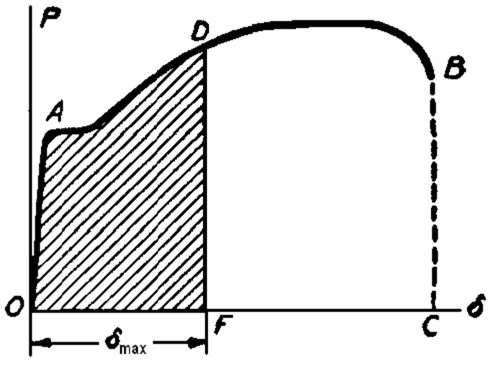

Figure 2.26. Tension test diagram
(Source: Timoshenko, 1940)

It is known that the shaded area in Figure 2.26 is equal to elasto-plastic energy to produce a elasto-plastic displacement $\delta_{\max}$ in the tension test specimen. For this case, the former assumptions are modified as follows:

1. Bar AB deforms elasto-plastically,
2. Kinetic energy of the collar transforms into strain energy in the bar AB.
3. Changes in potential energy of the bar due to the elongation are neglected.
4. Damping is neglected.

Now, the maximum elongation of the bar $\delta_{\max}$ shown in Figure 2.19 is found by equating the potential energy of the collar to the maximum strain energy of the bar as

$$Mg(h+\delta_{\max}) = \int_0^{\delta_{\max}} P(\delta)\, d\delta \tag{2.53}$$

The right side of Equation (2.53) corresponds to area OADF in Figure 2.26. The maximum elongation of the bar $\delta_{\max}$ is found from this equation. After finding $\delta_{\max}$, corresponding axial force P_{max} and elastic deformation $\delta_{\text{max-e}}$ are obtained. Therefore, considering the equation $\delta_{\max} = \delta_{\text{max-e}} + \delta_{\text{max-p}}$, plastic deformation $\delta_{\text{max-p}}$ is calculated. Finally, corresponding elastic and plastic stresses are determined.

2.13. Summary of FEM-ANSYS Workbench LS-DYNA/LS-Prepost

2.13.1. Overview

ANSYS is a software for finite element simulations. It has structural, mechanical, fluid, and electromagnetic simulation capabilities. ANSYS Classical has two different types of usage: 1) Graphic User Interface (GUI), 2) ANSYS Parametric Design Language (APDL). On the other hand, ANSYS Workbench (hereafter Workbench) has a more user friendly GUI.

LS-DYNA is another software for finite element simulations, but is especially developed for highly nonlinear, transient dynamic finite element analysis using explicit time integration. Workbench Explicit Dynamic is one of the more well-known and user friendly software. LS-PrePost is a preprocessor for LS-DYNA and is distributed freely.

In this thesis, static and explicit dynamic finite element simulations are carried out using “static structural” and “explicit dynamic” applications of Workbench, respectively. Moreover, some finite element model features in LS-DYNA, such as simple airbag, as used in this thesis, are not supported in Workbench. Therefore, aforementioned difficulties are overcome by LS-PrePost.

The objectives of this section are to present the Finite Element Method, Workbench, and LS-PrePost for LS-DYNA.

2.13.2. Basis of Finite Element Method

The finite element method is a well known numerical procedure for solving a wide range of engineering problems such as stress analysis, etc. Basic procedure of this method is outlined in next paragraphs by using Figure 2.27.

Finite element method is based on the division of the entire body into small and geometrically simple bodies which are known as finite elements. Depending on the problem type, physical equations of each element such as equilibrium equations are obtained.

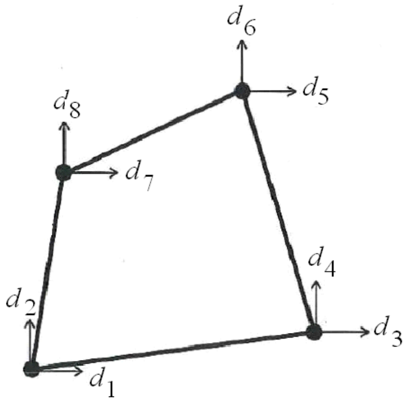

Figure 2.27. The nodal displacements of a 2D 4-node quadrilateral element (Source: Lee, 2014)

The elements are connected by the nodes located on the vertices and edges of elements. Discrete values at the nodes such as displacements are nodal unknowns. Nodal unknowns are related with the element shape functions. The element displacement vector $\{d\}$ is written as

$$\{d\} = \{d_1\, d_2\, d_3\, d_4\, d_5\, d_6\, d_7\, d_8\}^T \tag{2.54}$$

The relationship between the element displacements vector $\{d\}$ and the displacement vector $\{u(x,y)\}$ over the element is provided by shape function matrix $[N(x,y)]$

$$\{u(x,y)\} = [N(x,y)]\{d\} \tag{2.55}$$

where $\{u(x,y)\}$ is 2x1 due to the x and y directions. Therefore, $[N(x,y)]$ is 2x8. Since the element shown in Figure 2.27 has interpolating points on the vertices of the element, the shape function of the element is linear. When the element has linear shape function it is called a linear element, first-order element, or a lower-order element. If a node is added on the middle of each edge of the element; called the midside nodes, the element is called a quadratic element, second-order element, or a higher-order element. In these cases, the shape function of the element has quadratic form.

Equilibrium equations for each finite element is

$$\{f\} = [k]\{d\} \tag{2.56}$$

where $\{f\}$ and $[k]$ are element force vector and stiffness matrix, respectively.

Displacement vector of the entire body $\{D\}$ is combination of the element displacement vectors $\{d\}$ and obtained by assemble procedure. Similarly, if the capital letters are used for the entire body, the system of equilibrium equations of the entire body has the following form,

$$\{F\} = [K]\{D\} \tag{2.57}$$

where {F} and [K] are external force vector and stiffness matrix of the entire body. The size of Equation (2.57) is equal to total number of nodal freedoms. Boundary conditions can be applied to Equation (2.57) by several methods, and then the size of [K] changes.

The solution of modified Equation (2.57) gives the displacement vector of the entire body. After the displacements are known, the strain and stress at any point can be found.

If the stiffness matrix is a function of displacements, the static analysis is called nonlinear static analysis. A nonlinear structural behavior occurs due to geometric, material nonlinearities, and changing contact status (ANSYS, 2015).

Large deformation and stress stiffening are two main types of geometric nonlinearity. If the displacements or rotation of the structure is large compared to its dimension to such an extent that its original dimensions, position, and loading direction change significantly, this kind of state causes nonlinearity. For instance, a fishing rod having a low lateral stiffness under a lateral load has nonlinear stiffness behavior as shown in Figure 2.28. A structure that has little or no stiffness in one direction, while having considerable stiffness in another direction, exhibits this behavior too. For example, cables, membranes, or spinning structures have stress stiffness behavior (Madenci and Güven, 2006).

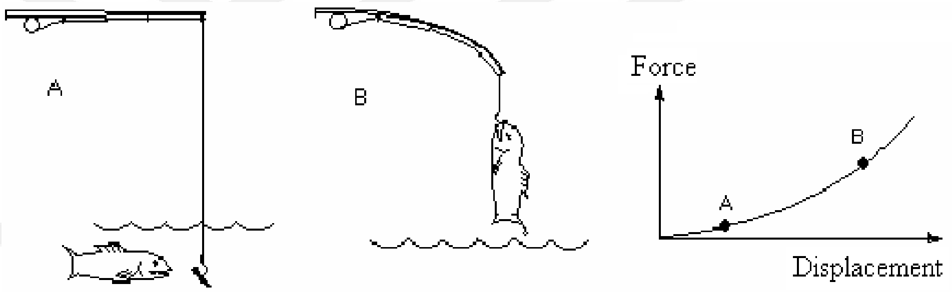

Figure 2.28. The nonlinear stiffness behavior of fishing rod.
(Source: ANSYS, 2015)

Material nonlinearity occurs due to the nonlinear stress-strain relationship, such as metal plasticity explained in Section 2.11. When the contact status of the bodies changes as shown in Figure 2.29, contact type nonlinearity occurs.

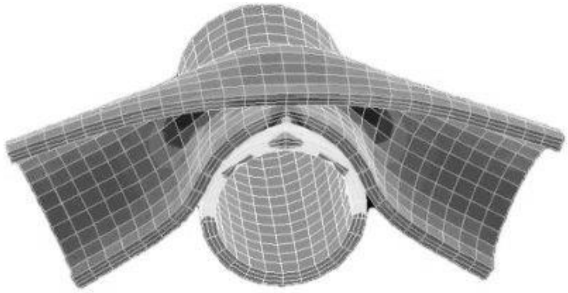

Figure 2.29. The nonlinear stiffness behavior due to status of contact.
(Source: ANSYS, 2015)

Equation (2.57) is solved directly for a linear analysis. However, for a nonlinear analysis, an iterative process called the Newton-Raphson method can be used to solve the problem. This method is presented in this Chapter.

Finite element method is also very effective for dynamic problems. The most common ones are presented as follows:

- **Modal analysis**: Equation (2.2) is solved for homogeneous case to find the natural frequencies and mode shapes. Damping is detailed in Section 2.6.
- **Transient structural analysis**: Equation (2.2) can be solved by using a direct integration method called an implicit integration method. Explicit dynamic analysis based on conservation of mass, momentum and energy in Lagrange coordinates.
- **Harmonic response analysis**: Equation (2.2) is solved for sinusoidal force of known frequency to determine the steady state response.

Finite element method requires hourglass control. Hourglass modes are zero-energy modes of deformation that produce zero strain and no stress. The energy is dissipated by the hourglass forces. It occurs when solid, shell, and thick shell elements have single integration point. Triangular shells and tetrahedral solid elements do not have hourglass modes. Typical hourglass modes are shown in Figure 2.30.

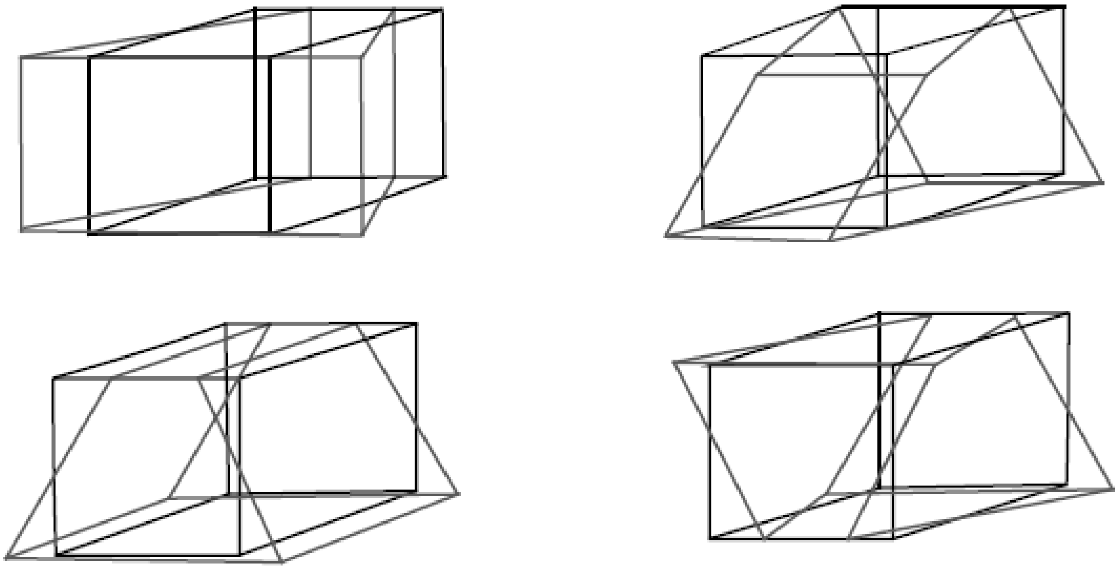

Figure 2.30. Typical hourglass modes of an eight-node element.
(Source: LSTC, 2015)

2.13.3. ANSYS Workbench

The Workbench uses GUI shown Figure 2.31. The main steps for static structural analysis can be seen from the small window appeared at the rights side of the screen under the title A.

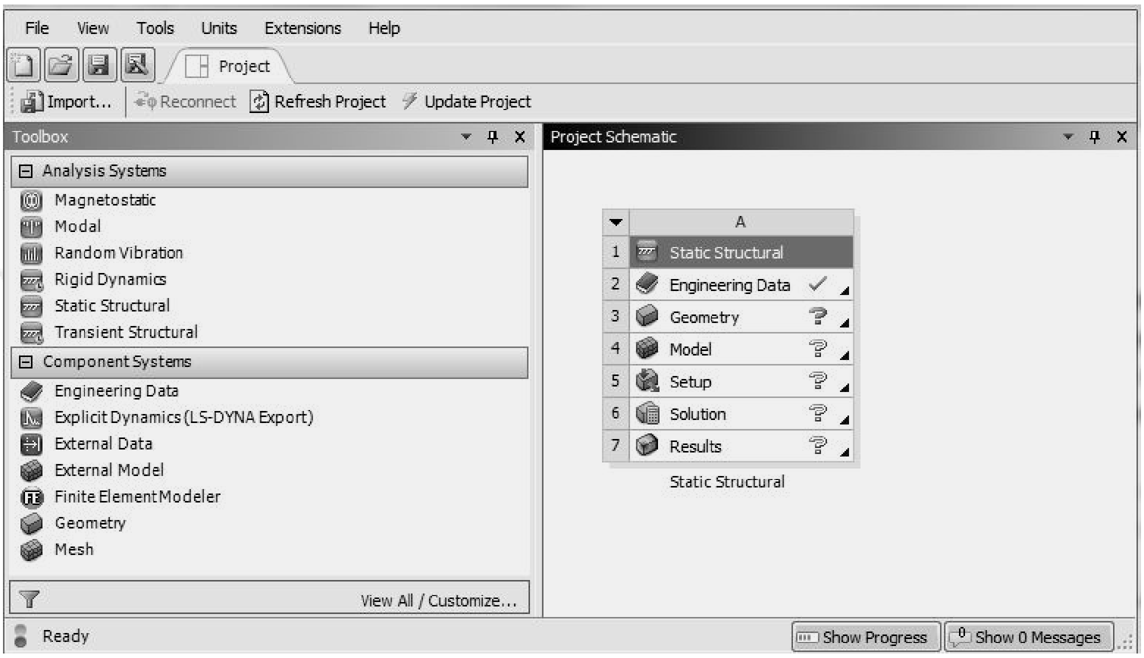

Figure 2.31. Workbench GUI
(Source: ANSYS Workbench, 2015)

Static analysis is performed in Workbench by the flowchart shown in Figure 2.32. Explicit dynamic analysis of a structure is not performed completely in Workbench due to the limitations of LS-DYNA applications available in Workbench. Flow chart of the explicit dynamic analysis is shown in Figure 2.33.

Structural dynamic analyses performed with the Workbench are

- Modal,
- Transient structural analysis,
- Harmonic response analysis,
- Explicit dynamics,
- Respond spectrum analysis,
- Random vibration analysis.

Each analysis type has own module in the Workbench.

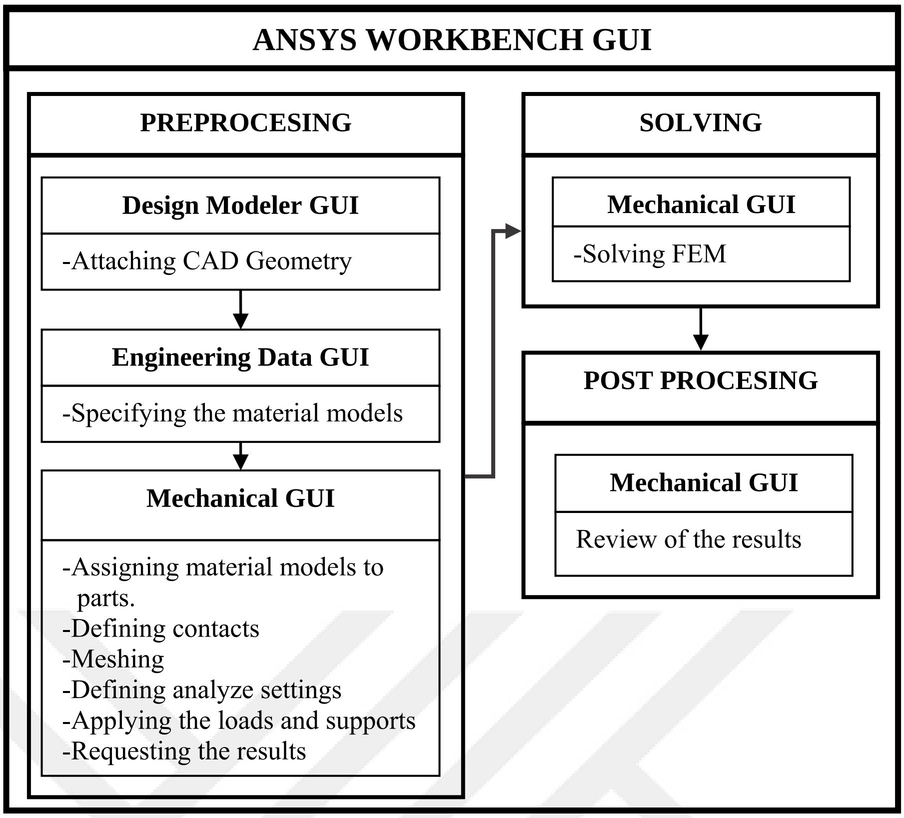

Figure 2.32. Flow chart of structural static FEA by Workbench.

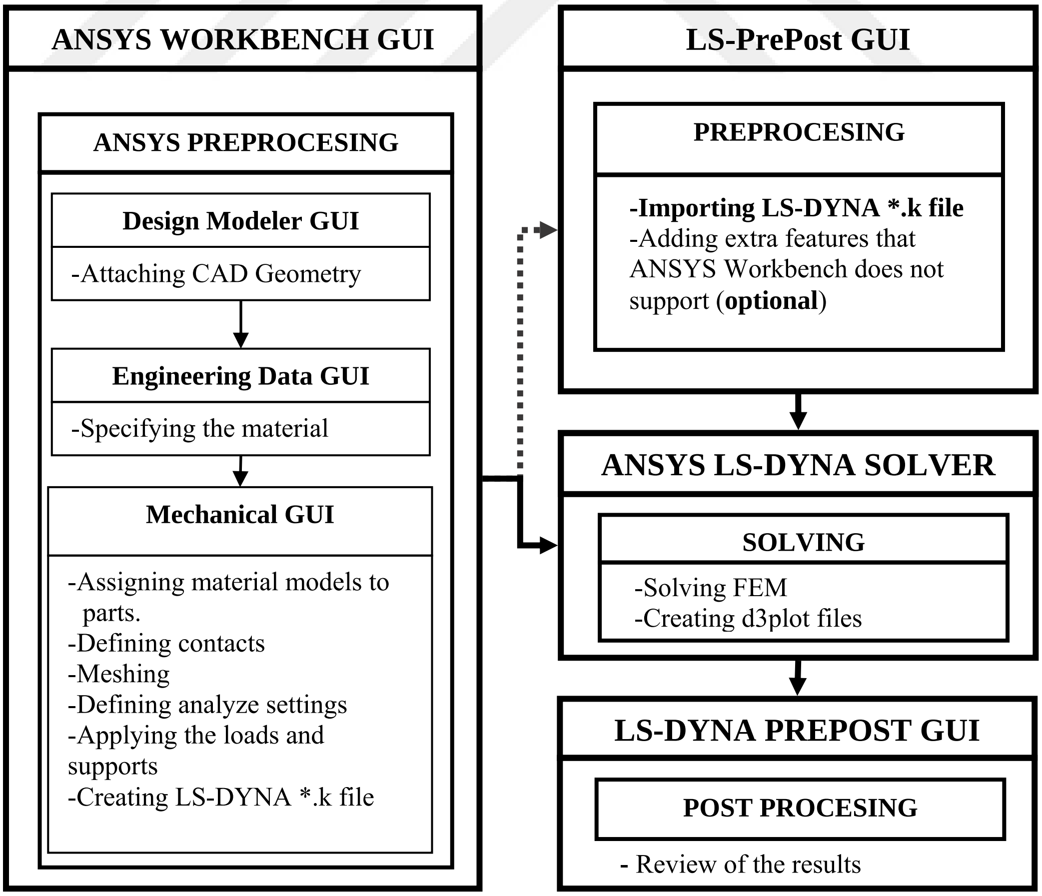

Figure 2.33 Flow chart of the explicit dynamic FEA

Material properties, rigid or flexible stiffness behavior are assigned to parts within the geometry branch of the Mechanical GUI. A rigid body, or part, is represented as a single mass element, thus it is very efficient for solution time. Mechanical application provides solid, surface and line bodies. Solid bodies are volumes or areas, surface bodies are only areas and finally line bodies are only curves. Although the thickness of surface bodies is defined in the "Details" view of the "Geometry" branch, the cross-section and orientation are defined within Design Modeler for line bodies and are imported into Mechanical automatically (Lee, 2014).

Touching two separate surfaces of bodies each other is termed contact. Contacts and contact types are defined within the contact branch of the Mechanical GUI. Contact surfaces have some flowing characteristics. Interpenetration does not occur and normal compressive and tangential friction forces are transmitted but tensile normal forces usually are not transmitted. Surfaces can separate and move away from each other. Touching or separating of the surfaces changes the contact status and the stiffness of the system. Therefore, some contact types are nonlinear. Workbench supports five contact types given below.

1. Bonded: This type of contact does not allow penetration, separation and sliding between faces or edges.
2. No Separation: This type of contact does not allow penetration or separation but frictionless sliding is allowed along contacting faces.
3. Frictionless: This type of contact does not allow penetration, but surfaces are free to slide and separate without resistance.
4. Rough: This type of contact does not allow penetration or sliding, but surfaces are free to separate without resistance.
5. Frictional: This type of contact does not allow penetration, but surfaces are free to slide with resistance proportional to user defined coefficient of friction and separate without resistance.

While the first and second contact types are linear and require only one step iteration, other contact types are nonlinear and need multiple iterations.

Numerous bodies may be grouped into multi-body parts in the Design Modeler. Multi-body parts' common boundaries are shared and the contact surfaces behave as bonded contact type. Contact definition is not needed in these situations.

In addition to contact connections, there are body to body or to ground connection branch for tying entities together using spring elements for static structural FEA in

Workbench. From the connections branch, a spring element with nonlinear properties can be inserted between two scoped entities. Spring element connection is not supported by Workbench Explicit Dynamic (LS-DYNA Export) application. Spring element connections for explicit dynamic analyses are defined within the LS-DYNA PrePost GUI.

Meshing operations are carried out within the Mesh branch of the Mechanical GUI of Workbench. Some finite elements are introduced below.

The SOLID187 element shown in Figure 2.34 is a higher order 3-D, 10-node element and each node has three degrees of freedom: translations in the nodal x, y, and z directions. The capabilities of the element are suitable for plasticity, hyperelasticity, creep, stress stiffening, large deflection, and large strain.

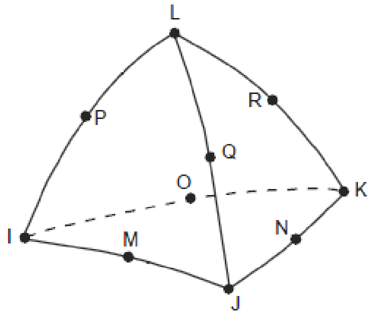

Figure 2.34. SOLID187 element
(Source: ANSYS, 2009)

The SOLID186 element shown in Figure 2.35 is a higher order 3-D 20-node solid element and each node has three degrees of freedom: translations in the nodal x, y, and z directions. The capabilities of the element are suitable for plasticity, hyperelasticity, creep, stress stiffening, large deflection, and large strain capabilities.

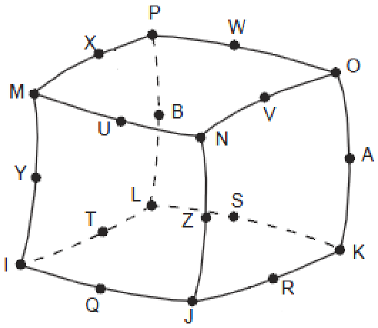

Figure 2.35. SOLID186 element
(Source: ANSYS, 2009)

The SURF154 element shown in Figure 2.36 is defined by four to eight nodes. It is used for various load and surface effect applications in 3-D structural analyses.

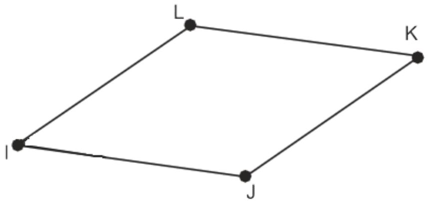

Figure 2.36. SURF154 element
(Source: ANSYS, 2009)

The SOLID164 element is an 8-node brick element shown in Figure 2.37 is used for the 3-D modeling of solid structures. It is defined by eight nodes having the following degrees of freedom at each node: translations, velocities, and accelerations in the nodal x, y, and z directions. Wedge, pyramid, and tetrahedral shaped SOLID164 elements are degenerated bricks formed by repeating some of the nodes. This element is used in explicit dynamic analyses only. The capabilities of the element are suitable for isotropic elastic, bilinear kinematic and isotropic, Mooney-Rivlin rubber material models.

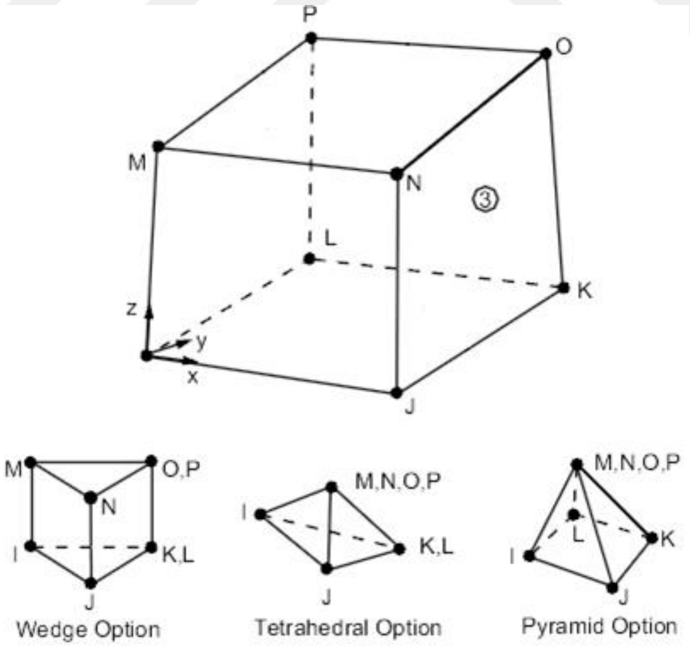

Figure 2.37 SOLID164 element with options
(Source: ANSYS, 2009)

The BEAM161 element has 3 nodes and each node has the following degrees of freedom: translations, rotations, velocities, and accelerations in the nodal x, y, and z directions. This element is used in explicit dynamic analyses only. The capabilities of the element are suitable for isotropic elastic and bilinear kinematic material models.

Analysis settings, initial conditions, loads and supports of the finite element model are specified within the Static Structural and Explicit Dynamic branch of the Mechanical GUI of Workbench. A series of static analyses called Multi-Step Analysis can be set up and solved sequentially by means of Number of Steps option of analyze settings.

Requested results such as total deformation and von-Mises stress distributions are viewed from the Solution branch of the Mechanical GUI of Workbench except explicit dynamic (LS-DYNA) analysis type, because all post-processing operations can be done by using LS-PrePost.

2.13.4. Generating LS-DYNA Keyword File in Workbench

After pre post operations for explicit dynamic (LS-DYNA) analysis is performed in Workbench, the LS-DYNA keyword file is generated in the explicit dynamic branch of Mechanical GUI of Workbench. During this process, ANSYS file format is converted to LS-DYNA keyword file format. For explicit dynamic (LS-DYNA) analysis, LS-DYNA keywords used in this thesis are given in Tables 2.1-2.3 for the material models, contact and element types defined in the Workbench. Also, LS-DYNA keywords used in this thesis and defined in LS-PrePost are listed in the Table 2.4.

Table 2.1. The Workbench materials models / LS-DYNA material keywords

Workbench material models	Corresponding LS-DYNA material keywords
Isotropic elasticity	*MAT_ELASTIC
Bilinear isotropic hardening	*MAT_MODIFIED_PIECEWISE_LINEAR_PLASTICITY
Bilinear kinematic hardening	*MAT_PLASTIC_KINEMATIC
Mooney Rivlin with two parameters	*MAT_HYPERELASTIC_RUBBER
Rigid	*MAT_RIGID

Table 2.2. The Workbench contact types / LS-DYNA contact keywords

Workbench Contact name	Corresponding LS-DYNA contact keyword
Bonded	*CONTACT_TIED_NODES_TO_SURFACE
Frictionless	*CONTACT_AUTOMATIC_NODES_TO_SURFACE
Frictional	*CONTACT_AUTOMATIC_NODES_TO_SURFACE

Table 2.3 The Workbench element types / LS-DYNA contact keywords

Workbench Element Name	corresponding LS-DYNA element *keyword
Tet4 (SOLID164-tetrahedral option)	*SECTION_SOLID, ELFORM 13
Hex8 (SOLID164)	*SECTION_SOLID, ELFORM 1
Low Order Beam (BEAM161)	*SECTION_BEAM, ELFORM 1

2.13.5. LS-Prepost

Some pre- and all post-processing operations are done by using LS-PrePost since Workbench does not support the viewing. The operations used in this thesis and given in Table 2.4 are performed by using Page Menu and Main Button menu shown in Figure 2.38.

Table 2.4. LS-DYNA keywords defined by using LS-PrePost

Purpose	LS-DYNA keyword
Defining the dynamic relaxation of the impact system before impact due to inflated tire and preloaded bolts.	*CONTROL_DYNAMIC_RELAXATION
Defining reinforcement elements of the tire.	*CONSTRAINED_LAGRANGE_IN_SOLID
Dynamic modeling of the pressured air inside the tire.	*AIRBAG_SIMPLE PRESSURE VOLUME
Nonlinear spring and dashpot model of the rubber.	*MAT_SPRING_NONLINEAR_ELASTIC *MAT_DAMPER_VISCOUS

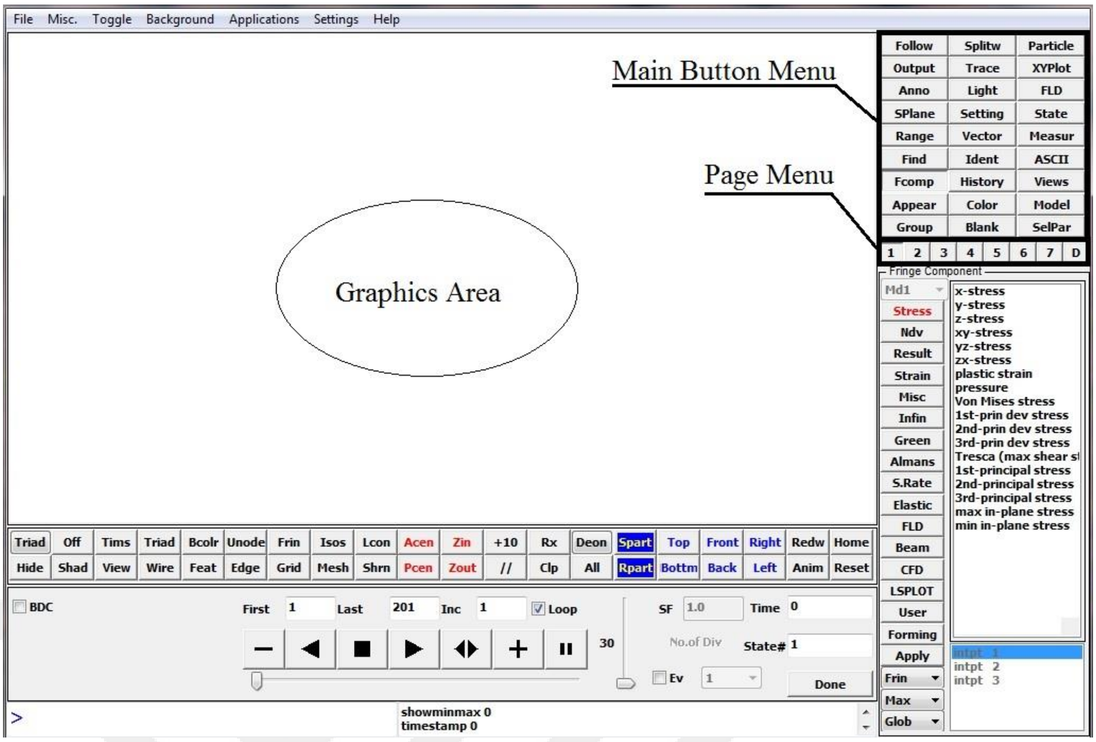

Figure 2.38. LS-PrePost GUI
(Source: LS-PrePost, 2015)

2.13.6. Numerical Methods in ANSYS Workbench and LS-DYNA

The numerical methods used in ANSYS Workbench and LS-DYNA are summarized below by illustration.

The Newton-Raphson method: This is an iterative process used to find displacement corresponding to the applied load F^a as illustrated in Figure 2.39. More details are available in finite element textbook written by Bathe (1996).

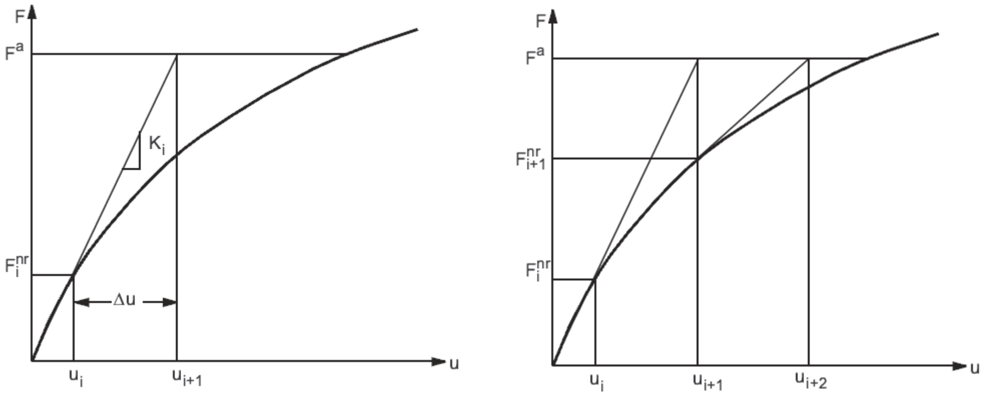

Figure 2.39 Illustration of the Newton-Raphson solution steps
(Source: ANSYS, 2009)

The notations used in Figure 2.39 are listed here for clarity:

F^a	Applied load
u_i	Displacement at iteration *i*
u_{i+1}	Displacement at iteration *i*+1
u_{i+2}	Displacement at iteration *i*+2
F_i^{nr}	Restoring force at iteration *i*
F_{i+1}^{nr}	Restoring force at iteration *i*+1
K_i	Tangent stiffness at iteration *i*

The general method is as follows:

1. Assume an initial displacement $\{u_0\}$. It is zero for the first step.
2. Calculate the updated tangent stiffness $[K_i^T]$ and restore force $\{F_i^{nr}\}$ from current displacement $\{u_i\}$.
3. Calculate $\{\Delta u_i\}$ from $[K_i^T]\{\Delta u_i\} = \{F_a\} - \{F_i^{nr}\}$ and $\{u_{i+1}\}$ from $\{u_{i+1}] = \{u_i\} + \{\Delta u_i\}$.
4. Repeat the last two steps until $\{Fa\} - \{F_n^{nr}\} < tolerance.$

In other words, the final converged solution has to be in equilibrium such that $\{F^a\} \approx \{F_n^{nr}\}$

<u>Implicit time integration method:</u> The Newmark time integration method is used. It is based on the usage of central difference method to solve equation of motion given in Equation (2.2). The equation of the method is given by Petyt (2010) as

$$\begin{aligned}
&([M] + a_1[C] + a_2[K])\{q_1\} = \\
&([M] + a_1[C] - a_3[K] - a_4[M]^{-1}[C][K])\{q_0\} \\
&+ (2a_1[M] - a_4[M]^{-1}[C]^2)\{\dot{q}_0\} \\
&+ (a_3 + a_4[M]^{-1}[C])\{F_0\} + a_2\{F_1\}
\end{aligned} \tag{2.58}$$

$$\begin{aligned}
&([M] + a_1[C] + a_2[K])\{q_{j+1}\} = \\
&a_2\{F_{j+1}\} + 2a_3\{F_j\} + a_2\{F_{j-1}\} \\
&+ (2[M] - 2a_3[K])\{q_j\} \\
&- ([M] - a_1[C] + a_2[K])\{q_{j-1}\}
\end{aligned} \tag{2.59}$$

where

$$a_1 = \Delta t / 2, \qquad a2 = \beta(\Delta t)^2 \tag{2.60}$$

$$a_3 = (0.5 - \beta)(\Delta t)^2, \qquad a4 = (0.25 - \beta)(\Delta t)^3 \tag{2.61}$$

Equation (2.58) is solved for $\{q_1\}$ then $\{q_{j+1}\}$ are used to find the next ones.

Explicit time integration method: The explicit central difference method is used in LS-DYNA to integrate the equations of motion (LSTC 2015).

$$[M]\{\ddot{q}_n\} = \{P_n\} - \{S_n\} + \{H_n\} \tag{2.62}$$

where $\{P_n\}$ includes all external and body forces, $\{S_n\}$ is the stress divergence vector, and $\{H_n\}$ is the hourglass resistance. Using the central difference time integration to advance to time t_{n+1}, the following equations are written

$$\{\ddot{q}_n\} = [M]^{-1}(\{P_n\} - \{S_n\} + \{H_n\}) \tag{2.63}$$

$$\{\dot{q}_{n+1/2}\} = \{\dot{q}_{n-1/2}\} + \{\ddot{q}_n\}\Delta t_n \tag{2.64}$$

$$\{q_{n+1}\} = \{q_n\} + \{\dot{q}_{n+1/2}\}\Delta t_{n+1/2} \tag{2.65}$$

where

$$\Delta t_{n+1/2} = (\Delta t_n + \Delta t_{n+1})/2 \tag{2.66}$$

and $\{\dot{q}\}$ and $\{q\}$ are the global nodal velocity and displacement vectors, respectively. The geometry is updated by adding the displacement increments to the initial geometry $\{x_0\}$.

$$\{q_{n+1}\} = \{x_0\} + \{q_{n+1}\} \tag{2.67}$$

2.14. Dynamic Properties of Rubbers

Rubber has elastic properties, like a metallic spring, and more energy absorbing properties like a viscous liquid. Rubber maintains its original shape after a deformation load is removed. The viscosity of rubber is based on elastomers and temperature. The Hooke's law is valid for the elasticity of rubber. The dynamic properties of elastomers are affected by temperature. The effect of temperature on the damping of compounds containing different elastomers is shown in Fig. 2.40 where the natural rubber is represented as "NR" (Harris and Piersol, 2002).

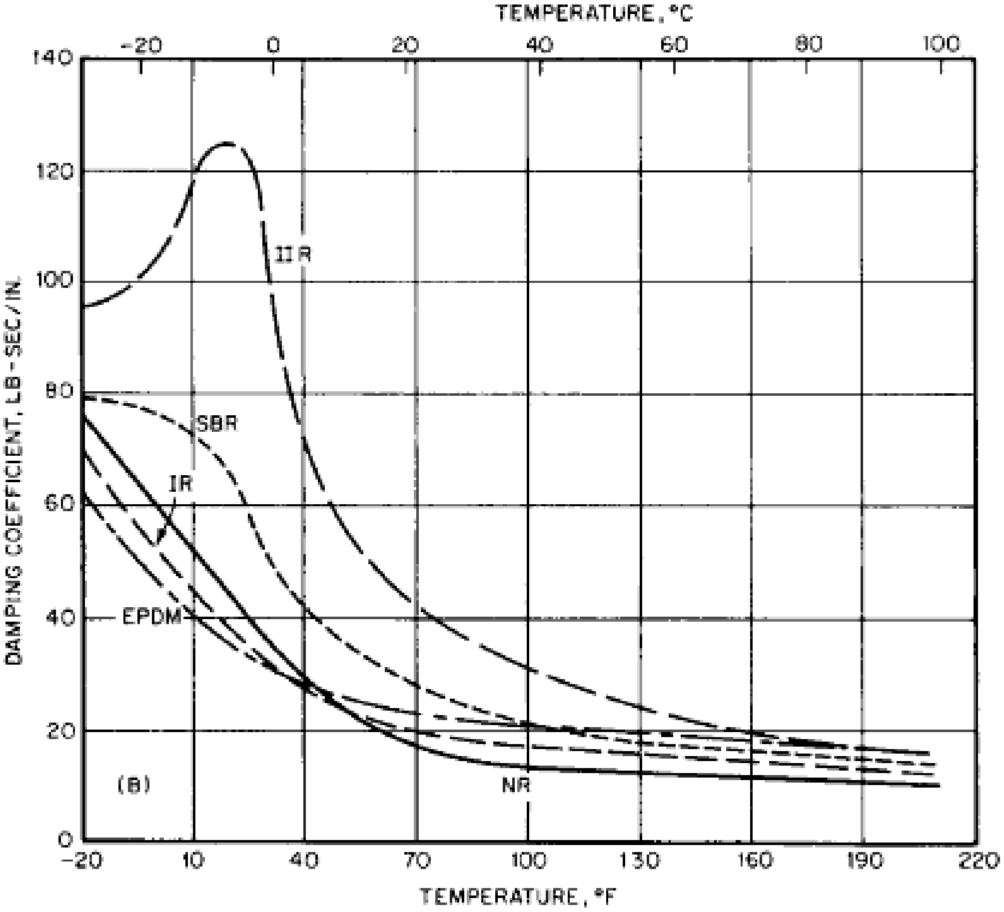

Figure. 2.40 The damping coefficient of typical isolating and damping compounds (Source: Harris and Piersol, 2002)

The elastic and viscous components of rubber are frequently illustrated by spring and dashpot to create theoretical models of rubber. The spring and dashpot is combined in parallel or series, representing the Voigt or Maxwell elements.

2.15. Introduction to Hyperelasticity

A hyperelastic material can have a large strain, up to 700%, that is recoverable. Elastomers such as rubber, many other polymers, and some biological materials are hyperelastic materials.

Polymers have flexible chain-like molecules that highly twisted, coiled, and randomly oriented in an undeformed state. The large elastic strain capability is due to the untwisting of cross-linked molecular chains. Under a tensile load, the chains become partially straightened and untwisted. The chains return to their original configuration when the load is removed. The stress-strain relationship of these materials can be highly nonlinear (ANSYS, 2010). Although polymers usually exhibit isotropic material properties at small deformation, it shows anisotropic material properties at the larger deformation. However, isotropic material properties are usually used to simplify the problem in the modeling of polymers.

Fiber reinforced polymer composites cannot be modeled as isotropic. If the stiffness of the fibers are 50-1000 times of the polymer matrix, this leads to strongly anisotropic material behavior. Biomaterials, such as muscles and arteries are another class of anisotropic materials. The anisotropic behavior of the biomaterials is due to their fibrous structure.

According to volumetric behavior of the hyperelastic materials, they are grouped into two classes: Incompressible or nearly-incompressible and compressible materials. Polymers and foam are typically first and second type of materials, respectively.

The strain energy potential (or density) function is used to obtain constitutive hyperelastic models. However, the response function model based on experimental data is an exception. Four types of hyperelastic models are available in ANSYS as follows (ANSYS, 2013).

1. Incompressible or nearly-incompressible isotropic models: Mooney-Rivlin, Neo-Hookean, Polynomial Form, Ogden Potential, Arruda-Boyce, Gent, Yeoh, and Extended Tube.
2. Compressible isotropic models: Blatz-Ko and Ogden Compressible Foam.
3. Incompressible or nearly-incompressible isotropic response function hyperelastic model.
4. Invariant-based anisotropic strain-energy potential.

As two parameter Mooney-Rivlin and Neo-Hookean models are considered in the thesis, only these two models are explained.

2.15.1. Finite Strain Elasticity

Hyperelastic material has the strain energy density function (or an elastic potential function) W that is a scalar function of one of the strain or deformation tensors. Derivation of the function with respect to a strain component determines the corresponding stress component as follows (ANSYS, 2010).

$$S_{ij} = \frac{\partial W}{\partial E_{ij}} \equiv 2\frac{\partial W}{\partial C_{ij}} \tag{2.68}$$

where S_{ij} is the components of the second Piola-Kirchhoff stress tensor, W is the strain-energy function per unit undeformed volume, E_{ij} is the components of the Lagrangian strain tensor, and C_{ij} is the components of the right Cauchy-Green deformation tensor. E_{ij} can be expressed by:

$$E_{ij} = \frac{1}{2}(C_{ij} - \delta_{ij}) \tag{2.69}$$

where δ_{ij} is kronecker delta (δ_{ij}=1, i=j; δ_{ij}=0, i≠j) and C_{ij} is the deformation tensor that is comprised of the products of the deformation gradients F_{ij}

$$C_{ij} = F_{ki}F_{kj} \tag{2.70}$$

The Kirchhoff stress is defined as

$$\tau_{ij} = F_{ik}S_{kl}F_{jl} \tag{2.71}$$

and the Cauchy stress is obtained by

$$\sigma_{ij} = \frac{1}{J}\tau_{ij} \tag{2.72}$$

The eigenvalues (principal stretch ratios) of C_{ij} are λ_1^2, λ_2^2, and λ_3^2, and exist only if:

$$\det\left[C_{ij} - \lambda_p^2\delta_{ij}\right] \equiv \lambda_p^6 - I_1\lambda_p^4 + I_2\lambda_p^2 - I_3 = 0 \tag{2.73}$$

where p=1, 2, 3 and I_1, I_2, and I_3 are invariants of C_{ij},

$$\begin{aligned} I_1 &= \lambda_1^2 + \lambda_2^2 + \lambda_3^2 \\ I_2 &= \lambda_1^2\lambda_2^2 + \lambda_2^2\lambda_3^2 + \lambda_3^2\lambda_1^2 \\ I_3 &= \lambda_1^2\lambda_2^2\lambda_3^2 = J^2 \end{aligned} \tag{2.74}$$

and

$$J = \det\left[F_{ij}\right] \tag{2.75}$$

J is also the ratio of the deformed elastic volume to the undeformed volume of materials.

2.15.2. Deviatoric-Volumetric Multiplicative Split

If it is assumed that material response is isotropic, the strain-energy function can be expressed by (Simo and Huges, 1997).

$$W = W(I_1, I_2, I_3) = W(I_1, I_2, J) \tag{2.76}$$

or

$$W = W(\lambda_1, \lambda_2, \lambda_3) \tag{2.77}$$

The modified principal stretch ratios and invariants can be written as

$$\overline{\lambda}_p = J^{-1/3}\lambda_p$$
$$\overline{I}_p = J^{-2p/3}I_p \tag{2.78}$$

Equation (2.76) and (2.77) can be rewritten as

$$W = W(\overline{I_1}, \overline{I_2}, J) = W(\overline{\lambda_1}, \overline{\lambda_2}, \overline{\lambda_3}, J) \tag{2.79}$$

2.15.3. Isotropic Hyperelasticity

Following models are for the simulation of incompressible or nearly incompressible isotropic hyperelastic materials. The two-parameter Mooney-Rivlin model can be defined as

$$W = c_{10}(\overline{I_1} - 3) + c_{01}(\overline{I_2} - 3) + \frac{1}{d}(J-1)^2 \tag{2.80}$$

where c_{10}, c_{01}, and d are material constants. The initial shear modulus μ, bulk modulus K, and Young’s Modulus E_0, can be calculated as

$$\mu = 2(c_{10} + c_{01})$$
$$K = \frac{2}{d} \tag{2.81}$$
$$E_0 = 2\mu(1+v)$$

where the v is the Poisson's ratio. The Neo-Hookean model can be defined as

$$W = \frac{\mu}{2}(\overline{I_1} - 3) + \frac{1}{d}(J-1)^2 \tag{2.82}$$

The two-term Mooney-Rivlin model is most commonly used and it can be used for up to 90-100 % tensile strains, although the model does not account for stiffening effects of the material, usually present at larger strains. The model can be also used for pure shear behavior may be characterized up to 70-90 %. Although the model can be used to characterize moderate compression behavior well up to 30 % (ANSYS, 2010).

The Neo-Hookean model is the simplest hyperelastic model and it may be used for up to 30-40 % tensile strains, characterizing of pure shear and compression behavior up to 70-90 % and 30 %, respectively.

2.16. Graphical Representation of Data, Box Plot

Assessments of the collected data can be accomplished with graphical representations. Histograms and box plots are commonly used graphs in statistics. In this thesis, box plots are used for this purpose. Therefore, the box plot and its components are defined in this section.

The box plots show how the data are spread. A typical box plot and its components are shown in Figure 2.41. The quartiles, the median, and the highest and lowest values are the interest of the box plots. A box plot shows how data are distributed within those ranges. The median is the value in the middle of a distribution. There are three quartiles which are denoted as Q_1, Q_2, and Q_3. The middle number between the smallest number and the median of the data set is the first quartile, Q_1. The median of the data is the second quartile, Q_2. The middle value between the median and the highest value of the data set is the third quartile, Q_3. Interquartile range, denoted as IQR, is the difference between Q_1 and Q_2..

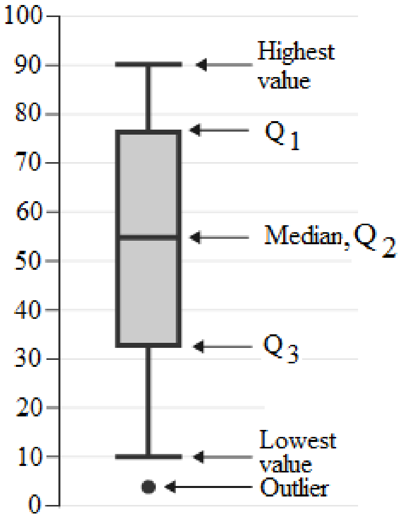

Figure 2.41 A typical box plot and its components

The presence of outliers, any observation away from the closest quartile by more than 1.5, can be easily seen by using a box plot. If an outlier is away from the closest quartile by more than 3IQR, it is considered extreme (Bass 2007).

Several box plots can be used to compare date sets with each other on the same graph.

CHAPTER 3

EXPERIMENTAL STUDIES

3.1. Introduction

Material characteristics are based on the manufacturing process. Most light alloy wheels are produced using the LPDC (low pressure die casting) method. The common materials for LPDC are AlSi11Mg and AlSi7Mg. Foundries generally have their own experience on casting which cannot be fully controlled. Although the same molds are used and the same process conditions are applied in casting, it is observed that mechanical properties of the product are not identical. Therefore, to have a general material data adequate numbers of tension, tests are also done.

In order to verify the catalog values of the rubber mounts used in the test stand, several compression tests are performed to find the force-displacements characteristics.

In total, impact tests are completed for fourteen wheel models. However, only two different wheels with different geometrical shape are chosen to present their finite element simulation details in next Chapter.

3.2. Tension Test of Aluminum Alloy Wheel Specimens

The round tension test specimens are prepared from the spokes of the $wheel_1$ and $wheel_2$ produced by the same casting charge according to DIN 50125. The material of the $wheel_1$ and $wheel_2$ tested in this step is AlSi11Mg. The specimen shown in Figure 3.1 has test piece diameter d_o=5 mm. Ten experiments conducted in the test machine are shown in Figure 3.2 for each wheel and the average material data are given in Table 3.1.

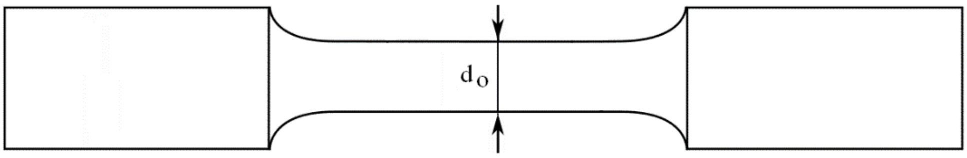

Figure 3.1. The round tension test specimen

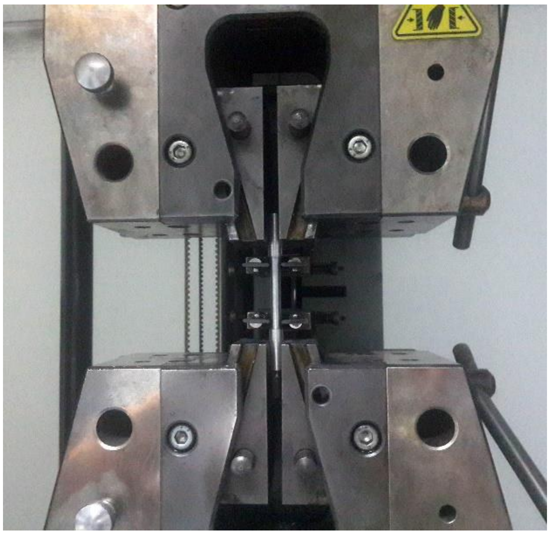

Figure 3.2. Zwick/Roell Z100 Tension test machine

Table 3.1. Material properties of the wheel$_1$ and wheel$_2$

Material Properties	Wheel$_1$	Wheel$_2$
Young's Modulus (MPa)	37540	38070
Yield Stress (MPa)	109	118
Fracture Stress (MPa)	210	210
Fracture Strain (%)	5.9	5.5

By using the experimental data given above, the bilinear isotropic hardening material model, discussed in Section 2.11.2-3, shown in Figure 3.3 is obtained to use them in numerical computations.

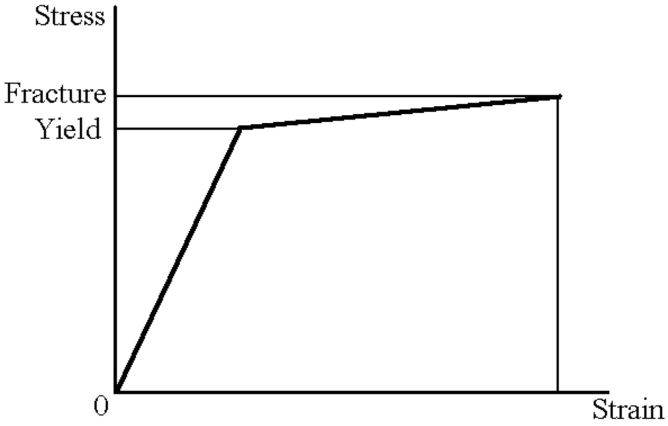

Figure 3.3. Bilinear isotropic hardening material model

It is known that the reliability of the finite element simulation results is based on tension test results. However, the mechanical properties of a wheel cannot be precisely known before casting wheel to be designed. Because of this reason, the tension tests of wheels of different shapes and sizes are performed to obtain general data about the wheel materials AlSi11Mg and AlSi7Mg.

The nine fully processed AlSi11Mg alloy wheels are chosen for the tensile tests. These wheels have different shapes and sizes to represent all possible types of AlSi11Mg alloy wheels. In total, twenty-four test specimens are obtained. Test results are given in Table 3.2. Also, statistical results are provided in Table 3.3.

The eight fully processed AlSi7Mg alloy wheels are chosen similarly. In total, thirty test specimens are obtained. Test results are given in Table 3.4. Also, statistical results are provided in Table 3.5.

Table 3.2. Tensile tests results of AlSi11Mg wheels

Sample Number	Yield Stress (MPa)	Fracture Stress (MPa)	Fracture Strain (%)	Sample Number	Yield Stress (MPa)	Fracture Stress (MPa)	Fracture Strain (%)
1	112.13	193.33	3.65	13	111.43	187.51	3.32
2	114.70	187.13	2.60	14	111.53	198.62	5.43
3	104.49	173.45	2.63	15	111.65	186.42	3.37
4	104.58	169.21	2.48	16	103.88	168.82	2.98
5	106.62	175.58	2.81	17	105.68	184.99	5.20
6	103.69	163.42	2.54	18	104.63	185.24	5.27
7	111.08	195.50	4.70	19	103.15	184.75	5.95
8	110.84	174.19	2.36	20	105.81	171.89	2.89
9	112.12	189.79	3.51	21	104.26	174.65	4,5
10	102.72	187.33	2.75	22	113.46	180.52	2.47
11	113.66	178.41	2.18	23	113.79	177.10	2.09
12	111.40	189.17	3.41	24	104.70	175.19	2.93

Table 3.3. Statistical results for tensile tests of AlSi11Mg wheels

	Yield Stress (MPa)	Fracture Stress (MPa)	Fracture Strain (%)	Young Modulus (MPa)
Average	108.90	181.34	3.42	37437
Minimum.	102.72	163.42	2.09	27087
Maximum.	114.84	198.62	5.95	46285
Standard deviation	4.1	8,9	1.11	5244

Table 3.4. Tensile tests results of AlSi7Mg wheels

Sample Number	Yield Stress (MPa)	Fracture Stress (MPa)	Fracture Strain (%)	Sample Number	Yield Stress (MPa)	Fracture Stress (MPa)	Fracture Strain (%)
1	196.89	254.33	5.89	16	195.78	238.14	2.7
2	205.79	251.4	3	17	201.18	237.54	3.2
3	199.69	251.15	3.88	18	196	236.75	2.66
4	198.33	246.85	3.25	19	194.72	236.59	3.02
5	194.71	244.57	3.59	20	193.23	236.18	3.1
6	202.28	243.91	3.1	21	187.79	235.63	3.2
7	203.63	243.63	2.8	22	181.2	235.45	3.48
8	187.18	242.97	4.04	23	193.57	234.35	2.44
9	195.15	242.67	3.1	24	196	234.22	2.35
10	193.9	242.41	3.44	25	193.31	230.32	2.3
11	183.56	242.35	4.5	26	188.36	223.79	3.15
12	204.24	241.97	2.34	27	180.68	220.83	3.11
13	200.05	239.39	3.2	28	178.59	219.53	3.3
14	192.9	238.79	3.05	29	195.78	238.14	2.7
15	191.19	238.23	3.11	30	201.18	237.54	3.2

Table 3.5. Statistical results for tensile tests of AlSi7Mg wheels

	Yield Stress (MPa)	Fracture Stress (MPa)	Fracture Strain (%)	Young Modules (MPa)
Average	194.58	239.95	3.29	59931
Minimum.	178.6	219.53	2.3	51143
Maximum.	205.8	258.39	5.89	71321
Standard deviation	7.21	9.1	0,74	5056

3.3. Compression Test of Rubber Mounts

Rubber mounts shown are on the left side of the Figure 3.4 and used in the legs of the wheel hub adapter structure as an isolator. In order to have the compression force-displacement behavior of rubber mounts, the compression test device shown in Figure 3.4 is used. It can be seen from Figures 3.5 that the rubber mount is placed in the fixture.

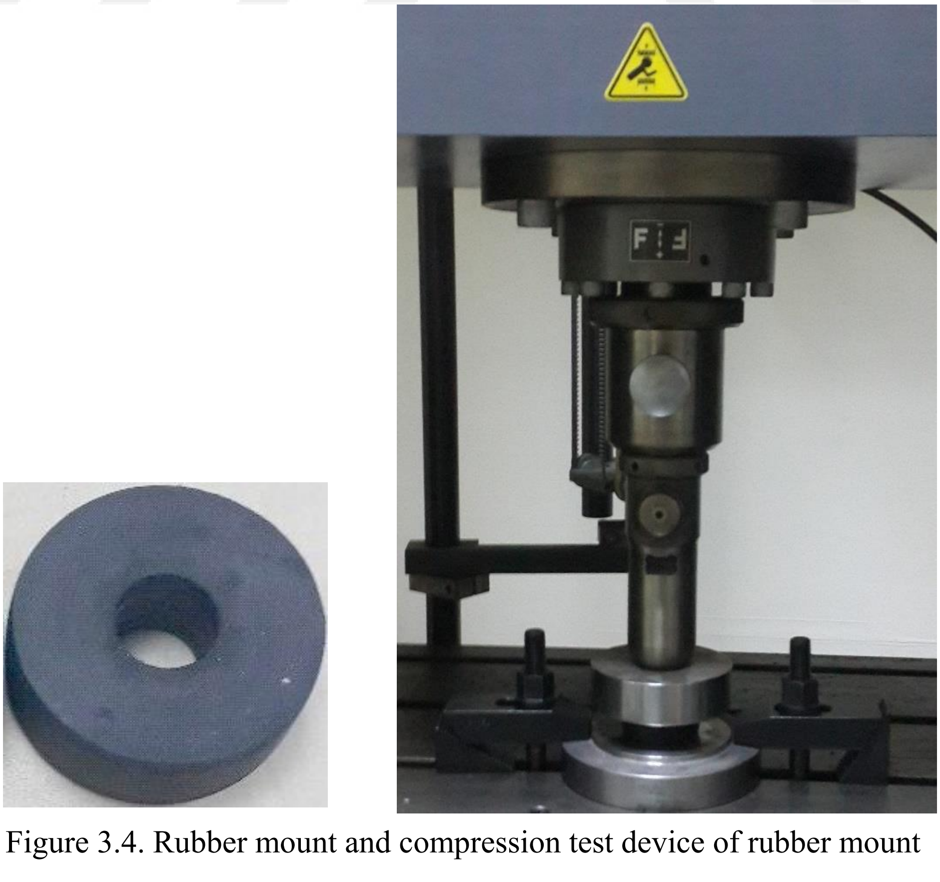

Figure 3.4. Rubber mount and compression test device of rubber mount

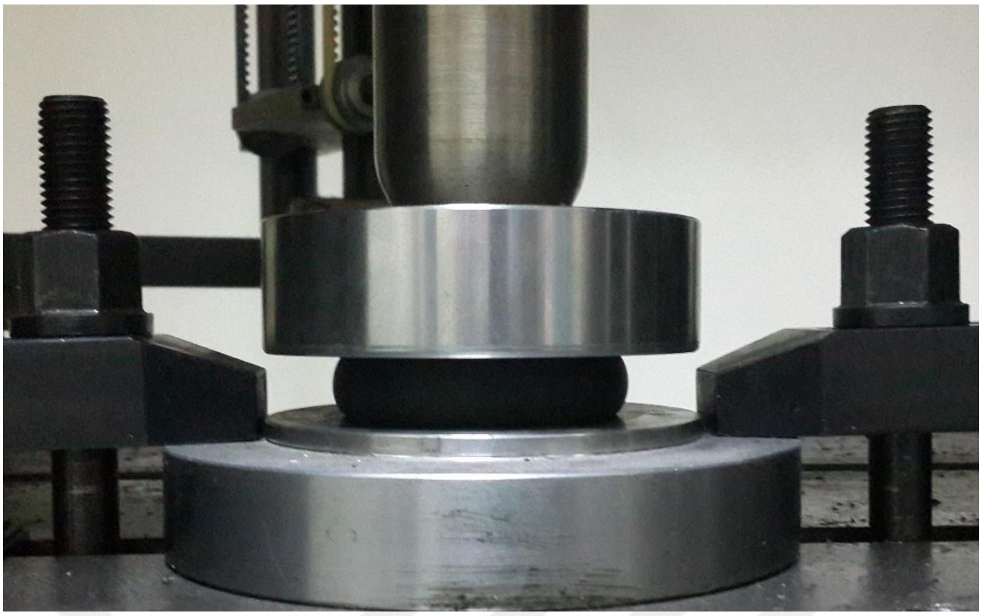

Figure 3.5. A rubber mount under compression force

The test results of five sample rubber mounts having the same dimensions with the rubber mounts used in the impact test machine are plotted in a graph shown in Figure 3.6. It should be noted that compression force is taken as positive in the plot.

From the plots mentioned above, rubber mount stiffness characteristics can be represented by bilinear form.

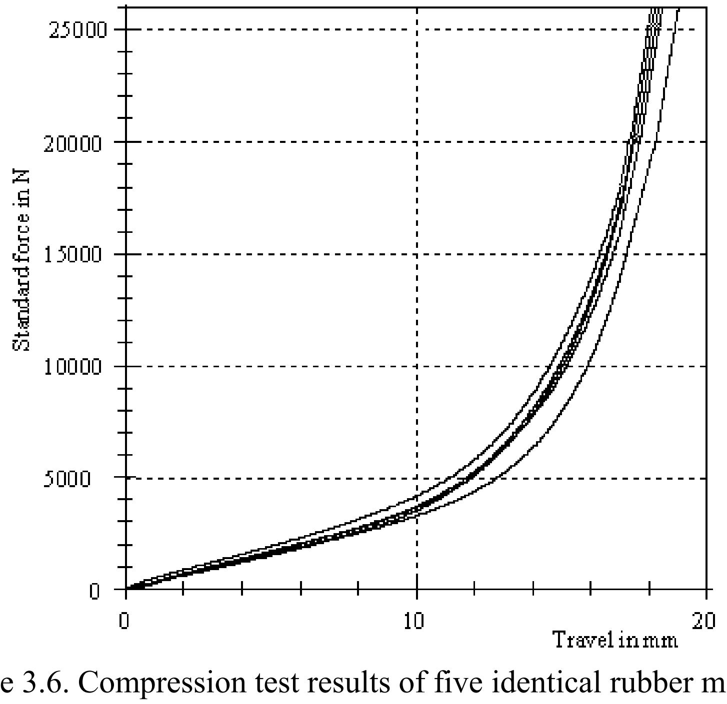

Figure 3.6. Compression test results of five identical rubber mounts

The plots in Figure 3.6 are reduced to a curve of which data is given in Table 3.6.

Table 3.6. Compression characteristics of rubber mount

Force (N)	Displacement (mm)
0	0
4000	10.76
5000	11.79
6000	12.71
7000	13.51
8000	14.08
9000	14.66
10000	15.11
11000	15.57
12000	15.92
13000	16.26
14000	16.49
15000	16.72
17000	17.23
20000	17.78
26000	18.09

3.4. Impact Tests

First, the road vehicles-light alloy wheels-impact test machine specified by ISO7141 standard and branded as MAKRA shown in Figure 3.7 is examined for calibration. The deflection at the center of the beam under the calibration load 1000 kg is found in the range of 7.5 mm ± 0.75 mm which is given by the standard.

According to ISO7141, the wheel is considered to have failed the test if any of the case given Section 2.2 occurs.

Figure 3.7. MAKRA Impact test machine

The two models, $wheel_1$ and $wheel_2$, are chosen for impact tests. The selected wheel model geometries are given in Figures 4.1. and 4.3, respectively. The nine and six samples are taken for $wheel_1$ and $wheel_2$, respectively. Although the impact load is determined by ISO7141, which is related with the maximum static wheel load provided by the vehicle producer, different loads are applied in this study to see their effects.

Plastic deformations due to impact load at the impact region of sample wheels are measured by using the CMM (coordinate measuring machine) shown in Figure 3.8. As an example of plastic deformation at the impact region is shown in Figure 3.9.

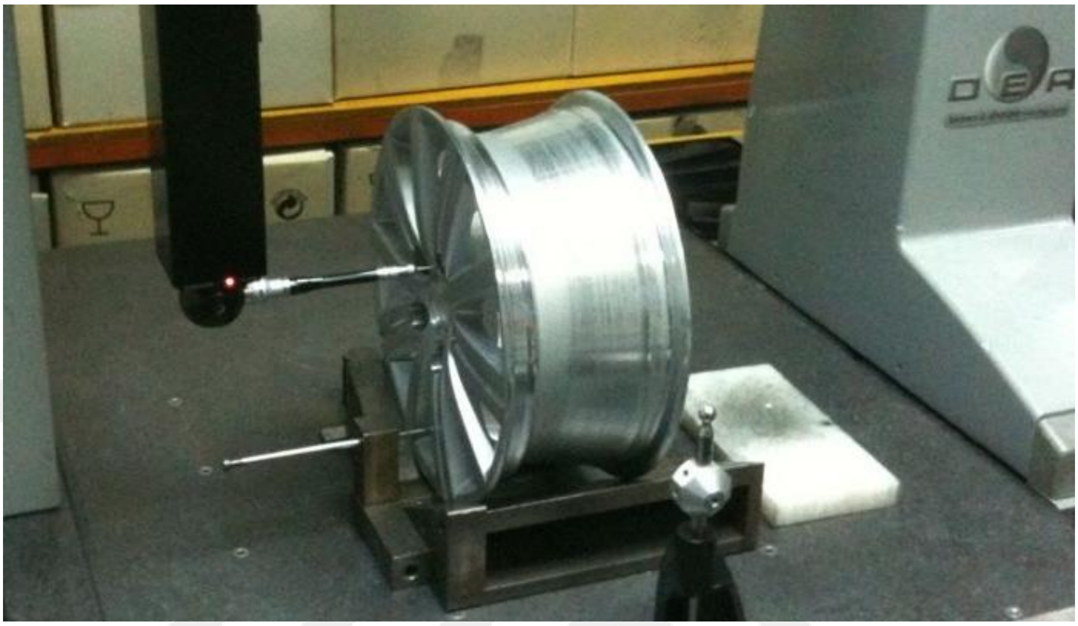

Figure 3.8. Measuring the plastic deformation by CMM

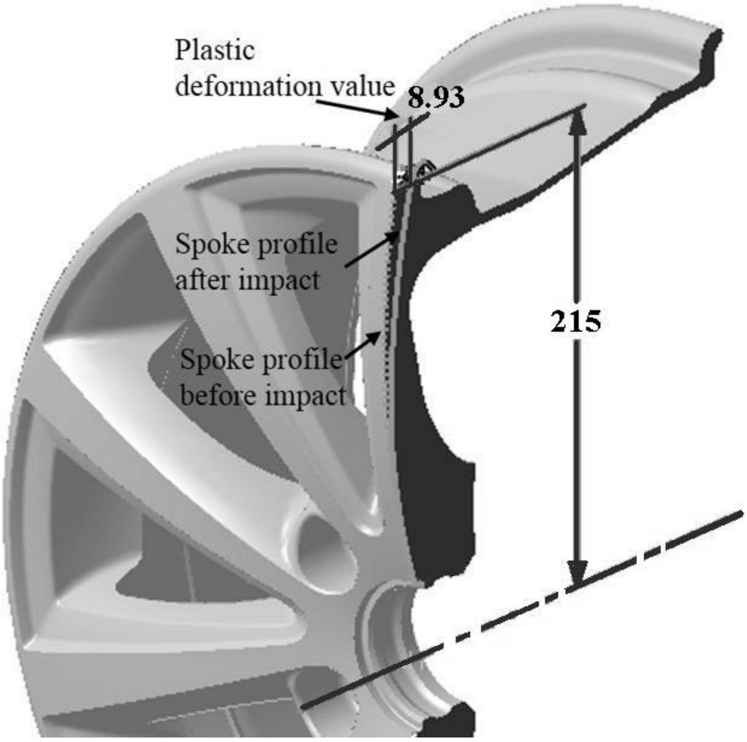

Figure 3.9. Plastic deformation value of the spoke

The measured plastic deformations for nine samples of wheel$_1$ and six samples of wheel$_2$ under different impact loads are given in Table 3.7 and 3.8, respectively.

Table 3.7. Impact test results for wheel$_1$

Sample number	Impact Load (kg)	Plastic deformation (mm)
1.1	450	6.153
1.2	450	6.557
1.3	450	7.100
1.4	550	8.928
1.5	550	8.870
1.6	550	7.412
1.7	800	17.364
1.8	800	16.515
1.9	800	16.348

Table 3.8. Impact test results for wheel$_2$

Sample number	Impact Load (kg)	Plastic deformation (mm)
2.1	400	6.842
2.2	400	6.891
2.3	400	5.540
2.4	540	9.866
2.5	540	12.258
2.6	540	10.880

In order to determine the failure characteristics of the wheels based on the criteria given before as “Visible fracture(s) penetrate through a section of the center member of the wheel assembly”, totally 31 impact tests under different impact loads are accomplished for four different AlSi11Mg alloy wheel models and ten different AlSi7Mg alloy wheel models. The wheels have different sizes and shapes.

Increasing the impact load from design load to failure level, numerous conditions are considered. The results are given in Table 3.9.

Table 3.9. Experimental results based on visible fracture

Model number	Alloy type	Impact load (kg)	Experimental result
1	AlSi11Mg	450	No fracture
1	AlSi11Mg	550	No fracture
1	AlSi11Mg	800	No fracture
2	AlSi11Mg	400	No fracture
2	AlSi11Mg	540	No fracture
2	AlSi11Mg	900	No fracture
3	AlSi11Mg	468	No fracture
4	AlSi11Mg	396	No fracture
5	AlSi7Mg	825	Fracture
5	AlSi7Mg	775	No fracture
5	AlSi7Mg	725	No fracture
5	AlSi7Mg	675	No fracture
5	AlSi7Mg	627	No fracture
6	AlSi7Mg	775	Fracture
6	AlSi7Mg	725	No fracture
6	AlSi7Mg	625	No fracture
6	AlSi7Mg	575	No fracture
6	AlSi7Mg	525	No fracture
7	AlSi7Mg	800	No fracture
7	AlSi7Mg	750	No fracture
7	AlSi7Mg	700	No fracture
7	AlSi7Mg	650	No fracture
8	AlSi7Mg	468	No fracture
8	AlSi7Mg	468	Fracture
9	AlSi7Mg	558	No fracture
9	AlSi7Mg	558	Fracture
10	AlSi7Mg	573	No fracture
11	AlSi7Mg	850	Fracture
12	AlSi7Mg	615	No fracture
13	AlSi7Mg	585	No fracture
14	AlSi7Mg	498	Fracture

Examples of failed wheels from the impact tests are shown in Figure 3.10.

Figure 3.10. Some of the wheels failed in the impact tests

CHAPTER 4

MODELLING OF THE IMPACT TEST

4.1. FE Modeling of the Wheels

The 3D solid models of the wheels studied on this thesis were modeled by CATIA. The first model is shown in Figure 4.1. Then, the 3D model is transferred to ANSYS for finite element analysis. It is meshed by tetrahedral solid elements as shown in Figure 4.2.

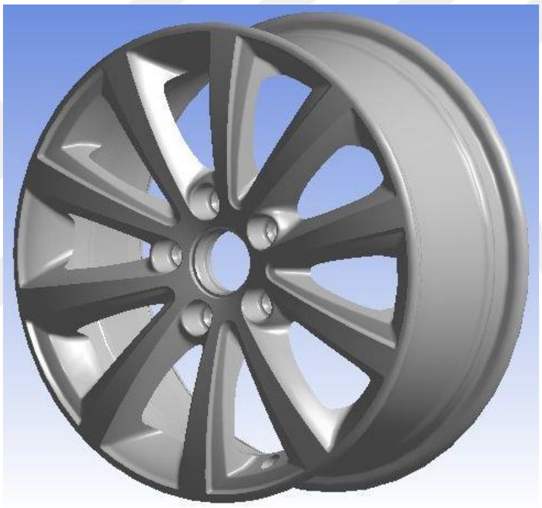

Figure 4.1. 3D solid model of $wheel_1$ with 6.5Jx16H2

Figure 4.2. Finite element model of the $wheel_1$

The second model is shown in Figure 4.3. Similar to the first model, the 3D model is transferred to ANSYS for FE (finite element) analysis. It is also meshed by tetrahedral solid elements as shown in Figure 4.4.

Wheel material is AlSi11Mg and is considered isotropic, homogeneous and strain rate independent (as discussed Chapter 1 and Section 2.11.4) Density and Poisson's ratio are 2.77x10^3 kg/m^3 and 0.33, respectively.

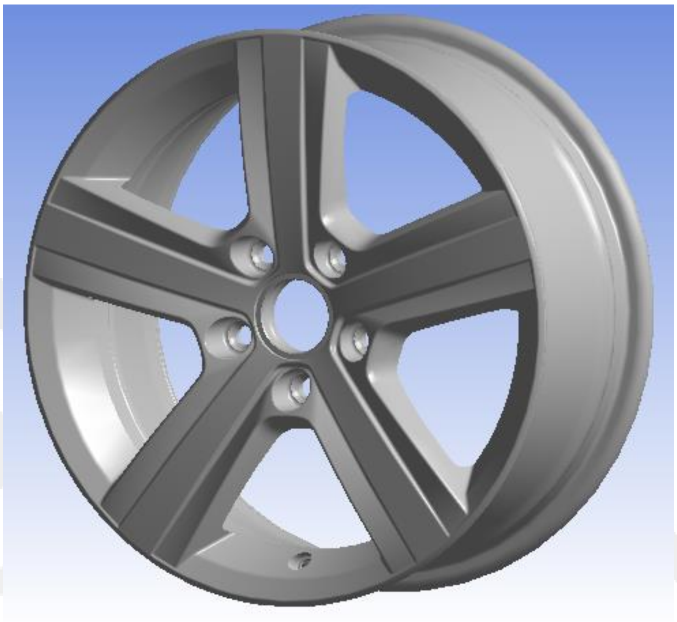

Figure 4.3. 3D solid model of wheel$_2$ with 6.5Jx16H2

Figure 4.4. Finite element model of the wheel$_2$

The selected tetrahedral element has 4 nodes. According to the convergence studies done for the size of mesh, 5 mm is selected for general mesh size. Additionally, due to the complex shape of the wheel, for the critical regions, such as rim part and other smaller regions, mesh size is taken as 4 mm and 2.5 mm, respectively.

4.2. FE Modeling of the Pneumatic Tire

4.2.1. 3D FE Model of the Pneumatic Tire

There are many types of tires depending on the application area. Radial tubeless tires named P205/55 R16 for passenger cars are used in this study.

The dimensional parameters such as thickness, position of the beads, carcass and cord elements of the selected tire are found by cutting the tire as shown in Figure 4.5.

Figure 4.5. Half cross-section of the tire

It is known that dimensions of the tire profiles are available in the ETRTO (2011). Bead core, crown and casing plies of the tire are reinforcement components. Each bead core has 20 steel wires having totally 19.625 mm^2 cross sectional area which corresponds to approximately a wire with diameter of 5 mm.

In thread region, defined in Figure 2.8, of the present cross-section, there are double crown plies (belts) that have steel wires of diameter 1 mm.

A single casing ply is shown in Figure 4.6 and its diameter is 1 mm.

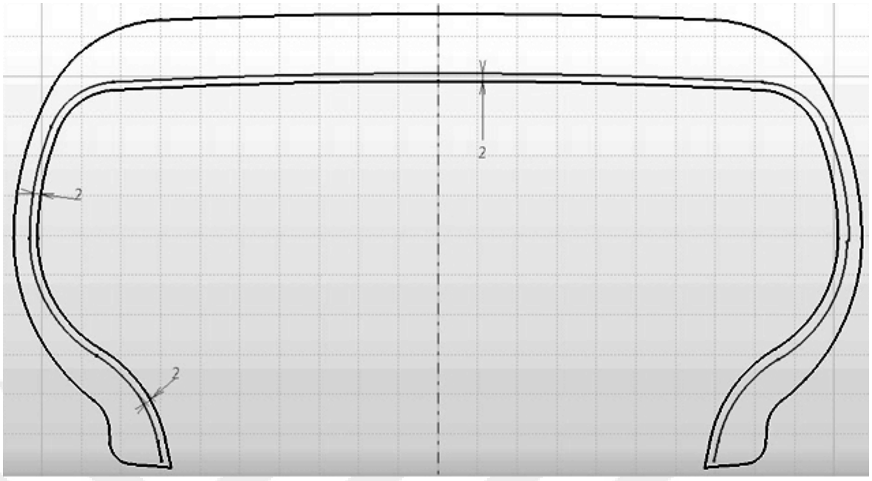

Figure 4.6. Casing ply of the tire

Tire materials are considered as isotropic, homogeneous, and strain rate independent. The material properties used in the finite element model is given in Table 4.1.

Additionally, tread is modeled by the two parameter Mooney-Rivlin model of which parameters are as follows: C_{10}= 1 MPa, C_{01}=0, and D_1=5x10^{-14} MPa (Neves et al, 2010). Also, bilinear kinematic hardening model is used for bead core wire and belt wire.

Table 4.1. The material properties and material models of the tire
(Sources: Reid et al., 2016 Neves et al., 2010)

Part Name	Bead wall and Side walls	Tread	Bead wire and belt	Casing ply
Material	Rubber	Rubber	Steel	Synthetic
Density (kg/m^3)	1.1x10^3	0.94x10^{3*}	7.85x10^{3*}	1.39x10^3
Poisson's ratio	0.45	0.4995	0.3	0.28
Young's modulus (MPa)	30	E_0=6*	200000	5000
Yield stress (MPa)	-	-	350	-
Tangent modulus (MPa)	-	-	700	-

* Calculated by using Equation 2.81.

Various types of finite elements are used for finite element modeling of the tire. Rubber parts are modeled by 8 noded hexahedron finite elements. Mesh size of the side walls and tread are 5 mm while bead parts are 3 mm.

Beat wires, belts and casing plies are modeled by reinforcement elements. Average mesh size of these elements are taken 15 mm. Finite element model of the whole tire is given in Figure 4.7.

Lagrange in solid option in LS-DYNA is used for constraining of the reinforcement elements inside the tire. This option allows all reinforcement elements to move with rubber elements of the tire during inflation and impact. Airbag simple pressure volume option in LS-DYNA is used to simulate air pressure in the tires for both inflation and impact phase of the test for more realistic simulation. If only a pressure load is defined for control volume for the tire, the pressure does not change during the impact. Airbag simple pressure volume option considers that when the volume changes, the pressure will also change.

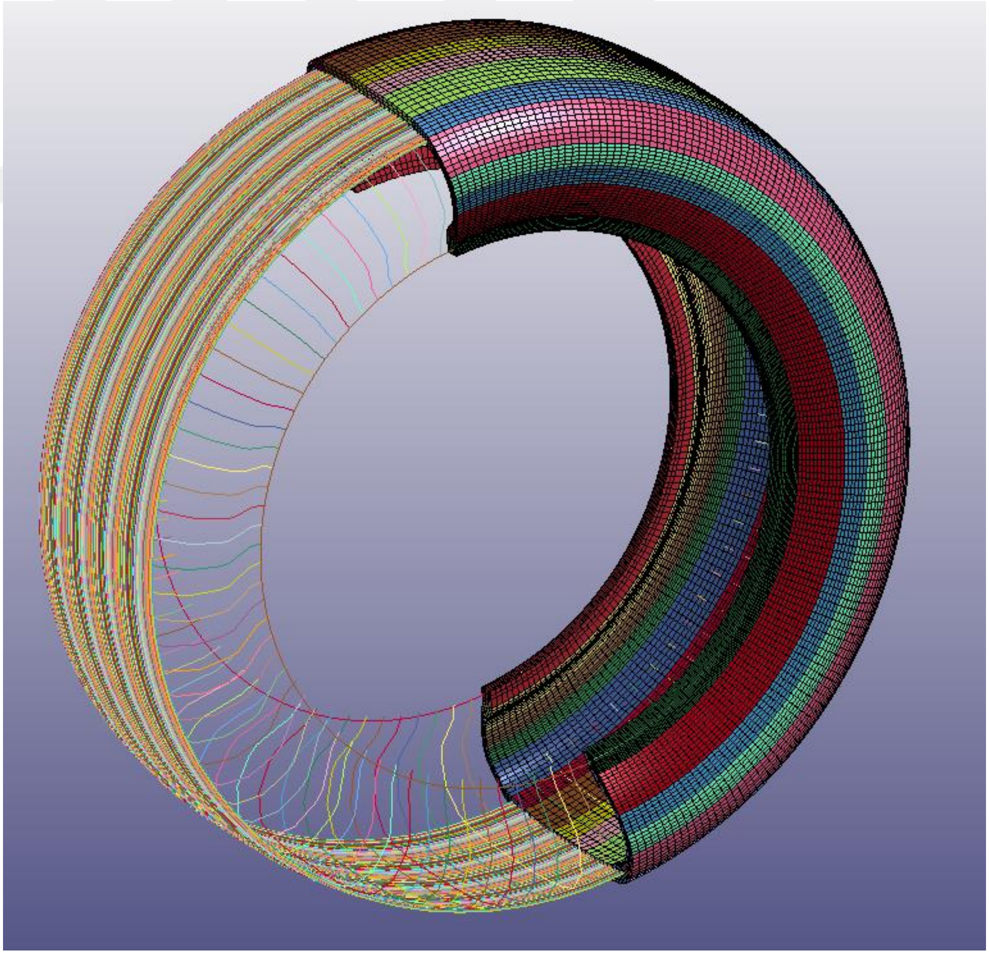

Figure 4.7. Finite element model of the tire

4.2.2. Simplified Model of the Pneumatic Tire

Pneumatic tire components are presented in Section 2.4 by showing cross-ply tire and radial-ply tire construction in Figures 2.5 and 2.6, respectively. The technical terminology of the components of the tire is illustrated in Figure 2.8 in detail. Figure 2.8 can be reduced to a cross-section model as shown in Figure 4.8.

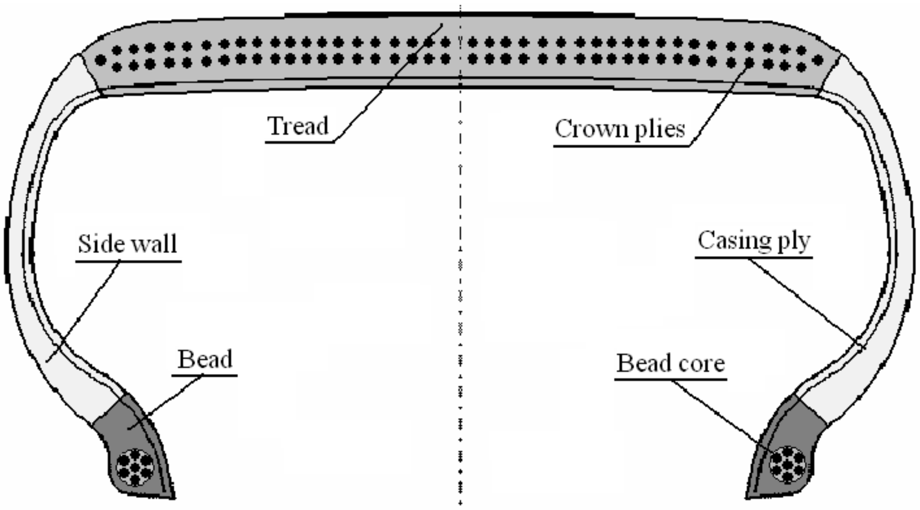

Figure 4.8. Section of the rubber part of the tire

If Figures 2.8 and 4.8 are examined carefully by considering the finite element modeling approaches, a simple model shown in Figure 4.8 can be obtained.

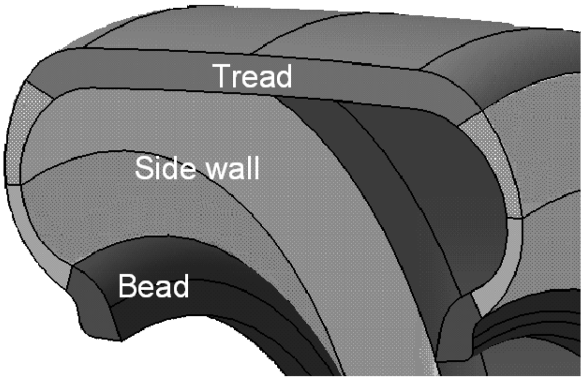

Figure 4.9. Simplified cross-section of the tire

Let us imagine a pneumatic tire having an internal pressure. Due to the internal pressure, it is clear that the tire has major stresses in different part in different directions. While tread and bead parts have major stresses in circumferential directions, the side wall is under major stresses in radial directions. Because of these realities, crown plies, casing plies and bead core mainly have tension.

Now, let us consider a rubber with continuous longitudinal fiber in the shape of a tension test specimen. The cross-section of this composite test specimen has two different materials: rubber and fiber. Also, total cross-sectional area A_{rf} is simply

$$A_{rf} = A_r + A_f \tag{4.1}$$

where A_r and A_f are cross-section of the rubber and fiber parts of the specimen, respectively. Using the equivalent axial stiffness approach for the specimen having length L, the following equation can be written

$$\frac{E_{rf} A_{rf}}{L} = \frac{E_r A_r}{L} + \frac{E_f A_f}{L} \tag{4.2}$$

where E_{rf}, E_r and E_f are equivalent modulus of elasticity of specimen, rubber and fiber parts of the specimen, respectively. Geometrical representation of the Equation (4.2) is shown in Figure 4.10 as parallel connection of two springs.

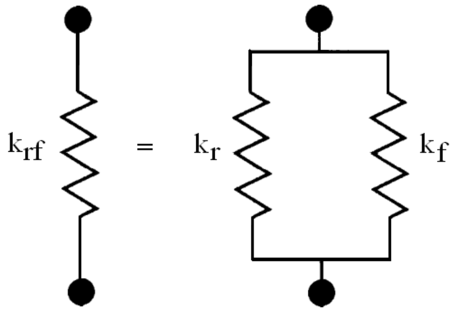

Figure 4.10. Equivalent stiffness for parallel connection of springs

From Equation (4.2), equivalent modulus of elasticity of specimen E_{rf} can be written as

$$E_{rf} = \frac{E_r A_r + E_f A_f}{A_{rf}} \tag{4.3}$$

Modulus of elasticity of the material of the tire components are provided in Table 4.1. Equivalent modulus of elasticity for tread, side wall and bead parts can be obtained by using the Equation (4.2). The term “fiber” used in Equation (4.2) corresponds to crown ply, casing ply and bead wire.

Thus, equivalent modulus of elasticity for tread and bead are calculated as

$$E_{tread} = \frac{E_r A_r + E_f A_f}{A_{rf}} = \frac{6*2652.6 + 200000*201}{2853.6} = 14093 \text{ MPa}$$

$$E_{bead} = \frac{E_r A_r + E_f A_f}{A_{rf}} = \frac{30*353.785 + 200000*19.625}{373.41} = 10540 \text{ MPa}$$

In the numerical calculations given above, the areas A_r and A_f can be seen from Figure 4.8. However, for the side wall, the area normal to casing ply is considered. It is a cylindrical strip having an average radius at side wall as shown in Figure 4.11. Thus,

$$E_{side\ wall} = \frac{E_r A_r + E_f A_f}{A_{rf}} = \frac{30*9701 + 5000*70.68}{9772.2} = 66 \text{ MPa}$$

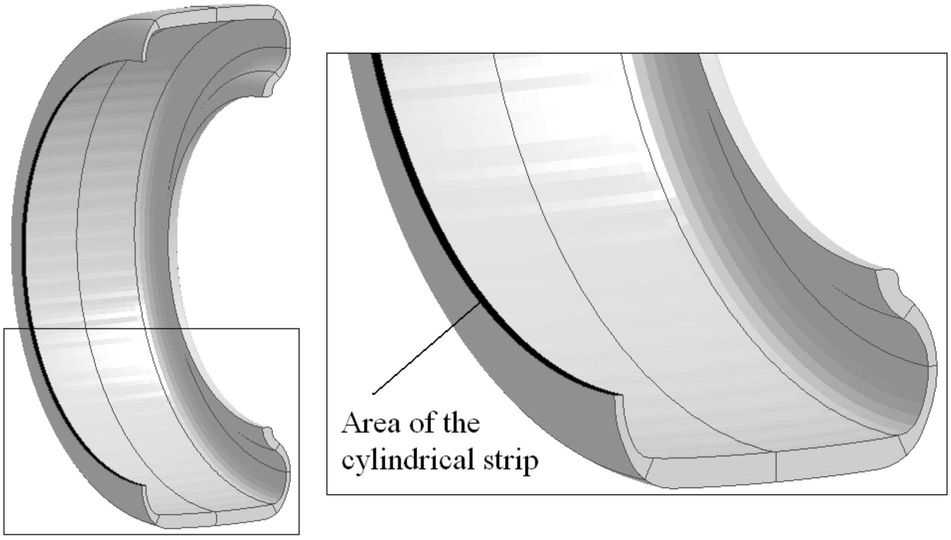

Figure 4.11 Area of the cylindrical strip of the side wall

Following the same procedure used for equivalent modulus of elasticity, equivalent densities for tread, side-wall and bead are found as 998.02 kg/ m^3, 1101.6 kg/ m^3, 1492.9 kg/ m^3, respectively.

4.3. Modeling of the Wheel and the Pneumatic Tire

4.3.1. 3D FE Model of the Wheel and the Pneumatic Tire

In this section, a 3D FE model of the wheel given in Figure 4.2 and/or Figure 4.4 is combined with FE model of tire given in Figure 4.7 by taking into account frictional contacts. Contact surfaces between bead parts of the tire and the wheel are defined as frictional contacts, as it is in the real system. Friction coefficient is 0.8, dynamic friction coefficient is 0.3. (Dirac Delta 2016) The benefit of this contact definition is to determine the contact condition. Thus, one of the failure criteria given in ISO7141 can be checked by using the contact condition. If the contact between the tire and the wheel is lost by impact load, air pressure of the tire drops. Using these details, the mentioned criteria can be evaluated.

Air pressure inside of the tire, which is taken as 200 kPa, is modeled by airbag option available in LS-DYNA.

4.3.2. 3D FE Model of the Wheel and the Simplified Pneumatic Tire

In order to reduce the degrees of freedom of the whole system obtained in Section 4.3.1, especially in LS-DYNA, the simplified tire model based on equivalent system approach given in Section 4.2.2 can be used. It is shown in Figure 4.12.

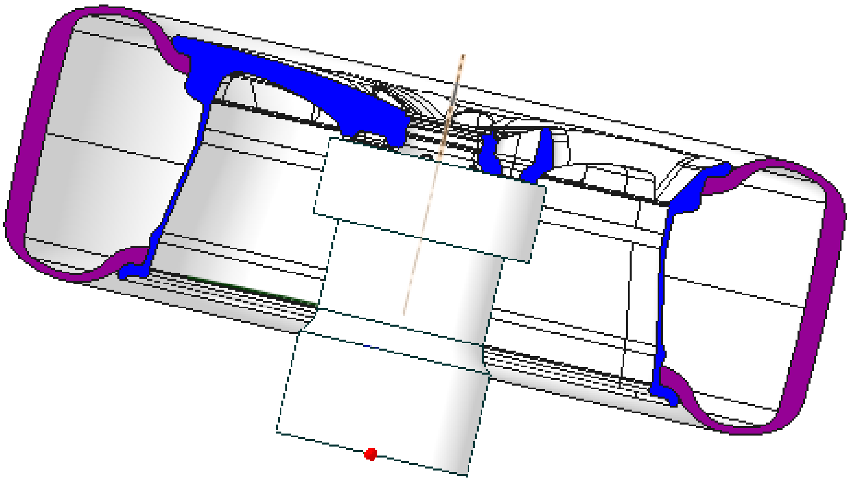

Figure 4.12. Cross-section of a wheel$_2$ with simplified tire mounted to the hub adapter

4.4. Modeling of the Impact Loading Test Machine

4.4.1. 3D FE Model of the Impact Loading Test Machine

The dimensions of the wheel hub adapter structure shown in Figure 2.2 are considered. To obtain 3D geometrical model of the structure, the undefined dimensions of the structure are taken from the real machine shown in Figure 3.7.

3D solid model of the wheel hub adapter structure and striker are modeled in CAD software as shown in Figure 4.13.

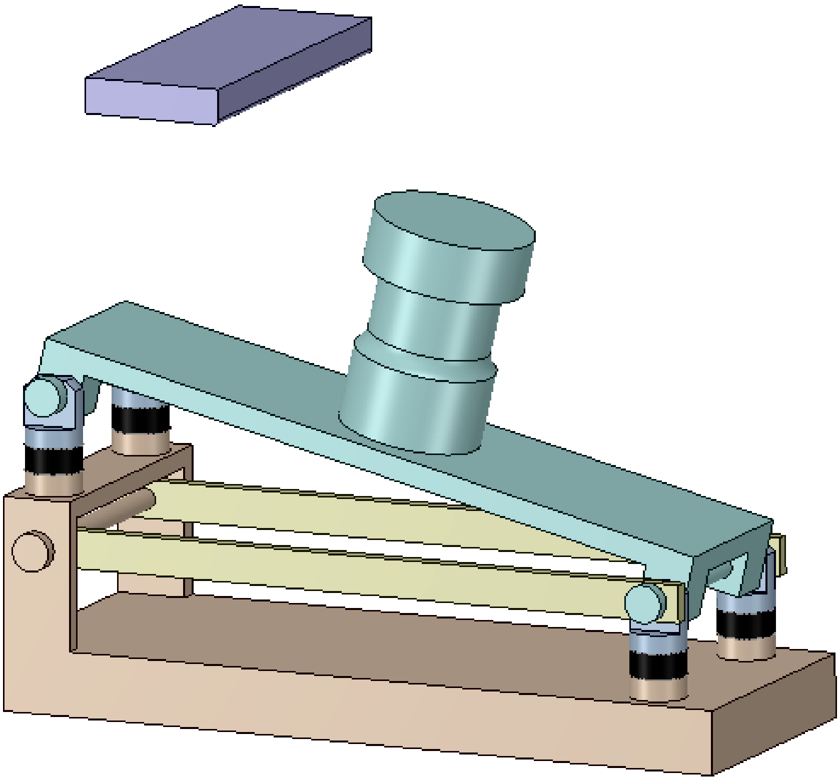

Figure 4.13. 3D solid model of the impact loading test machine

The material of the structure is steel with density 7.85x103 kg/m^3, modulus of elasticity 200 GPa and Poisson's ratio 0.3. As stated before, dampers are natural rubber.

The steel part of the solid model is meshed by 8-node hexahedron finite elements. The element size for plate and horizontal connection beam is set to be 5 mm. The rubber part of the solid model is modeled by spring and damper in finite element. Linear damping coefficient is found as 3 Ns/mm from Figure 2.40. The finite element model shown in Figure 4.14 is verified by applying the calibration load 1000 kg.

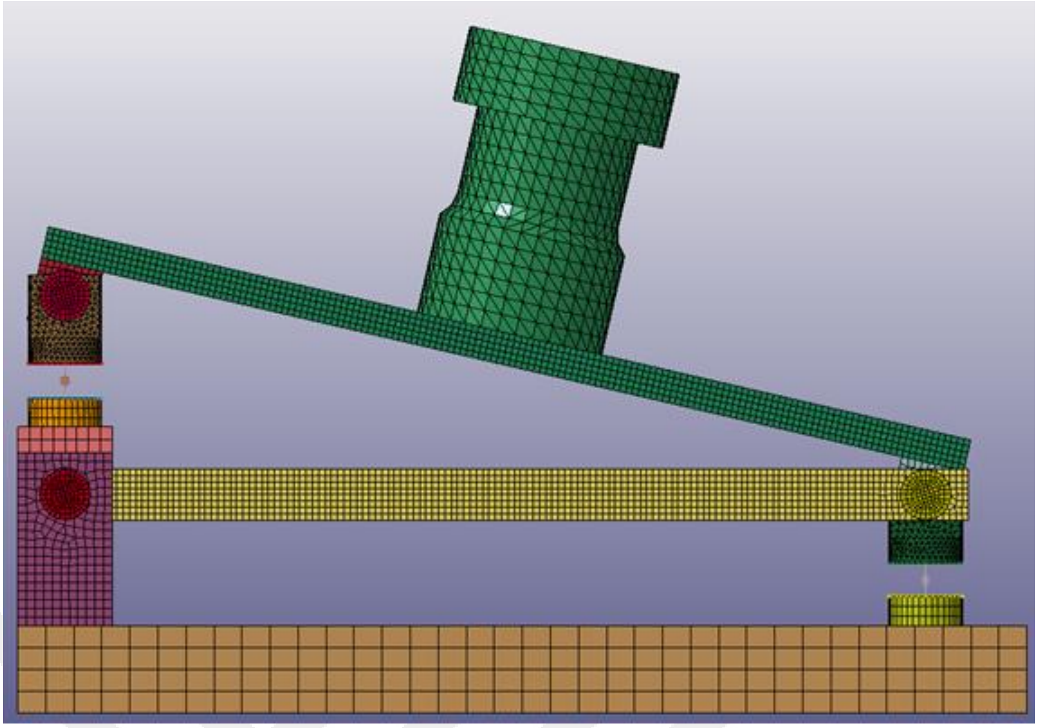

Figure 4.14. 3D FE model of the wheel hub adapter structure

4.4.2. 2D FE Model of Impact Loading Test Machine

It is very well known that the degrees of freedom of the FE model of a system is very effective on the modeling efforts and solution time especially for time dependent and/or iterative solution methods. Therefore, finite element modeling of a geometrical model is a crucial step.

Based on the experience obtained from the former studies, the wheel hub adapter structure is modeled by 1D/2D finite elements as shown in Figure 4.15. Boundary conditions are applied as in Figure 2.2, namely, long legs are fixed at the ground, but short legs have freedom in lengthwise direction. The arrow at the top of the picture represents the calibration testing load 1000 kg. The elements used in ANSYS are listed below with the modeled part of the structure.

Plate having hub adapter	: SHELL63
All beams	: BEAM4
Rubber mounts	: COMBIN39
Revolute joints	: COMBIN7
Rigid connections	: MPC184

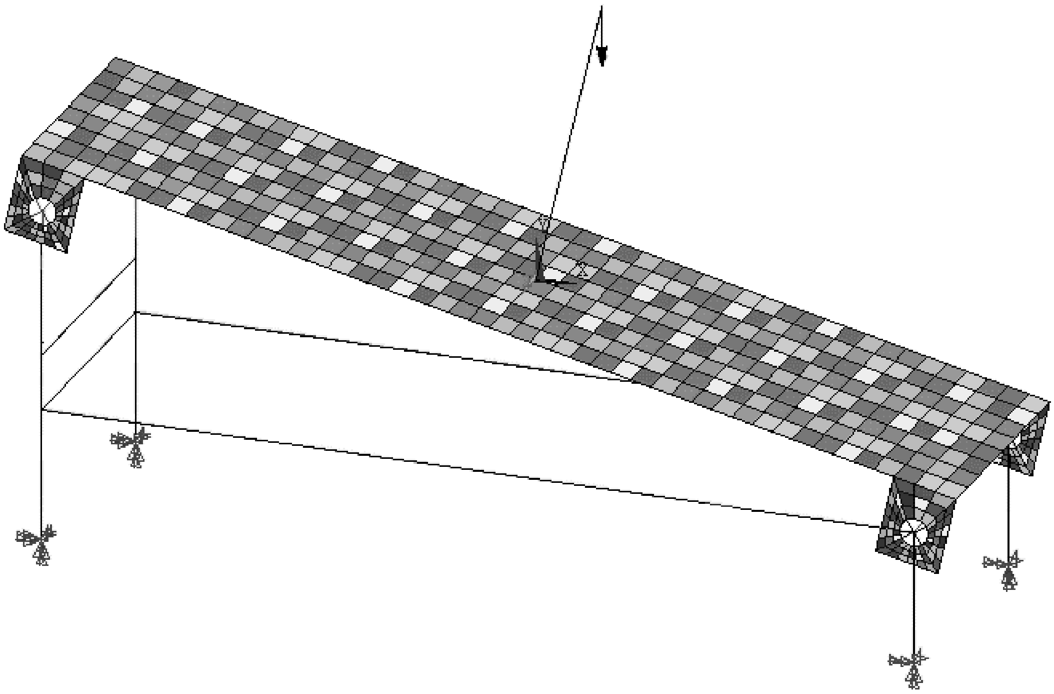

Figure 4.15. 1D/2D FE model of the wheel hub adapter structure

4.4.3. Lumped Model of the Impact Loading Test Machine

Figures 4.13-4.15 show the geometrical and finite element models of the wheel hub adapter structure. The lumped model of the wheel hub adapter structures shown in Figure 4.13 can be obtained easily. In order to find the static stiffness coefficient of the structure, a vertical force is applied to the hub adapter as shown in Figure 4.15. On the other hand, the lumped mass is simply summation of the mass of the hub adapter and the lumped mass of the beam connected to hub adapter. Thus, a lumped model can be obtained as shown in Figure 4.16.

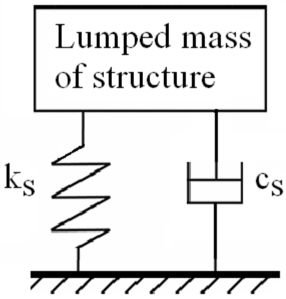

Figure 4.16. Lumped model of the wheel hub adapter structure

4.5. Modeling of the Test Systems

4.5.1. 3D FE Model of the Test Systems

In this section, the wheel with tire model is combined with the wheel hub adapter structure. The geometric model is shown in Figure 4.17. Complete FE Model of impact test system is shown in Figure 4.18.

The test procedure defines that striker mass is released from 230 mm ± 2 mm above of the highest point of the rim flange with zero velocity. However, it requires too much computing time in computer simulation. To overcome this, the striker mass is released from about 30 mm above of the highest point of the rim flange with a velocity based on the energy conversation. During the falling of the striker in computer simulations, its motion is restricted in horizontal directions and about all axes, namely it has one freedom in vertical direction. Contact surfaces between striker and wheel with tire are defined as frictionless surfaces.

Because of the test procedure provided by vehicle manufacturer, bolts are fastened to the wheel hub adapter with a torque 12 Nm which is accomplished in LS-DYNA by initial stress section option.

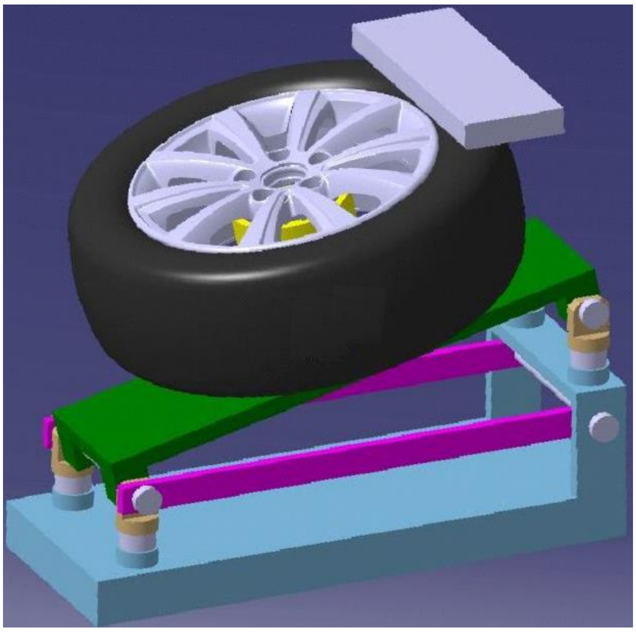

Figure 4.17. Complete 3D solid model of the impact test machine

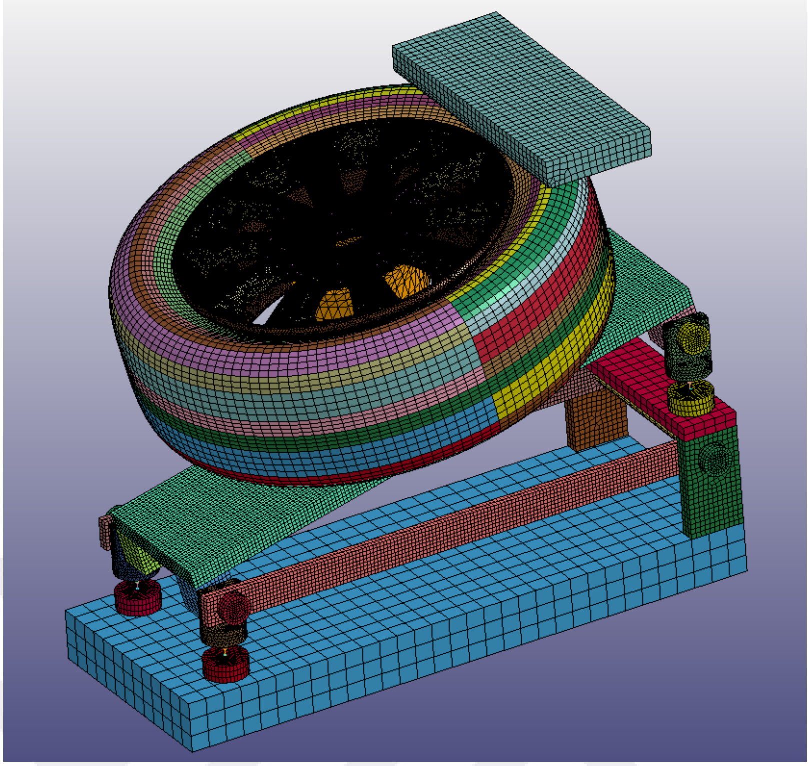

Figure 4.18. Complete FE Model of the impact test system

4.5.2. Semi-Lumped Model of the Test Systems

The system is based on combination of the former lumped models and shown in Figure 4.19.

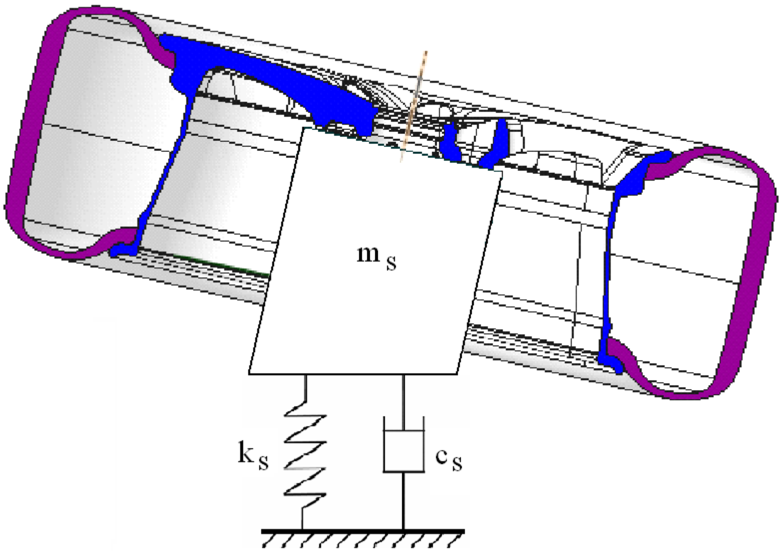

Figure 4.19. Semi-Lumped model of the impact test system

CHAPTER 5

NUMERICAL STUDIES

5.1. Comparisons of the Tire Models

Pneumatic tire is modeled in finite element analysis by using two approaches: composite pneumatic tire and simplified pneumatic tire. Composite and simplified pneumatic tires are detailed in Section 4.2.1 and 4.2.2, respectively. It is clear that simplified model has some advantages such as modeling efforts, modeling time, number of degrees of freedom in finite element model and computation time.

The function of a pneumatic tire in an impact test is to provide an inner pressure effect on the rim of the wheel. Bead wires of the pneumatic tire provide a circumferential resistance force to inner and outer flange of the rim of the wheel. Therefore, comparisons of the models should be based on the functionality of the tire.

The displacements of wheels with two different tire models under the inner pressure 0.2 MPa are found. The displacements of the rim and tire are shown in Figures 5.1-5.4.

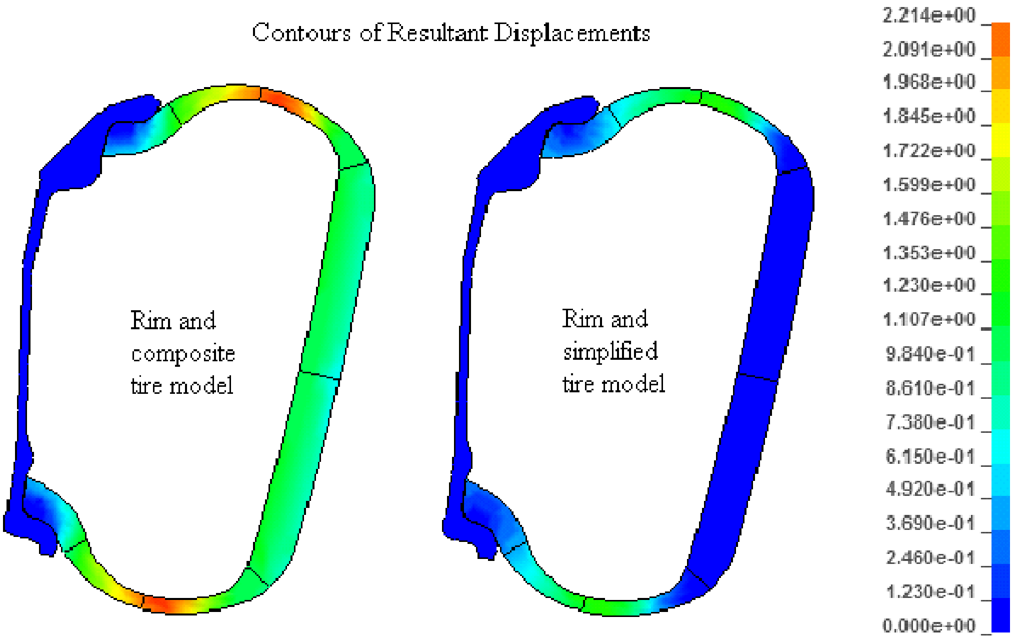

Figure 5.1. Comparison of total displacements for the tire models

If the functionality of the tire on impact test given above is considered, it is seen from Figure 5.1 that total displacements of both models are in good agreements.

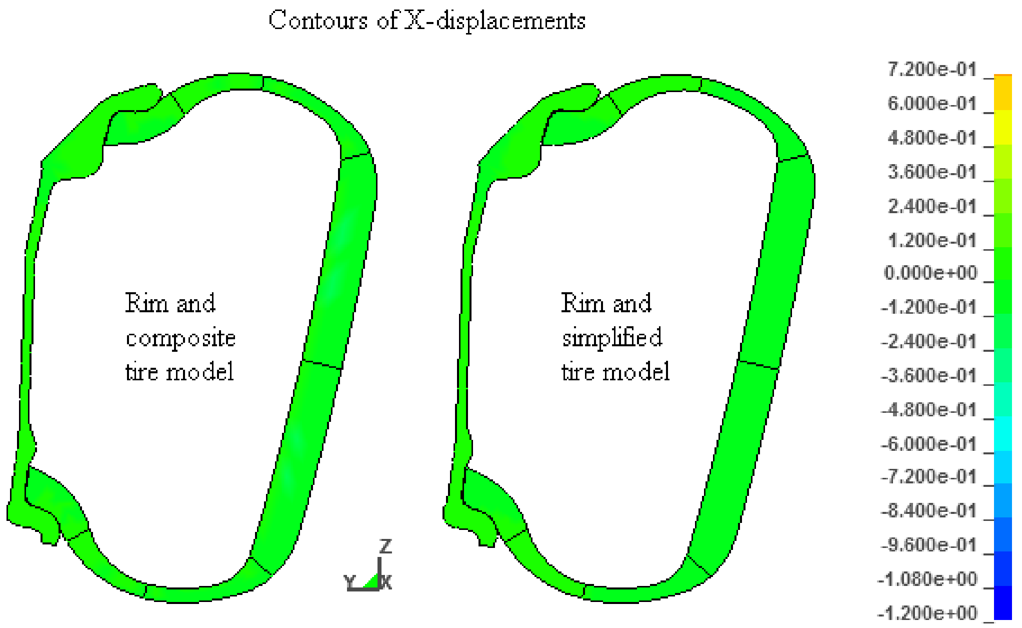

Figure 5.2. Comparison of X-displacements for the tire models

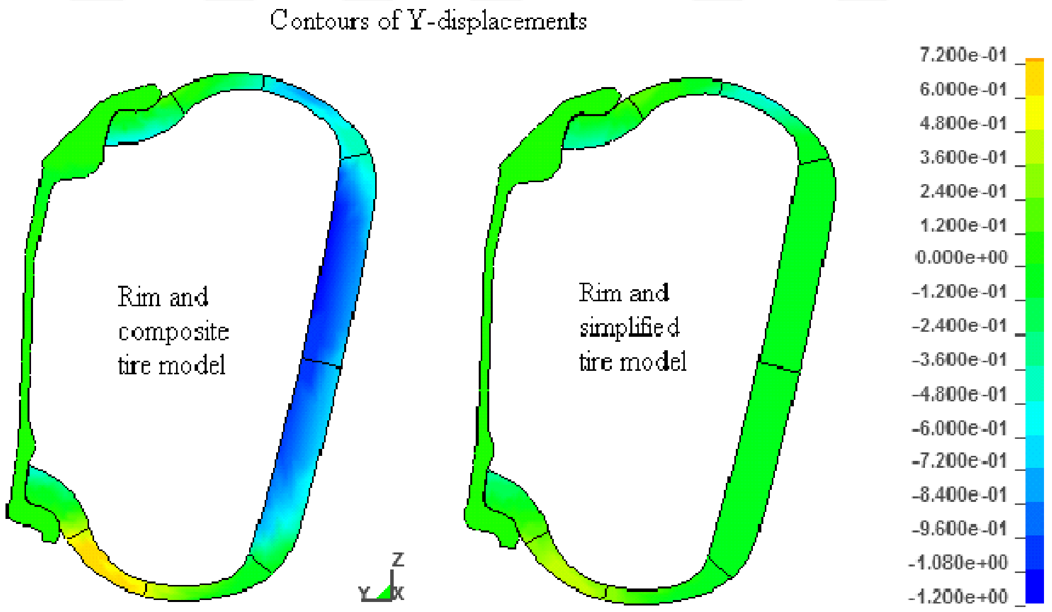

Figure 5.3. Comparison of Y-displacements for the tire models

It is seen from Figures 5.2 and 5.3 that displacements of both models in the region of rim and bead of the tire are in good agreements.

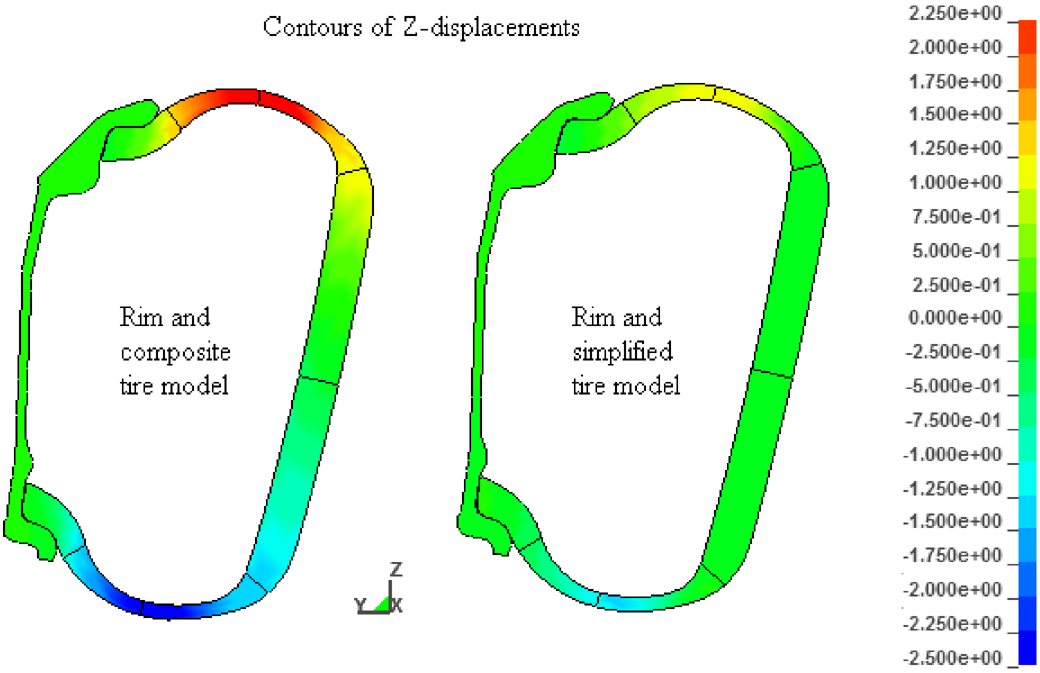

Figure 5.4. Comparison of Z-displacements for the tire models

The comments stated for Figures 5.1-5.3 can be said one more time for Figure 5.4.

5.2. Theoretical Verification of the Wheel Hub Adapter Structure

Under the vertical calibration load 1000 N, static displacements of the midpoint of the beam defined in ISO7141 for the two following models are found and compared with respect to each other:

1. 3D FE model of wheel hub adapter structure
2. 1D/2D FE model of wheel hub adapter structure

The results are given in Table 5.1.

Table 5.1 Comparisons of wheel hub adapter structure models

Model	Displacements (mm)
3D FE model of wheel hub adapter structure	7.77
1D/2D FE model of wheel hub adapter structure	7.82

It can be shown that the structure models are consistent with each other.

5.3. Effect of Tire Models on the Impact Test

To see the effect of different tire models on the vertical displacements of the impact point of the wheel and von-Mises stress occurring on the spoke near to the impact point, wheels with composite tire models and simplified tire models are considered.

For the impact load, 900 kg is selected although the normal impact load is about 500 kg. Wheel$_2$ with tire on 3D FE model of test stand is simulated in LS-DYNA for impact loading response.

The maximum vertical displacements of the impact point of the wheel$_2$ with different tire models and maximum von-Mises stresses occurring on the spoke in the same radial direction with the impact point are given in Table 5.2.

It should be stated that the vertical displacements and von-Mises stresses are based on dynamic response, namely obtained from time simulation of the system.

Table 5.2 Comparisons of tire models

	Vertical displacements (mm)	Stress (MPa)
3D FE with composite tire	56.8	270
3D FE with simplified tire	54.3	259
Difference %	100x(56.8-54.3)/56.8=4.4	100x(270-259)/270=4.1

It is clear that finding the vertical displacements and stresses based on the composite tire model requires a FE model having more degrees of freedom comparing to another one. Also, the model with composite tire needs more computation time. However, simplified tire model provides simplicity and less computation time if the percentile difference is considered in the acceptable range.

5.4. Stiffness Curve of the Lumped Model of the Wheel Hub Adapter

The lumped model of the wheel hub adapter structure shown in Figure 4.16 is considered here. Following the procedure given in Section 4.4.3, stiffness characteristics of the 3D FE model of system is found. The displacements of the top center of the wheel hub adapter shown in Figure 2.2 are found, tabulated in Table 5.3 and plotted in Figure 5.5.

Table 5.3. Stiffness characteristics k_s of the system in Figure 4.18

Force (N)	Deflection (mm)
0	0
-10000	-8.08
-20000	-12.99
-30000	-15.70
-40000	-17.64
-50000	-19.44
-60000	-20.81
-70000	-22.13
-80000	-23.48
-90000	-24.80
-95000	-25.46

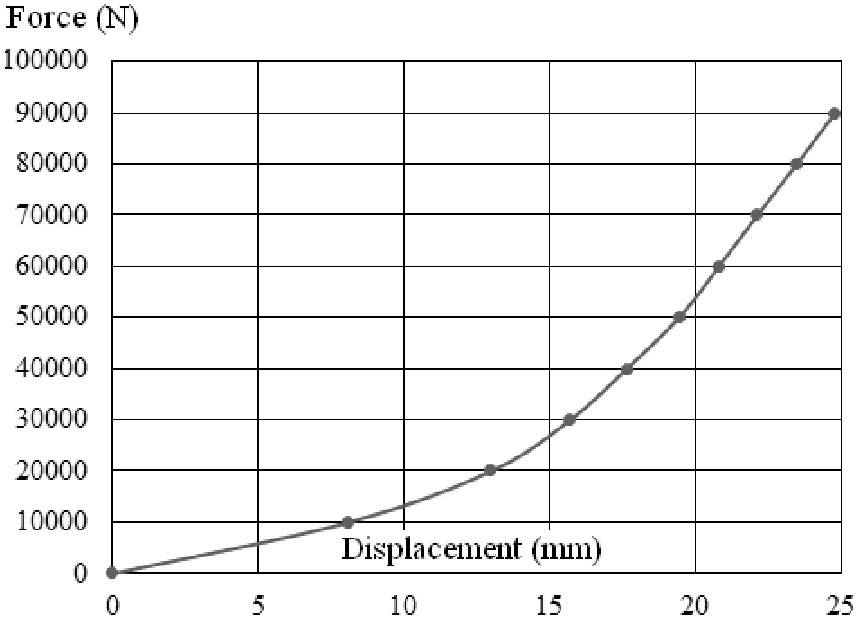

Figure 5.5 Stiffness characteristics k_s of the system in Figure 4.16

5.5. Static Simulations with Semi-Lumped Model

The semi-lumped model shown in Figure 4.19 has been modified here as shown in Figure 5.6 by adding a vertical static force *F* acting on the impact point to find the stiffness characteristics of the impact point of the wheel$_1$ and wheel$_2$ with the simplified tire.

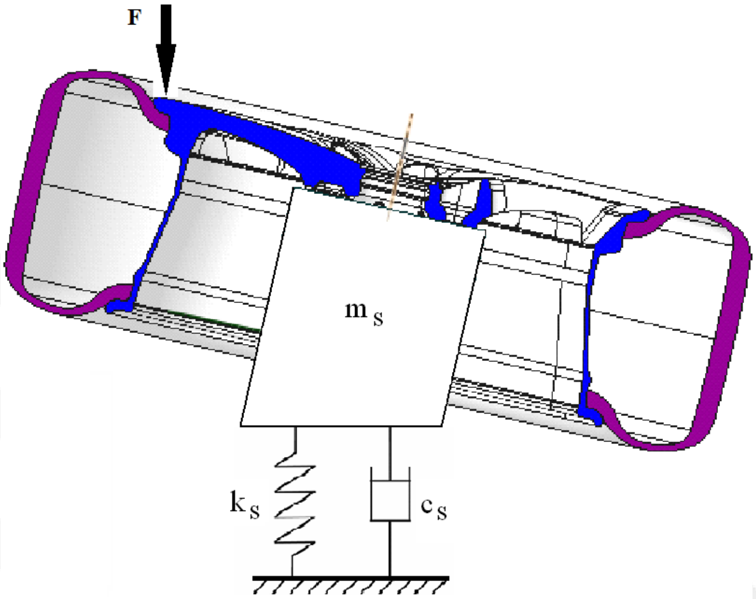

Figure 5.6. Semi-lumped model for the impact point stiffness

To find the stiffness characteristics of the semi-lumped model at the impact point in vertical direction, multi-step static analyses are carried out in Workbench for wheel$_1$ and wheel$_2$ by following the procedure explained in Section 2.13.3. The hub adapter structure is modeled as COMBIN39 nonlinear spring and a point mass. It is known that damping coefficient c_s is not effective on static analysis. SOLID187 and SOLID186 are used for finite element modeling of the wheels and the tire, respectively. The same material properties at the dynamic analyses are used in the static analysis. In the first step, only static pressure inside of the tire is defined, then the force acting on the impact point of the wheels is increased gradually at each analysis step.

As result of the multi-step static structural analyses, the displacements where the force acting on and the maximum von Mises stress on the wheels are obtained simultaneously. Stiffness characteristics of the semi-lumped models and the maximum von-Mises stresses are given in Table 5.4 and Table 5.5.

Table 5.4. Stiffness characteristics and von-Mises stresses for $wheel_1$

Force (N)	Displacement of impact point (mm)	von-Mises stresses (MPa)
0	0.00	0.58
10000	8.85	52.14
20000	14.47	104.5
30000	17.96	111.95
40000	20.95	117.66
50000	23.95	127.71
60000	28.16	145.09
70000	34.27	171.11
80000	42.14	202.75
90000	50.00	234.39
95000	53.95	250,21

Table 5.5. Stiffness characteristics and von-Mises stresses for $wheel_2$

Force (N)	Displacement of impact point (mm)	von-Mises stresses (MPa)
0	0.00	9.84
10000	9.48	85.21
20000	15.88	124.48
30000	20.47	129.12
40000	24.92	142.20
50000	29.82	161.24
60000	36.82	189.40
70000	47.44	229.94
80000	61.71	279.89

The results given in Table 5.4 and Table 5.5 are plotted as force-displacement curves and shown in Figure 5.7. Moreover, the von-Mises stress values given in second and third columns of Table 5.4 and Table 5.5 are given in graphical forms in Figure 5.8.

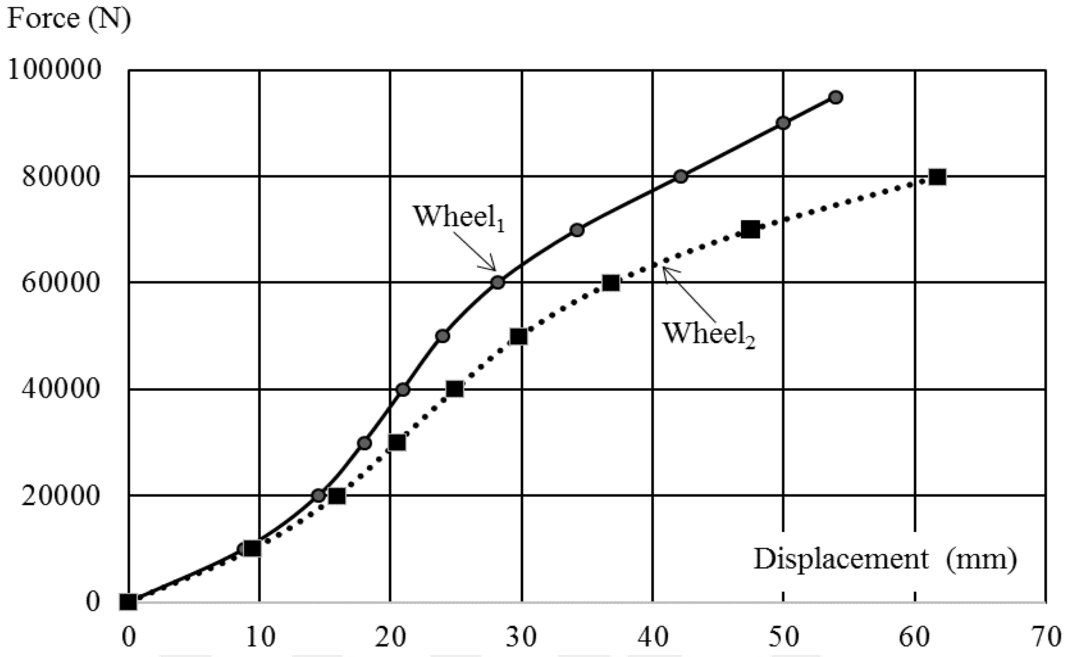

Figure 5.7. Stiffness characteristics of the system for wheel$_1$ and wheel$_2$

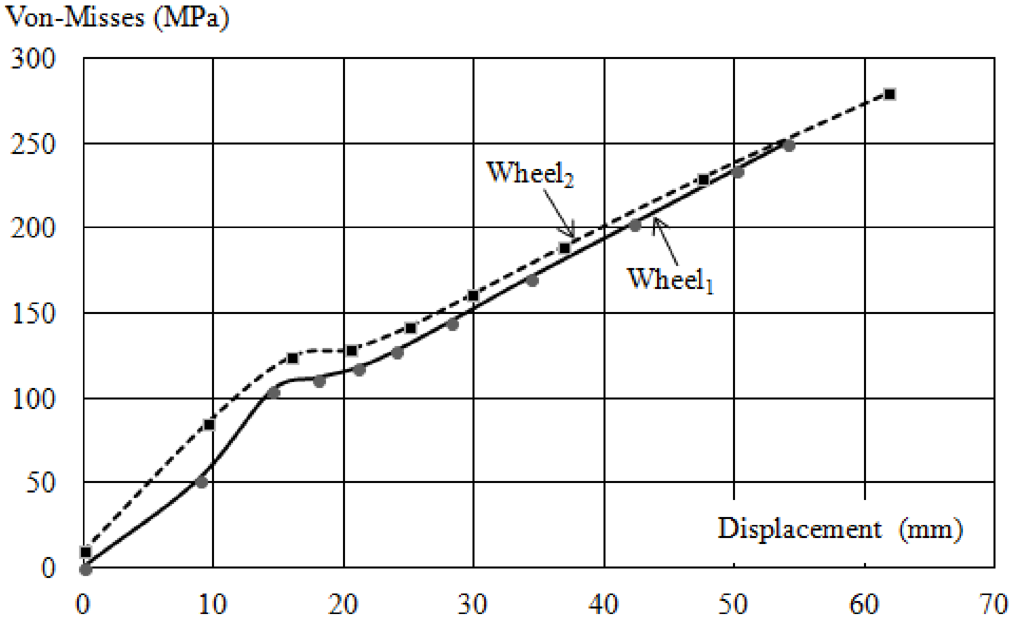

Figure 5.8. von Mises stresses versus displacements for wheel$_1$ and wheel$_2$

von Mises stress distributions under the static loads 95000 N and 80000 N acted on the impact point of the wheel$_1$ and wheel$_2$ are shown in Figure 5.9 and Figure 5.10.

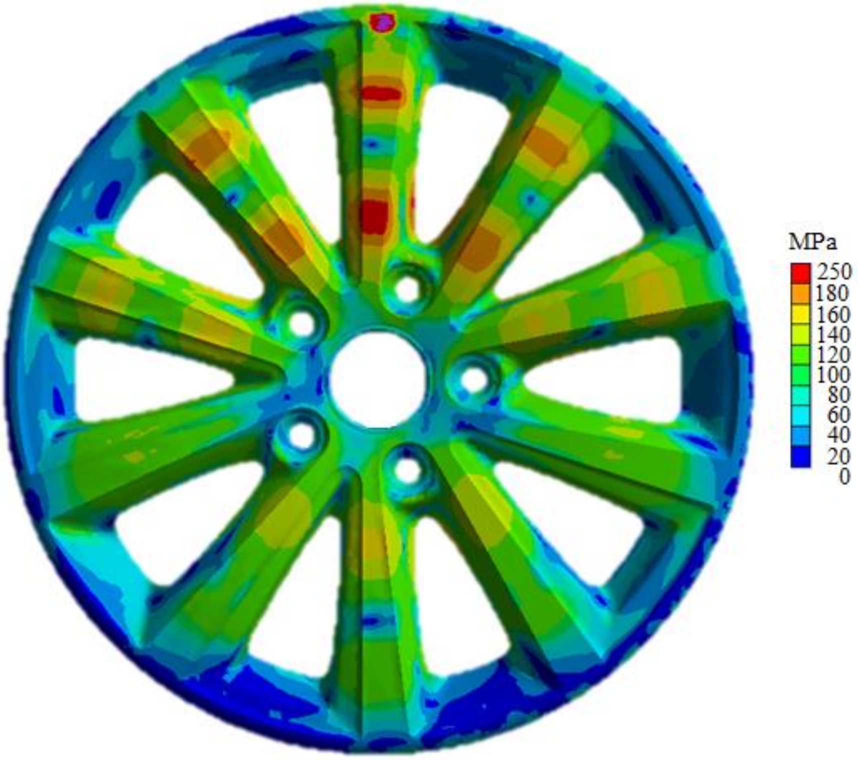

Figure 5.9. von Mises stress distribution of wheel$_1$ under static load 95000 N

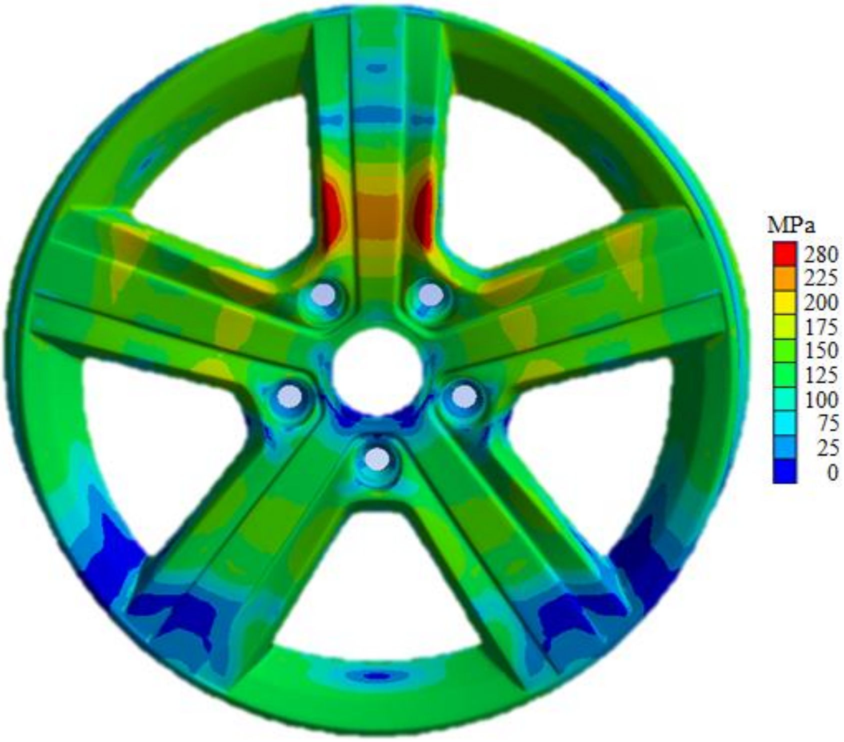

Figure 5.10. von Mises stress distribution of wheel$_2$ under static load 80000 N

Stiffness curves of the semi lumped model given in Figure 5.7 for wheel$_1$ and wheel$_2$ can be obtained as polynomial functions of displacement by using MATLAB (MathWorks, 2015). The best fitting polynomial function for the force-displacement curve for wheel$_1$

$$\begin{aligned} P_{s1}(\delta) = &-0.0001\delta^6 + 0.0249\delta^5 - 1.5486\delta^4 + 41.779\delta^3 \\ &- 425.7\delta^2 + 2516\delta + 31.78 \end{aligned} \tag{5.1}$$

where $P_{s1}(\delta)$ is in (N) and δ is the vertical displacement of the impact point of wheel$_1$ in (mm). Similarly, the force-displacement curve for wheel$_2$ is found as below

$$P_{s2}(\delta) = 0.0209\delta^4 - 3.0071\delta^3 + 127.91\delta^2 + 51.002\delta + 233.99 \tag{5.2}$$

R-squared values of the polynomials of $P_{s1}(\delta)$ and $P_{s2}(\delta)$ are 0.9997 and 0.9994, respectively. Comparison of the polynomial and the stiffness curves for wheel$_1$ and wheel$_2$ are given in Appendix A.

As discussed in Sections 2.10 and 2.12, the area under the Force-displacements curves shown in Figure 5.7 for wheel$_1$ and wheel$_2$ gives the elasto-plastic energies of the semi lumped systems. If Equations (5.1) and (5.2) are integrated with respect to δ, similar to the right hand side of Equation (2.53), the elasto-plastic strain energy denoted as $SE_{ep}(\delta)$ are found.

During the impact test, the striker is dropped from 230 millimeters above to impact point of the wheel. When the striker hits the wheel, it keeps falling down. If the distance between the initial and lowest position of the impact point of the wheel is represented as δ, Equation (2.53) can be rewritten as below

$$Mg(0.230 + \delta) = SE_{ep}(\delta) \tag{5.3}$$

where M is the impact load in kg and g is the gravitational acceleration.

To find the solution of the Equation (5.3) for different impact loads for wheel$_1$ and wheel$_2$, the MATLAB codes are given in Appendix B and C, respectively. Graphical representations of these solutions are indicated by the points D1, D2, and D3 for different impact loads in Figures 5.11 and 12.

Now, the maximum von Mises stress on the wheel can be found for any solution point such as D1 by using linear interpolation techniques applied to data available in Table 5.4 and Table 5.5. It should be noted that if the allowable maximum von Mises stress is known, δ_{max} corresponding to that value can be interpolated from Table 5.4 and Table.5.5. Moreover, maximum impact load M_{max} can also be found by using δ_{max} in Equation (5.3).

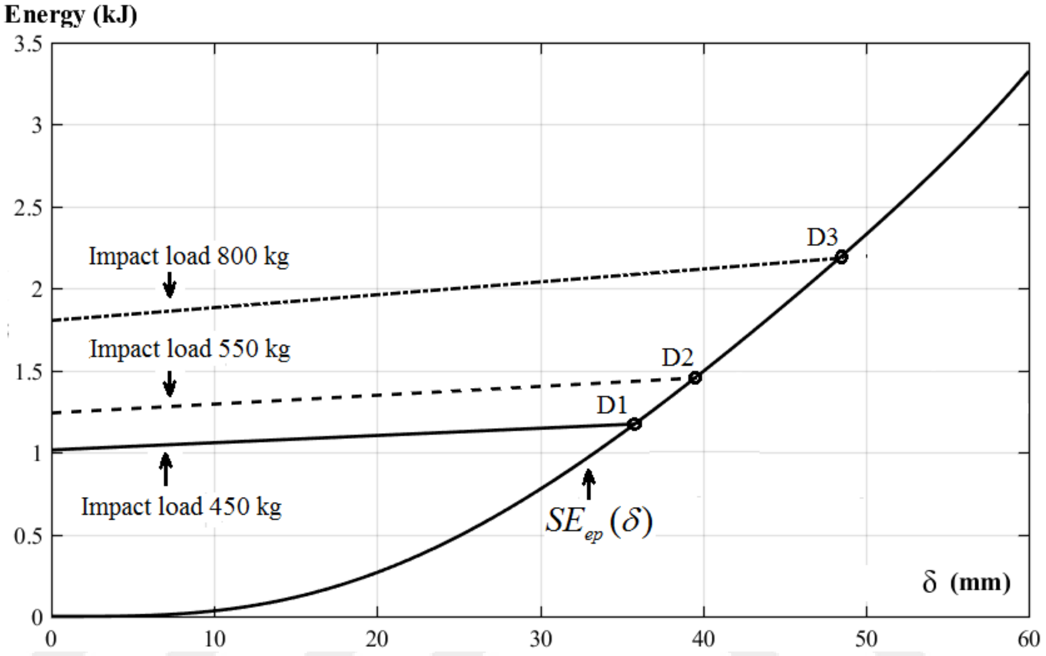

Figure 5.11. Graphical representation of the solution of Equation (5.3) for $wheel_1$

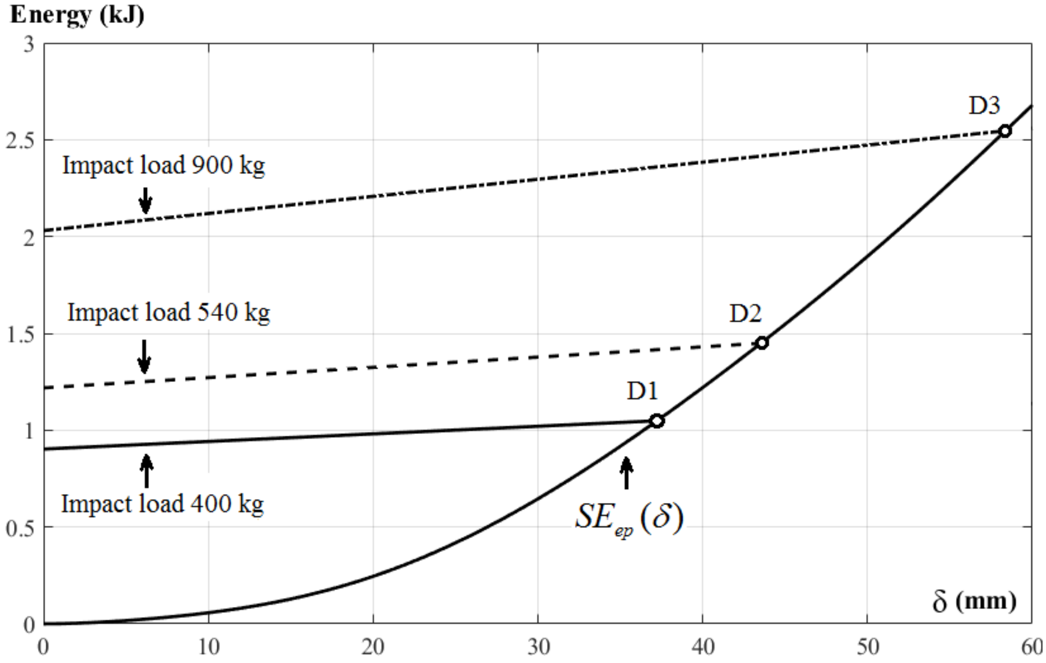

Figure 5.12. Graphical representation of the solution of Equation (5.3) for $wheel_2$

5.6. Experimental Verification of the Dynamic 3D FE Model

In this section, plastic deformation values of the impact region of the wheels obtained from the experiments and dynamic simulations in LS-DYNA are compared.

Experimental results and the results of 3D model of wheel$_1$ with tire and wheel$_2$ with tire are presented in Table 5.6.

Table 5.6. Comparison of experimental and numerical plastic deformations

Model	Impact load (kg)	Experimental results (mm)	Numerical results (mm)	Difference %
wheel$_1$+tire	450	6,603	6,677	1%
wheel$_1$+tire	550	8,403	9,305	11%
wheel$_1$+tire	800	16,348	17,147	5%
wheel$_2$+tire	540	11,001	11,995	9%
wheel$_2$+tire	400	6,424	6,478	1%

5.7. Comparisons of Dynamic and Static Models of the Test Systems

In this section, the von Mises stress distribution in the wheel due to impact load in the dynamic model is compared with the static approach.

According to the impact load and the wheel model given in Table 5.7, vertical displacements at the impact point and maximum von Mises stresses occurred in the wheel$_1$ and the wheel$_2$ are found.by using dynamic and static models.. All results in this section are given in Table 5.7.

The last column of Table 5.7 shows the percentage difference of the von-Mises stresses given in the third and fourth column of the Table 5.7. The formula used for the percentage difference is as follows

$$\%Difference = 100\frac{DynamicModel - StaticModel}{DynamicModel} \tag{5.4}$$

Table 5.7. Comparison of maximum von Mises stresses

Model	Impact load (kg)	Deflection in static model (mm)	Deflection in dynamic model (mm)	Von Mises Stress (MPa)		
				Static model	Dynamic model	Difference (%)
$wheel_1$+tire	450	35.39	34.4	175.6	174	-0.9%
$wheel_1$+tire	550	39.17	39.4	190.8	192	0.6%
$wheel_1$+tire	800	48.15	51.34	226.9	239	5%
$wheel_2$+tire	400	37.60	32.2	192.4	175	-9.9%
$wheel_2$+tire	540	43.82	39.5	216.1	210	-2.9%
$wheel_2$+tire	900	58.96	56.8	270.3	270	-0.1%

Therefore, the static model based on energy approach can be used for finding the von-Mises Stress distribution due to impact load acting on the wheel.

On the other hand, for example for the $wheel_2$ under 900 kg impact load, while the computational time of the static model is about 20 hours, it is about 60 hours for the dynamic model. Details of the computational time are given in Appendix D.

5.8. Important Moments of the Dynamic Impact Test Simulation

The important moments of the dynamic impact test simulation are explained in this section. The dynamic impact test simulation of $wheel_2$ was chosen, as an example, for this purpose and is illustrated in Figure 5.13. The explanations of Figure 5.13 are as follows.

a) The wheel studs are fastened to wheel hub adapter with an initial stress corresponding to torque 12 Nm. Striker mass 900 kg is released from 30 mm above the top edge of the wheel with a speed v = 1.980 m/s.
b) Until the time t = 0.0015 s, the striker falls to touch the sidewall of the tire.
c) When the time is equal to 0.012 s, the striker touches the wheel.
d) After the striker reaches its lowest position at a time of 0.055 s, it begins to move upward due to the spring back effect of the system.
e) During the spring back period of the system, the contact between the striker and the wheel is lost at time 0.0830 s.

f) While the striker keeps on moving to upward, the contact between the striker and the tire is lost at time 0.117 s.

g) The striker keeps on moving upward until the time reaches 0.193 s. This is the second highest position of the striker.

h) The striker begins to fall and touch the wheel at time 0.298 s.

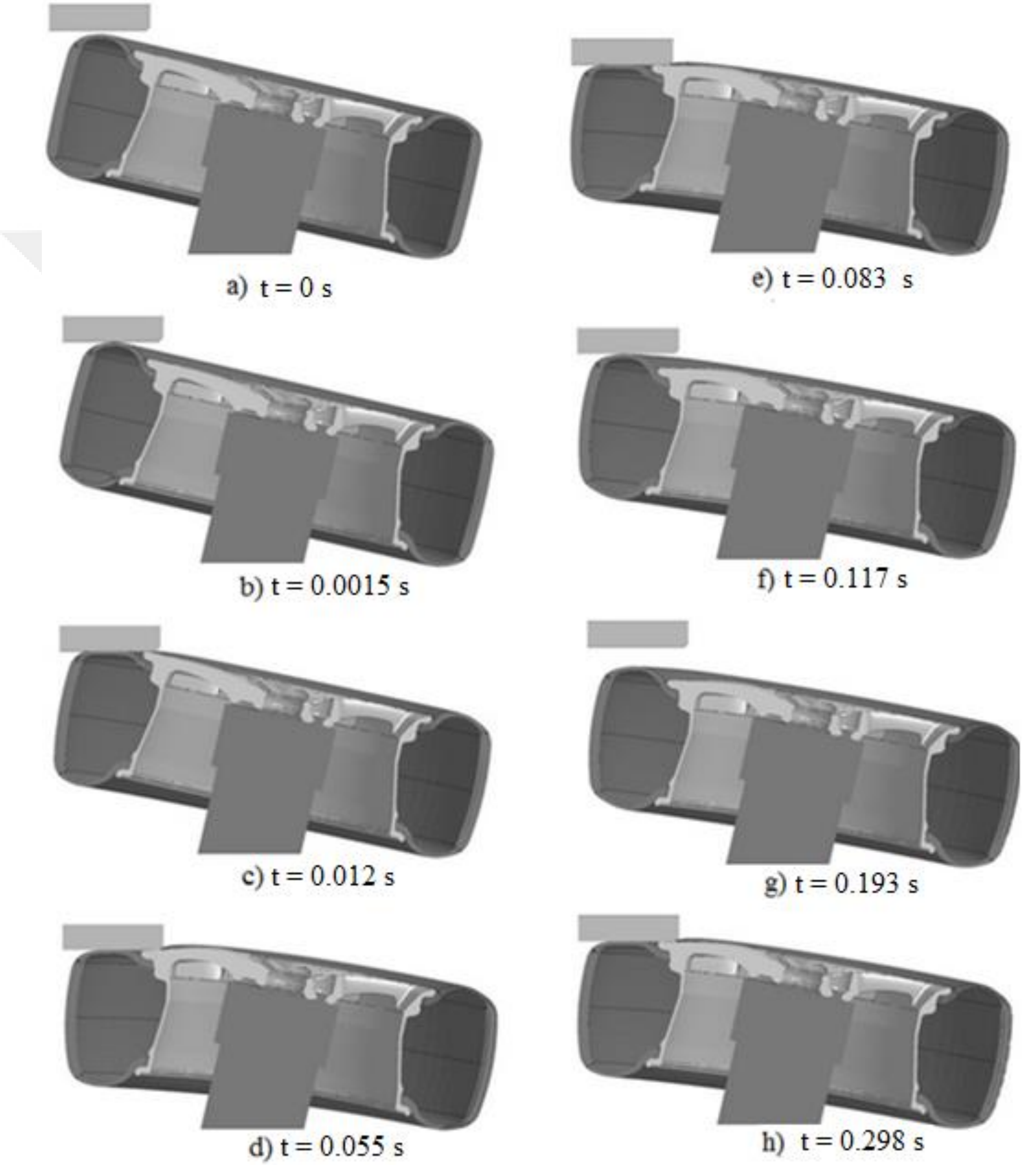

a) t = 0 s

b) t = 0.0015 s

c) t = 0.012 s

d) t = 0.055 s

e) t = 0.083 s

f) t = 0.117 s

g) t = 0.193 s

h) t = 0.298 s

Figure 5.13. Important moments of the impact test simulation

5.9. Shortening of Natural Rubbers during Impact Test

Shortening of the natural rubbers during impact test simulations are shown in Figure 5.14 and Figure 5.15.

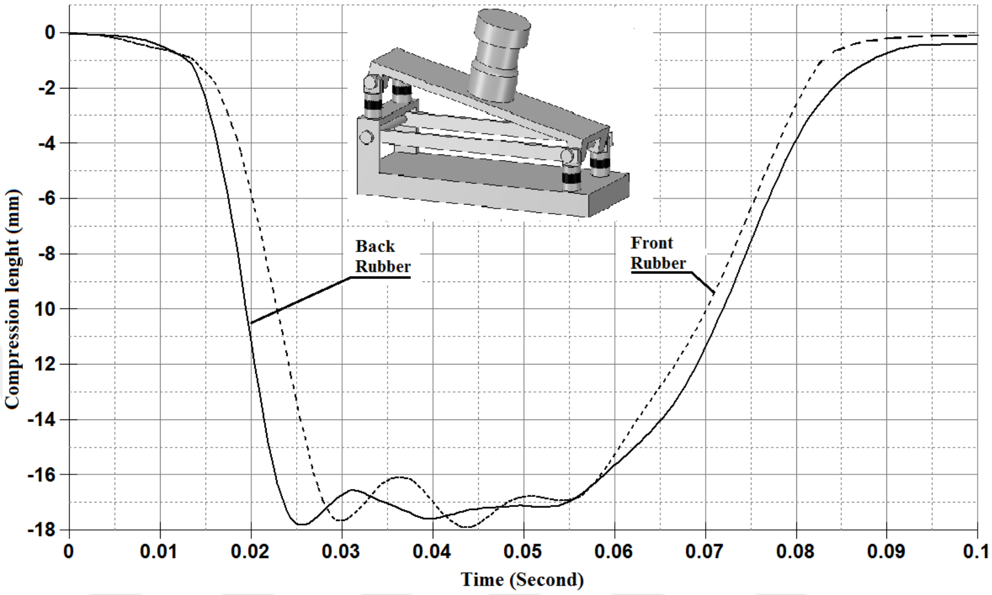

Figure 5.14. Shortening of the natural rubbers under 800 kg impact load for wheel$_1$

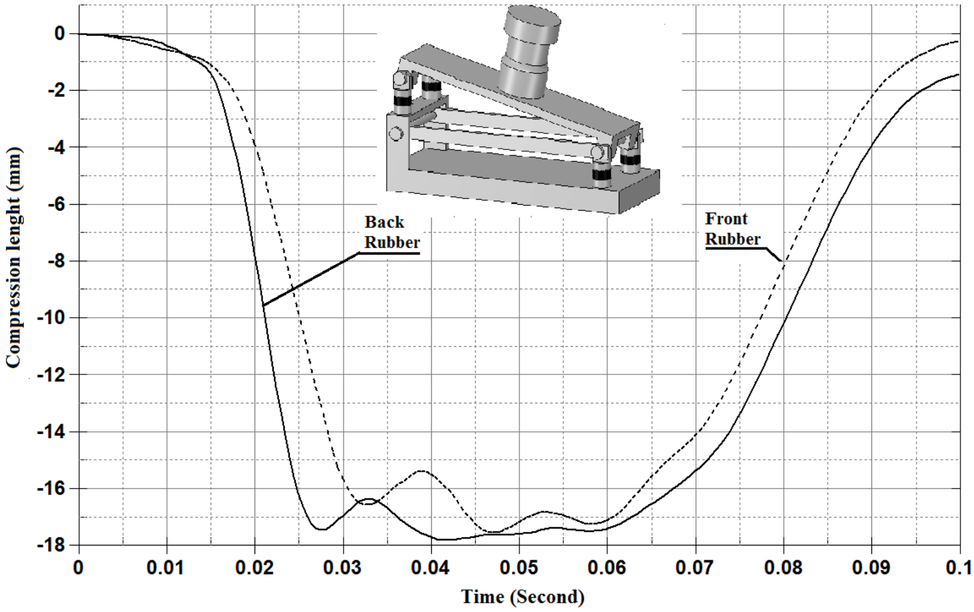

Figure 5.15. Shortening of the natural rubbers under 900 kg impact load for wheel$_2$

It can be seen from Figures 5.15 and 5.16 that shortening of rubber does not exceed the limit given in Figure 3.6 and Table 3.6.

5.10. Displacements of the Hub Adapter

The vertical displacements of top center A and bottom center B of hub adapter obtained from the dynamic simulations of the impact tests of the wheel$_1$ and wheel$_2$ under the maximum applied impact loads are plotted in Figure 5.16 and 5.17, respectively. It can be said that due to the rotation of line AB during the bending of beam, points A and B have different vertical displacements. It is noted that the maximum effective stress of the beam is found as 342 MPa which is within the elastic limit of the beam material.

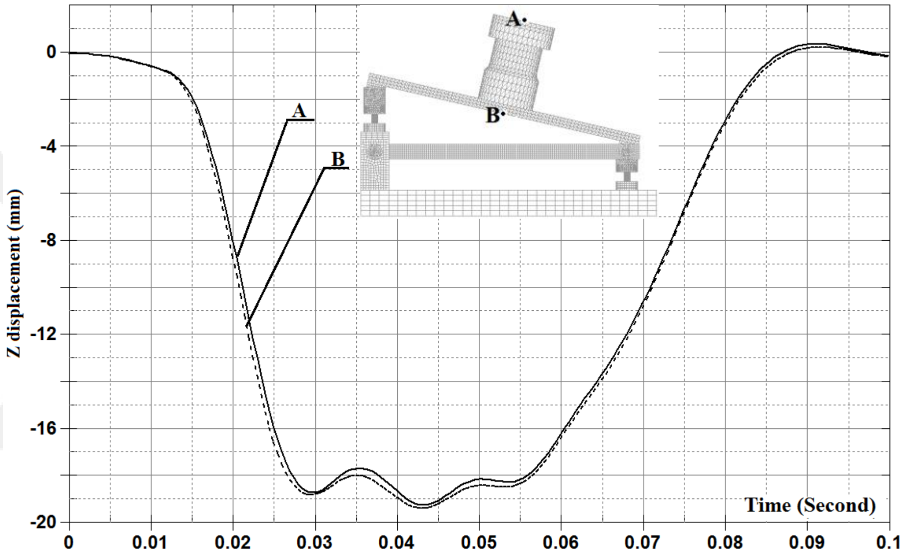

Figure 5.16. Vertical displacements of hub adapter centers A and B for wheel$_1$

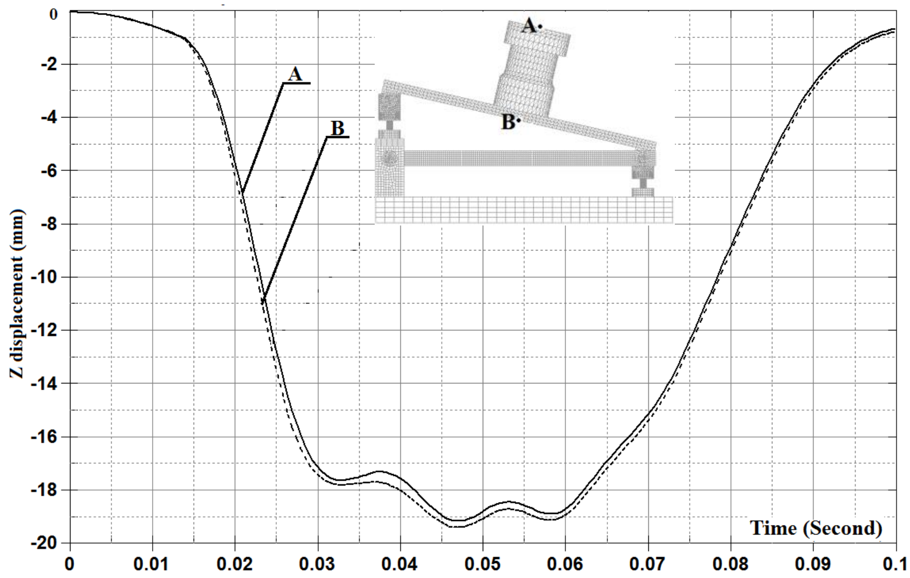

Figure 5.17. Vertical displacements of hub adapter centers A and B for wheel$_2$

5.11. Displacements and Energies of the Striker and Wheel

Displacements and kinetic energy of the striker and strain energy of the wheel$_2$ are shown in Figure 5.18.

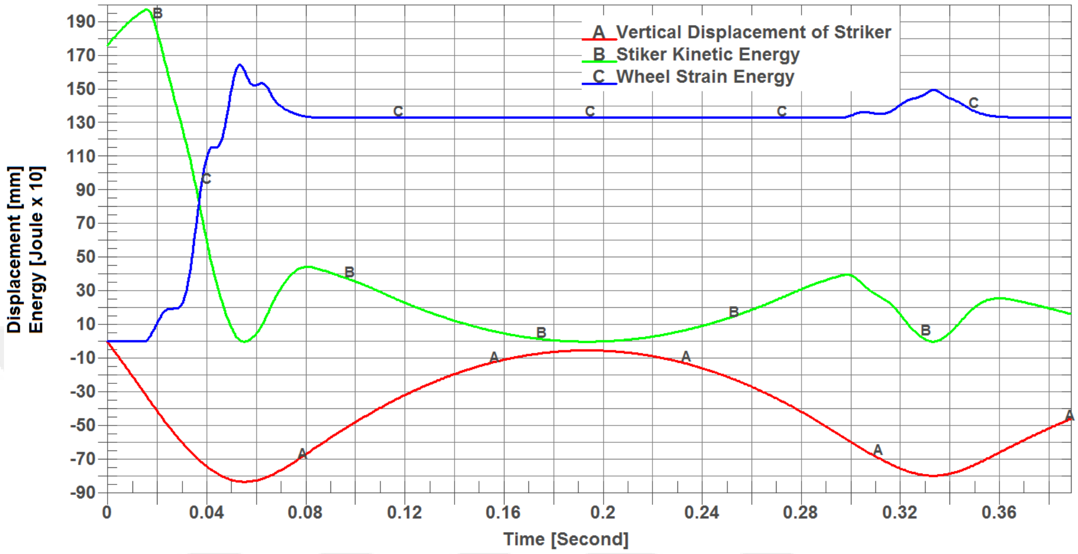

Figure 5.18. Displacements and energy variations during the test

Figure 5.18 also can be treated as the energy transformations between kinetic energy of the striker and strain energy of the wheel. It can be seen that striker starts to transfer energy to the wheel when it reaches to 30 mm with respect to its initial position.

Note that when the striker reaches its first lowest position, the kinetic energy of the striker is zero and the strain energy of the wheel is at the maximum. This shows that the maximum elasto-plastic deformation occurs during quarter of the first cycle of displacements, namely quarter of the natural vibration period. Since the time required to reach the first maximum displacement is 0.055 second, two times of this duration which is approximately 0.1 second can be taken as simulation time to evaluate the maximum stress and strain formed for this wheel. It is known that explicit analysis time is related with the termination time described in LS-DYNA. By doing this, remarkable computation time is saved. For example, in this study the termination time is 0.1 second and computing time is 2.5 days for a computer with Intel Core i7 3630 QM 2.4 GHz, 16 GB RAM configuration. Otherwise, for the full simulation time of 0.4 seconds, 9.5 days is required.

Coefficient of restitution, discussed Section 2.9, of first impact can be calculated from the ratio of first maximum kinetic energy of the striker to second maximum kinetic energy of the striker as 0.22. This means that if the damping of the system is neglected, energy dissipated for plastic deformations is 78%.

Vertical positions of the impact points of the striker and wheel with respect to a selected reference is presented in Figure 5.19.

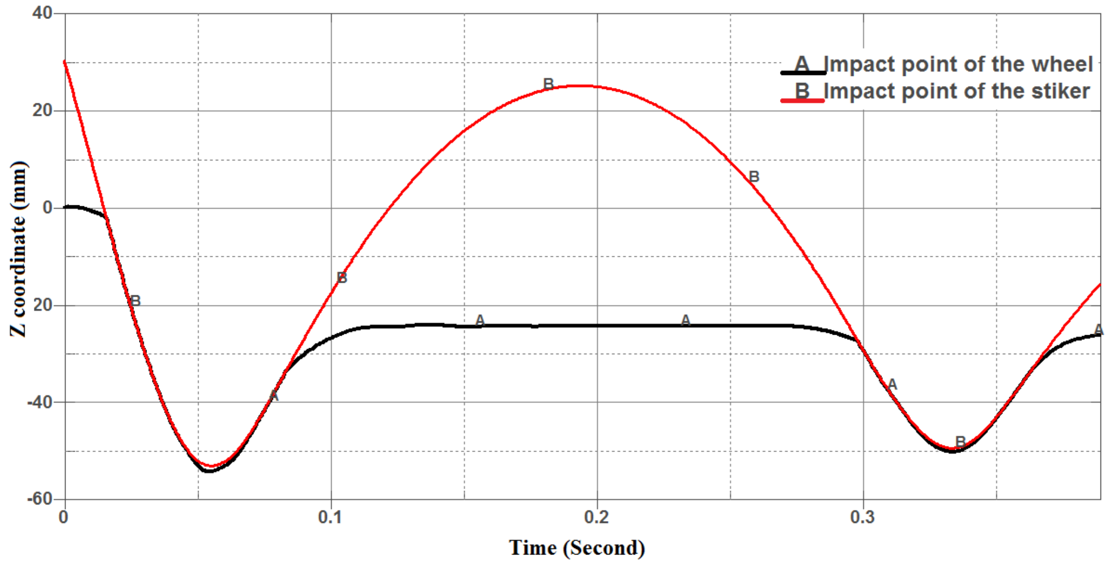

Figure 5.19. Vertical positions of wheel and striker’s impact points.

The von Mises stress distribution at 0.055 second corresponds to the time when maximum strain energy stored in the wheel is shown in Figure 5.20. Maximum stress occurs on the spoke of the wheel to which the impact load is applied.

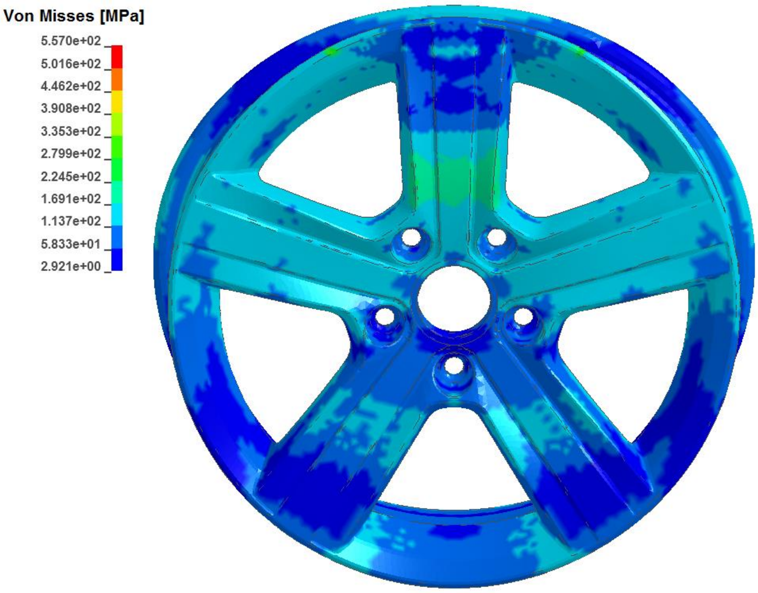

Figure 5.20. von Mises stress distribution at time 0.055 second

5.12. Investigations for Impact Test Failure Load

Here damage parameter of impact test simulation is determined by von Mises and effective plastic strain. The simulations corresponding to the experimental tests given in Table 3.9 are accomplished in LS-DYNA, and then both results are given in Table 5.7.

Table 5.8. Comparison of experimental results with dynamic simulation results

Wheel number	Alloy type	Impact load (kg)	Dynamic Simulation Results		Experimental impact test result
			Maximum von Mises stress (MPa)	Maximum % effective strain	
1	AlSi11Mg	450	175	3.7	No fracture
1	AlSi11Mg	550	185	4.5	No fracture
1	AlSi11Mg	800	230	7	No fracture
2	AlSi11Mg	400	175	3.5	No fracture
2	AlSi11Mg	540	210	5.3	No fracture
2	AlSi11Mg	900	270	8.5	No fracture
3	AlSi11Mg	468	174	3.6	No fracture
4	AlSi11Mg	396	243	7.1	No fracture
5	AlSi7Mg	825	252	4.5	Fracture
5	AlSi7Mg	775	243	3.9	No fracture
5	AlSi7Mg	725	237	3.4	No fracture
5	AlSi7Mg	675	231	2.9	No fracture
5	AlSi7Mg	627	227	2.6	No fracture
6	AlSi7Mg	775	269	5.9	Fracture
6	AlSi7Mg	725	261	5.3	No fracture
6	AlSi7Mg	625	258	5	No fracture
6	AlSi7Mg	575	254	4.7	No fracture
6	AlSi7Mg	525	247	4.2	No fracture
7	AlSi7Mg	800	247	4.2	No fracture
7	AlSi7Mg	750	243	3.9	No fracture
7	AlSi7Mg	700	237	3.4	No fracture
7	AlSi7Mg	650	235	2.7	No fracture
8	AlSi7Mg	468	265	5.4	No fracture
8	AlSi7Mg	468	265	5.4	Fracture
9	AlSi7Mg	558	250	4.4	No fracture
9	AlSi7Mg	558	250	4.4	Fracture
10	AlSi7Mg	573	220	1.9	No fracture
11	AlSi7Mg	850	343	11	Fracture
12	AlSi7Mg	615	233	3.1	No fracture
13	AlSi7Mg	585	227	2.6	No fracture
14	AlSi7Mg	498	250	4.1	Fracture

It should be noted that the stress and strain obtained from the simulations are true stress and true strain.

As an example from the Table 5.7, wheel$_5$ under impact load 825 kg is selected to illustrate the crack occurred due to impact load and von Mises stress distribution on wheel. Aforementioned illustrations are shown in Figures 5.21 and 5.22, respectively.

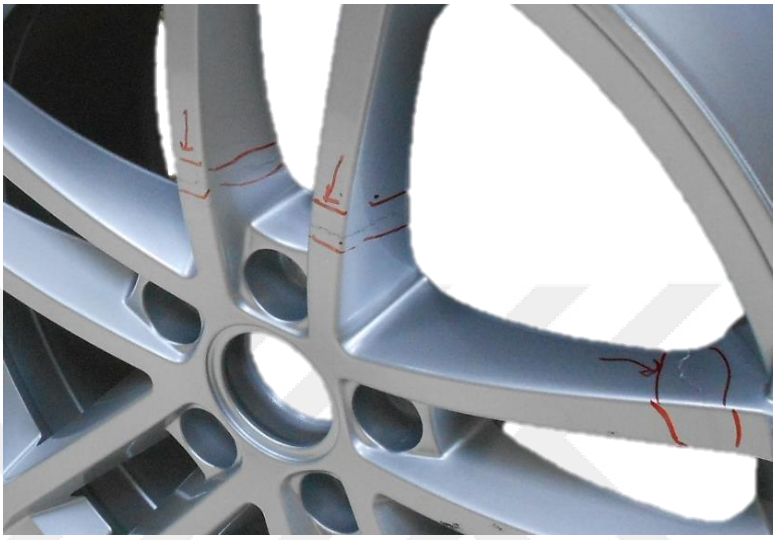

Figure.5.21 Experimental impact test result of the wheel$_5$ under impact load 825 kg

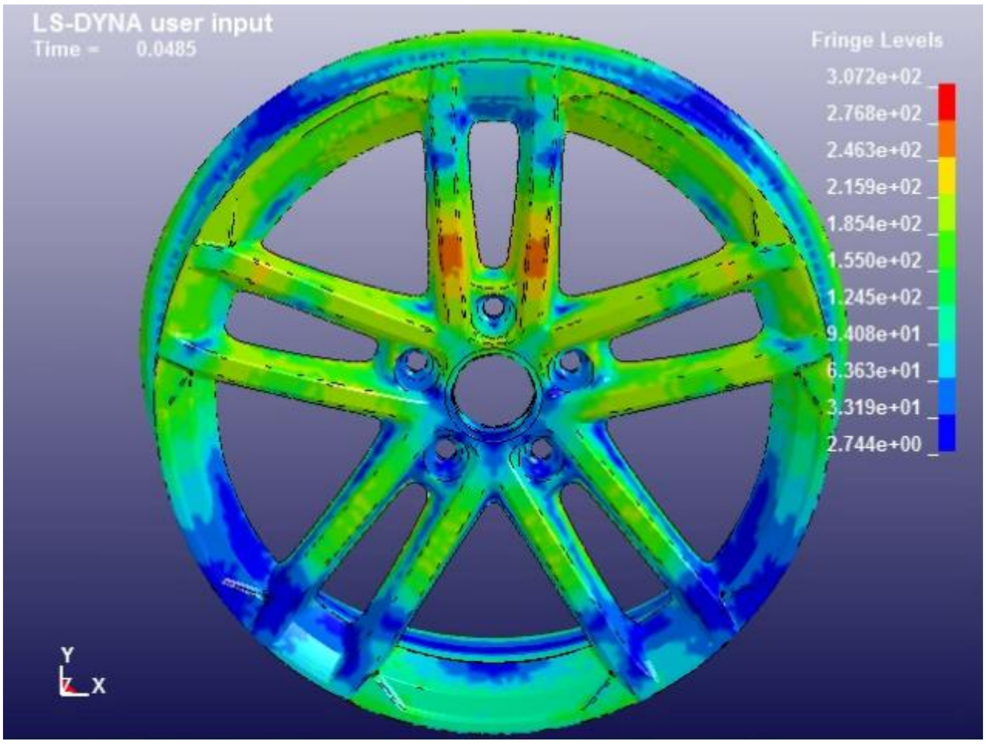

Figure 5.22. The von Mises stresses on the wheel$_5$ under impact load 825 kg.

It can be seen from Figures 5.21 and 5.22 that fractures occur where the maximum von Mises stresses find on the wheel.

The box plot technique defined in Section 2.15 is used to classify and compare the experimental and simulation results given in Table 5.8. Maximum von Mises stresses and maximum effective strains of AlSi7Mg alloy wheels available in Table 5.8 are presented in the box plots in Figures 5.23 and 5.24, respectively.

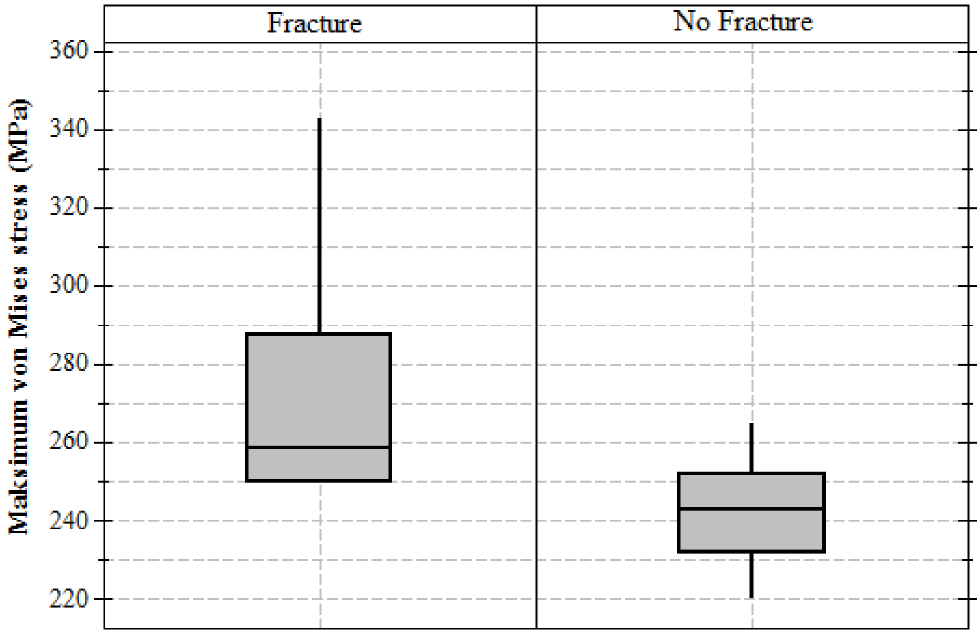

Figure 5.23 Box plots of AlSi7Mg alloy wheels for stresses

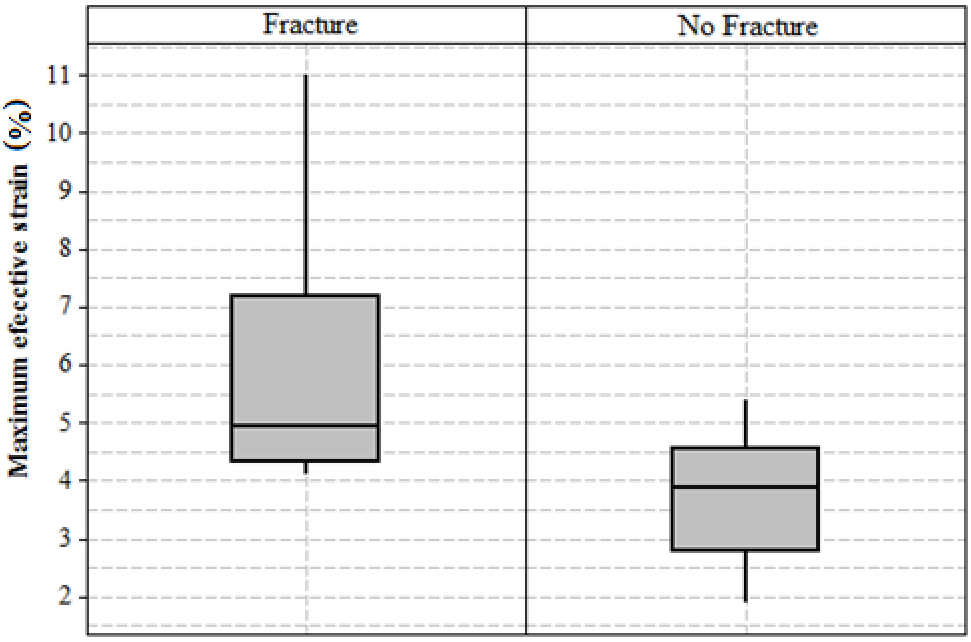

Figure 5.24 Box plots of AlSi7Mg alloy wheels for strains

When Figures 5.23 and 5.24 are examined, it can be said that if the maximum von Mises stress is more than approximately 250 MPa or the maximum effective strain is more than approximately 0.045, the wheel fails in the experimental impact test.

There is no impact test failure for the AlSi11Mg alloy wheels in Table 5.8. The box plots of numerical maximum von Mises and maximum effective strain values for the AlSi11Mg alloy wheels are shown in Figure 5.25.

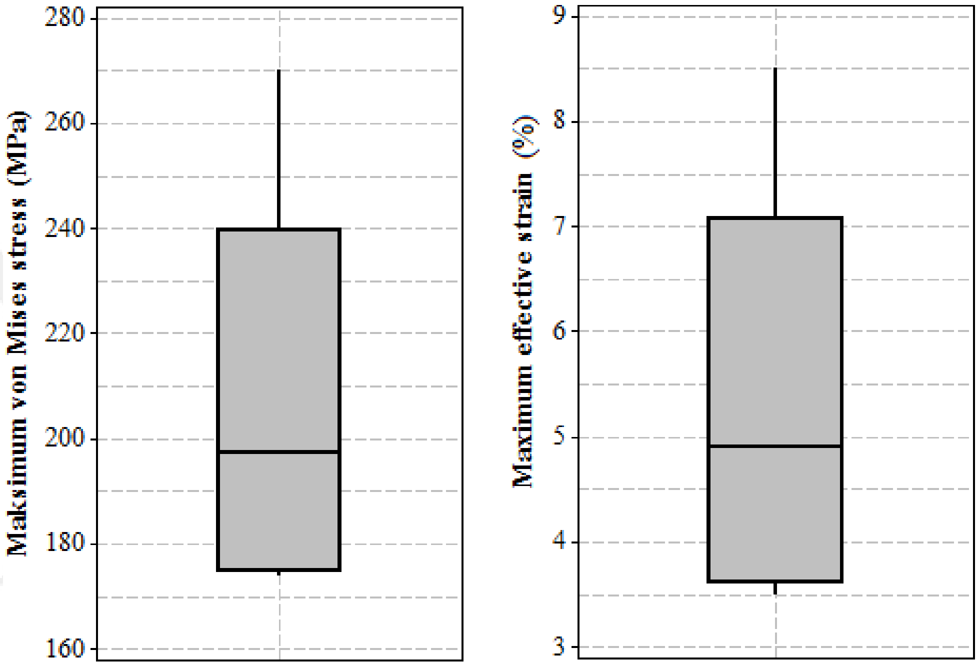

Figure 5.25 Box plots of AlSi11Mg alloy wheels for stress and strain

If Figure 5.25 is examined by considering median values, it can be said that if the maximum von Mises stress is less than 200 MPa or the maximum effective strain is less than 0.05, the wheel does not fail the experimental impact test.

The maximum von Mises stress values can also be used as failure limit for the static model of impact test simulations of the AlSi17Mg and AlSi11Mg alloy wheels because the maximum von Mises stresses obtained from static model and dynamic model of impact test simulations are in good agreement as shown in Table 5.7.

CHAPTER 6

CONCLUSIONS

Finite element simulation of the wheel impact test has significant benefits to design a wheel that satisfies all design requirements. However, finite element modeling of the wheel impact test is a complex problem due to the composite structure of the tire, nonlinearity of contacts, and large and plastic deformations.

In this thesis, the nonlinear 3D dynamic and semi lumped static finite element model of the wheel impact test as described in the international standard ISO 7141 were developed for the AlSi11Mg and AlSi7Mg alloy wheels. ANSYS LS-DYNA and Workbench were used for the dynamic and static models, respectively. Different finite element models of tire, wheel hub adapter structure were developed to simplify the finite element model of the impact test by noting the accuracy of the model.

Material properties of the AlSi11Mg and AlSi7Mg alloy wheels were obtained from tensile tests. The specimens were taken from spokes of the wheels. Bilinear isotropic hardening material model of the wheel was used in numerical computations. The stiffness curve of the rubber mount of the hub adapter structure was obtained by compression tests.

In total, forty-one experimental impact tests were done for different wheel models with two different materials: AlSi11Mg and AlSi7Mg. The number of wheel model for impact tests were selected as four and nine for AlSi11Mg and AlSi7Mg alloy wheels, respectively. Plastic deformations due to impact load at the impact region of fifteen wheels were measured by using the CMM (coordinate measuring machine).

3D and 2D finite element models of the wheel hub adapter structure were obtained. In order to simplify the model, natural rubber parts of the structure were modeled as spring and damping elements. Theoretical verification of 3D and 2D finite element models of the structure were performed according to the procedure defined in ISO 7141. Furthermore, nonlinear stiffness characteristics of the wheel hub structure under a vertical load was found by finite element static analysis to obtain the lumped model of the wheel hub adapter structure.

The tire was modeled in two different ways. The first model is a composite finite element model of tire that involves bead core, casing and crown plies, tread, side wall, and bead parts of the tire. However, the second model is a simplified tire model that does not have bead core or casing and crown plies. The strength effects of these parts were taken into account using an equivalent stiffness approach in the simplified tire model. von Mises stresses on the spoke of wheel found from dynamic simulations for composite and simplified tire models were compared. Results of the simplified tire model were found to be 4.1 % less than the results of composite tire model.

3D dynamic finite element model of the impact test consists of the finite element models of the 3D wheel hub adapter structure, wheel, and composite tire model. The pressure inside the tire is modeled as an airbag in the dynamic model. Verification of the dynamic model and simulations in LS-DYNA are performed by comparing the experimental results of the plastic deformations of the impact region of the wheels with the associated numerical results. The maximum difference between these values is 11%.

The dynamic simulations show the following: the striker reaches its lowest position at time about 0.05 s. When the striker reaches its first lowest position, it transfers its total potential energy to wheel-tire and its supports. Therefore, the maximum elasto-plastic deformation of the wheel occurs during this time interval, which corresponds to quarter of the natural vibration period. Two times of this duration can be taken as simulation time to evaluate maximum stress and strain formed in the wheel.

Simulation of the failure of the impact test can be determined by using von Mises and effective plastic strain occurred in wheel. To find a critical value of the von Mises and effective plastic strain, the box plot technique is used.

Semi lumped model of the wheel impact test consists of the wheel hub adapter structure which is modeled as a nonlinear spring and a lumped mass, and wheel with simplified tire model. The force-displacement curve of the semi lumped model at the impact point in the vertical direction and maximum von Mises stresses occurrs on the wheel are found simultaneously. Elasto-plastic energy function of the semi lumped system is found. Then, using the energy balance, the maximum von Mises stress in the wheel under the corresponding impact load can be found.

Comparison of maximum von Mises stresses obtained from static and dynamic model show that the difference between the two models is less than 9.9% whereas, for example for the wheel$_2$ under 900 kg impact load, the computational time of the static and dynamic model are found as 20 and 60 hours, respectively. Namely, it is about to % 67 less than the dynamic model .Therefore, the static model based on energy approach can be used for finding the von-Mises stress distribution due to impact load acting on the wheel.

It is also shown that once the force-displacement curve of the semi lumped model is obtained, the maximum von Mises stress in the wheel under any impact load and maximum impact load of the wheel can be found without running to the static model again. Significant time can be saved by this manner.

REFERENCES

ANSYS Inc. 2009. Theory Reference for the Mechanical APDL and Mechanical Applications., Canonsburg PA.

ANSYS Inc. 2010. Lecture Notes on Mechanical Structural Nonlinearities Release 13.0 Lecture 7: Hyperelasticity, Canonsburg PA.

ANSYS Inc. 2013. Mechanical APDL Theory Reference, Canonsburg PA.

ANSYS Inc, 2015. Lecture Notes on Introduction to Structural Nonlinearities in ANSYS Mechanical.

Bass, I. 2007. Six Sigma Statistics with Excel and Minitab. New York: The McGraw-Hill.

Bathe K.J. 1996. Finite Element Procedures, Engle Cliffs: Prentice-Hall.

Beer, F.P., Johnston, E.R., Mazurek, D.F., Cornwell, P.J., Eisenberg, E.R. 2010. Vector Mechanics for Engineers Statics and Dynamics. New York: The McGraw-Hill.

Boresi, A.P., Schmidt, R.J., 2003. Advanced Mechanics of Materials. US: John Wiley & Sons.

Chang, C.L. and Yang, S.H. 2009. Simulation of wheel impact test using finite element method, *Engineering Failure Analysis* 16(5): 1711–1719.

Cheng, G, Zhao, G., Guan, Y., and Wang, Z. 2011. Study on deflection performance of radial tire by Finite Element Method, *Journals of Noise & Vibration Worldwide* 42(11):30-35.

Dirac Delta Consultants Ltd. 2016 “Friction” Accessed July 19. http://www.diracdelta.co.uk/science/source/f/r/friction/source.html#.WAVsf_mLQpY

ETRTO, 2011. Engineering Design Information. Brussels:

Garret, T.K., Newton, K. and Steeds, W. 2001. The motor vehicle, Oxford: Butterworth-Heinemann.

Gere, J.M. 2004. Mechanics of Materials. Belmont: Thomson Learning

Ginsburg, S. and Gellert, M. 1980. Numerical solution of static and dynamic nonlinear multi-degree-of-freedom systems, *Computer Method in Applied Mechanics and Engineering* 23: 111-125.

Hall, W., Jones, R.P., and Mottram, J.P. 2004. Tire modeling methodology with the explicit finite element code LS-DYNA, *Tire Science and Technology* 32: 236-261.

Harris, C.M. and Piersol, A.G. 2002. Harris' Shock and Vibration Handbook. New York: The McGraw-Hill.

Ishikawa, S., Saka, Y., and Nosaka, N. 2014. Application of impact analysis for aluminum wheel with inflated tire, SIMULIA Community Conference. http://www.3ds.com/products-services/simulia/resources/

Inman, D.J. 2014. Engineering Vibration. New Jersey: Pearson

ISO 7141. 2005. Road vehicles- Light alloy wheels -Impact test, Third edition, 2005-07-01.

Jigang, C. and Guozhi, Z. 2012. Virtual impact test for aluminum-alloy wheel based on numerical simulation method, *Advanced Materials Research* 457-458: 93-97.

Kermelk, W. 1999. Wheels for Road Vehicles, Structure, Design, and Testing, Augsburg: Verlag Moderne Indusrie.

Lee, H. 2014. Finite Element Simulations with ANSYS Workbench 14. Mission KS: SDC.

Lee, W.S, Sue, W.C., Sue, Lin, C.F., and Wu, C.J. 2000. The strain rate and temperature dependence of the dynamic impact properties of 7075 aluminum alloy, *Journal of Materials Processing Technology* 100: 116-122.

LSTC, 2015. LS-DYNA Theory Manual. Livermore CA

Madenci, E., Güven I. 2006. The Finite Element Method and Applications in Engineering Using ANSYS. New York: Springer

MathWorks, Inc. 2015. MATLABr2015b Help Menu.

Meirovitch, L. 2000. Fundamentals of Vibrations. New York: The McGraw-Hill.

Mendelson, A. 1968. Plasticity: Theory and Application. New York: MacMillan.

Neves, R.R.V., Micheli, G.B., and Alves, M. 2010. An experimental and numerical investigation on tyre impact, *International Journal of Impact Engineering* 37: 685–693.

Orengo, F, Ray, M.H., and Plaxico, C.A., 2003. Modeling tire blow-out in roadside hardware simulations using Ls-Dyna. IMECE2003-55057, ASME International Mechanical Engineering Congress & Exposition, Washington, D.C.

Petyt, M. 2010. Introduction to finite element vibration analysis. Cambridge: Cambridge University Press.

Reida, J D, Boesch, D. A., and Bielenberg, R. W. 2007. Detailed tire modeling for crash applications, *International Journal of Crashworthiness* 12(5): 521-529.

Reimpell, J., Stoll, H. and Betzler, J.W. 2001. The Automotive Chassis: Engineering Principles, Oxford: Butterworth-Heinemann.

Riesner, M, Zebrowski, M.P. Gavalier, R.J. 1986. Simulation of Wheel Impact Test, SAE paper no. 860829, The Sixth International Conference on Vehicle Structural Mechanics, Warrendale, PA.

Simo, J.C., Hughes, T.J.R. 1997. Computational Inelasticity. New York: Springer-Verlag.

Shang, R W Altenhof, N Li and H Hu. 2005. Wheel impact performance with consideration of material inhomogeneity and a simplified approach for modeling, *International Journal of Crashworthiness* 10(2): 137–150.

Timoshenko, S. 1940. Strength of Materials Part I: Elementary Theory and Problems, New York: D. Van Nostrand.

Tsai, G.C, Huang, K.Y. 2012. 13° Impact test analysis of aluminum alloy wheel, *Materials Engineering for Advanced Technologies* 631-632: 925-931.

Yardimoglu, B. 2012. Lecture Notes on Mechanical Vibrations, Izmir: Izmir Institute of Technology.

Yuan, X., Zhang, L., Chen, X., Du, B., Li, B., Fan, L. and Pan. Y., 2012. Numerical Simulation of Aluminum Alloy Wheel 13° Impact Test Based on Abacus, *Applied Mechanics and Materials* Vols. 215-216. pp 1191-1196

APPENDIX A

THE POLYNOMIAL AND THE STIFFNESS CURVES

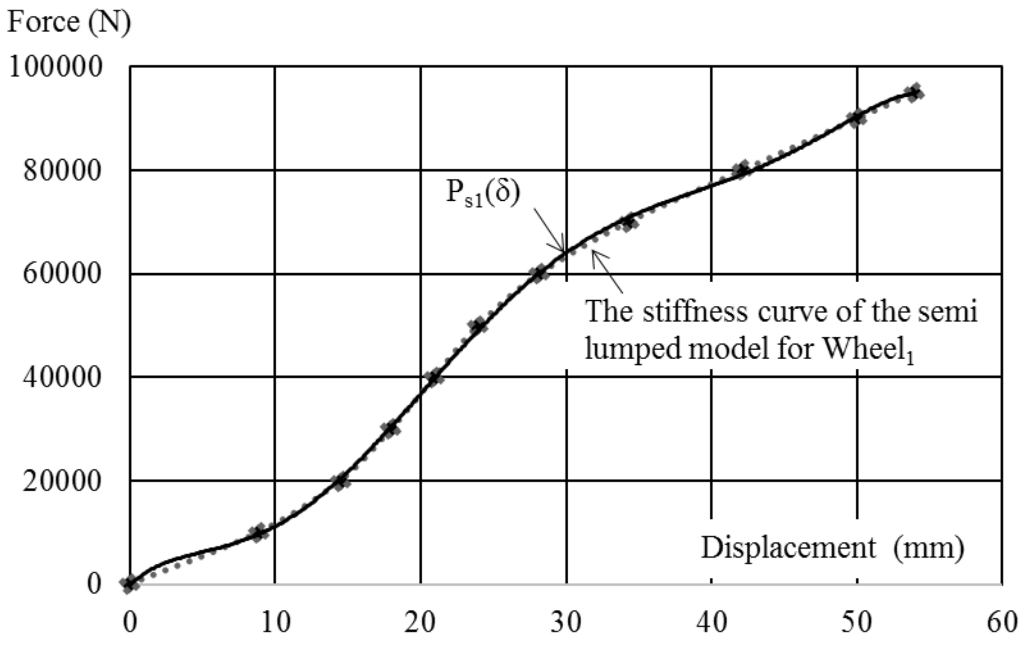

Figure A.1. Comparison of the polynomial and the stiffness curves for $wheel_1$

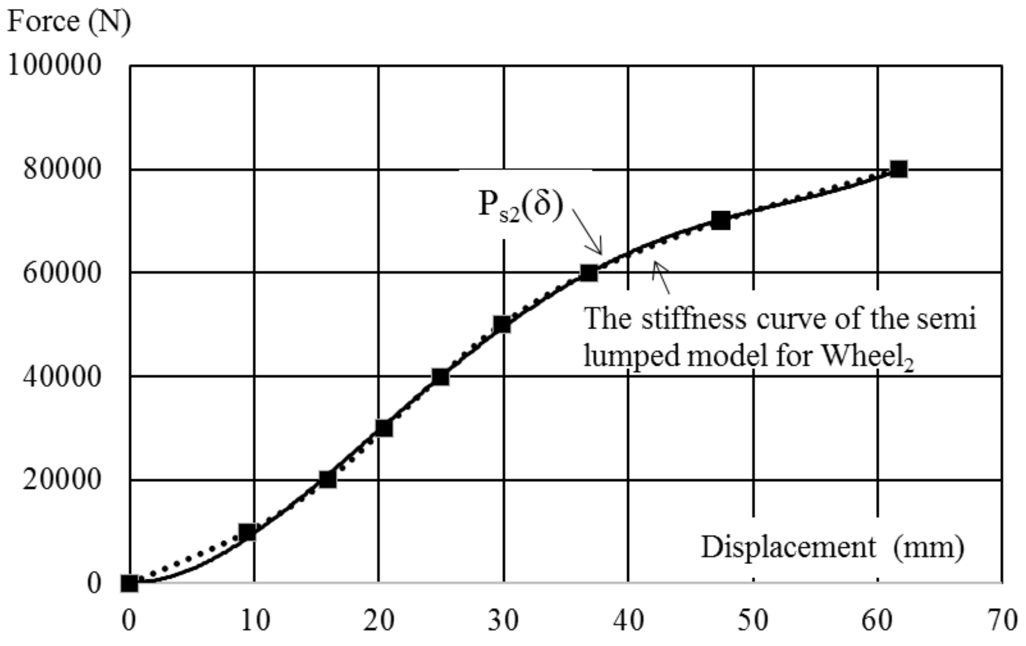

Figure A.2. Comparison of the polynomial and the stiffness curves for $wheel_2$

APPENDIX B

MATLAB CODE FOR WHEEL$_1$

```
% MATLAB 2015 code for finding potential-strain energy equilibrium points of
% the semi-lumped system for wheel1
syms x FX ESX ESX1 ESX2 ESX3 Fit
% Defining force in N, displacement in mm values of the semi-lumped system.
Displacement = [ 0 8.85 14.47 17.96 20.95 23.95 28.16 34.27 42.14 50 53.95]
Force= [0 10000 20000 30000 40000 50000 60000 70000 80000 90000 95000]
% Defining impact load and drop height of the striker.
Impactload1=450 ;Impactload2=550 ;Impactload3=800;dropheight=230
% Obtaining the force-displacement function of the semi-lumped system.
p1=polyfit (Displacement, Force,6)
a1=p1(1); b1=p1(2); c1=p1(3); d1=p1(4); e1=p1(5); g1 = p1(6); r1 = p1(7)
FX=a1*x^6+b1*x^5+c1*x^4+d1*x^3+e1*x^2+g1*x+r1
% Checking maximum error of the polynomial function.
Fit = polyval(p1,Displacement);
T = table(Displacement,Force,Fit,(Force-Fit),'VariableNames',{'Displacement','Force','Fit','FitError'})
% Obtaining the strain energy-displacement function of the semi-lumped system.
ESX=int(FX,x)
%Finding potential - internal energy equilibrium points in mm.
ESX1=Impactload1*9.81*(dropheight+x)
D1= vpasolve(ESX1 == ESX, x, [0 60])
ESX2=Impactload2*9.81*(dropheight+x)
D2= vpasolve(ESX2 == ESX, x, [0 60])
ESX3=Impactload3*9.81*(dropheight+x)
D3= vpasolve(ESX3== ESX, x, [0 60])
%Drawing the Force-Displacement points and the corresponding polynomial function.
figure;plot (Displacement,Force,'o');hold on
x= [0:1:54]
subs(FX);plot(x,ans,'-')
%Drawing potential and strain energy curves
x= [0:1:60]
figure;subs(ESX);plot(x,ans)
hold on;subs(ESX1);plot(x,ans);subs(ESX2);plot(x,ans);subs(ESX3);plot(x,ans)
hold off
```

APPENDIX C

MATLAB CODE FOR WHEEL$_2$

```
% MATLAB 2015 code for finding potential-strain energy equilibrium points of
% the semi-lumped system for wheel2
syms x FX ESX ESX1 ESX2 ESX3 Fit
% Defining force in N, displacement in mm values of the semi-lumped system.
Displacement = [ 0 9.48 15.88 20.47 24.92 29.82 36.82 47.44 61.71]
Force= [0 10000 20000 30000 40000 50000 60000 70000 80000]
% Defining impact load and drop height of the striker.
Impactload1=400 ;Impactload2=540 ;Impactload3=900;dropheight=230
% Obtaining the force-displacement function of the semi-lumped system.
p1=polyfit (Displacement, Force,4)
a1=p1(1); b1=p1(2); c1=p1(3); d1=p1(4); e1=p1(5)
FX=a1*x^4+b1*x^3+c1*x^2+d1*x+e1
% Checking maximum error of the polynomial function.
Fit = polyval(p1,Displacement);
T = table(Displacement,Force,Fit,(Force-
Fit),'VariableNames',{'Displacement','Force','Fit','FitError'})
% Obtaining the strain energy-displacement function of the semi-lumped system.
ESX=int(FX,x)
%Finding potential - internal energy equilibrium points.
ESX1=Impactload1*9.81*(dropheight+x)
D1= vpasolve(ESX1 == ESX, x, [0 60])
ESX2=Impactload2*9.81*(dropheight+x)
D2= vpasolve(ESX2 == ESX, x, [0 60])
ESX3=Impactload3*9.81*(dropheight+x)
D3= vpasolve(ESX3== ESX, x, [0 60])
%Drawing the Force-Displacement points and the corresponding polynomial function.
figure;plot(Displacement,Force,'o');hold on
x= [0:1:62]
subs(FX);plot(x,ans,'-')
%Drawing potential and strain energy curves
figure;subs(ESX);plot(x,ans)
hold on;subs(ESX1);plot(x,ans);subs(ESX2);plot(x,ans);subs(ESX3);plot(x,ans)
hold off
```

APPENDIX D

DETAILS OF THE COMPUTATIONAL TIME

Table D.1. Details of the computational time of the static and dynamic model for wheel$_2$ under impact load 900 kg

Definition	Model	
	Static	Dynamic
Central process unit, CPU, type of the computer	Intel Core i7 3630 QM 2.4 GHz	
Memory of the computer	16 GB	
Number of cores of the computer	4 (Number of threads 8)	
Number of nodes of the FE model	670479	231244
Number of elements of the FE model	306237	501671
End or termination time of the simulation [sec]	Not applicable	0.1
Computing time of the FE model (Hour)	20	60

VITA

Uğur PEHLİVANOĞLU was born in Ankara/TURKEY in January 01, 1973. After graduation from Mechanical Engineering department of İstanbul Technical University, he continued his MSc. studies in the same university. After he worked in the private sector for thirteen years, and then began his PhD studies in the Department of Mechanical Engineering of İzmir Institute of Technology.

Education

- PhD in English, 2016, Mechanical Engineering, İzmir Institute of Technology.
- MSc. in Turkish, 1997, Mechanical Engineering, İstanbul Technical University.
- B.Sc. in Turkish, 1994, Mechanical Engineering, İstanbul Technical University.

Professional Experience

- CEVHER Alloy Wheels, R&D Supervisor, 2011-2016, İzmir/TURKEY
- CEVHER Alloy Wheels, Mold Design and Production Supervisor, 2002-2011, İzmir/TURKEY.
- CMS, Design Engineer, 1998-2002, İzmir/TURKEY.